DEVELOPMENT OF AN AEROELASTIC METHODOLOGY FOR SURFACE MORPHING ROTORS

A Dissertation
Presented to
The Academic Faculty

by

James R. Cook

In Partial Fulfillment
of the Requirements for the Degree
Doctor of Philosophy in the
School of Aerospace Engineering

Georgia Institute of Technology
May 2014

DEVELOPMENT OF AN AEROELASTIC METHODOLOGY FOR SURFACE MORPHING ROTORS

Approved by:

Professor Marilyn J. Smith,
Committee Chair
School of Aerospace Engineering
Georgia Institute of Technology

Professor Olivier Bauchau
School of Aerospace Engineering
Georgia Institute of Technology

Professor Narayanan Komerath
School of Aerospace Engineering
Georgia Institute of Technology

Professor Mark Costello
School of Aerospace Engineering
Georgia Institute of Technology

Professor Carlos Cesnik
School of Aerospace Engineering
University of Michigan

Date Approved: January 10, 2014

Dedicated to my lovely wife, Lisa

ACKNOWLEDGEMENTS

I would like to first express gratitude to my advisor Dr. Marilyn J. Smith for suggesting the topic of my thesis and for her valuable guidance and counseling. Many thanks also to the other committee members of my thesis for their advice in improving the quality of my research.

I would like to thank Bob Biedron and Elizabeth Lee-Rausch at NASA Langley for providing the HART blade geometry and one of the grids used in this work.

I offer thanks Dr. Cesnik at the University of Michigan for his guidance and collaborative efforts. I would like to thank Smith Thepvongs for the significant amount of work and effort he contributed to NLABS modifications for the CFD/CSD coupling interface and for generating the NLABS input decks used in the majority of coupled HART simulations. Thanks also to Devesh Kumar for his instructional help in using NLABS and for generating a baseline NLABS deck for the NACA 0012 simulations.

Finally, I would like to thank the students of the Nonlinear Computational Aeroelasticity Lab for their support, suggestions, and discussions. In particular I would like to thank Eric Lynch, Rajiv Shenoy, Daniel Prosser, and Eliot Quon for their assistance and helpful comments in operation and modification of FUN3D and for assistance in job submission.

This work was sponsored by the National Rotorcraft Technology Center (NTRC) Vertical Lift/Rotorcraft Center of Excellence (VLRCOE) at the Georgia Institute of Technology and the University of Michigan. Dr. Mike Rutkowski is the technical monitor of this center. Opinions, interpretations, conclusions, and recommendations are those of the authors and are not necessarily endorsed by the United States Government. Computational support for the NTRC was provided through the DoD High Performance Computing Centers at ERDC and NAVO through HPC grants from the US Army (S/AAA Dr. Roger Strawn).

TABLE OF CONTENTS

LIST OF TABLES

LIST OF FIGURES

NOMENCLATURE

a	Speed of sound
a	Location of the elastic axis aft the midchord, semichords
A	Inertia matrix operator
A_{cell}	Area of a grid cell face, m^2
b	semi-chord, m
$\mathbf{b}$	Reference frame of undeformed rotor blade
$\mathbf{B}$	Reference frame of deformed rotor blade
c	Chord length, m
c_{d0}	Profile drag coefficient, $c_{do} = \frac{D_0}{\frac{1}{2}\rho_\infty V_\infty^2} c$
c_l	Lift coefficient, $c_l = \frac{L}{\frac{1}{2}\rho_\infty V_\infty^2} c$
c_m	Moment coefficient, $c_m = \frac{M_{qc}}{\frac{1}{2}\rho_\infty V_\infty^2} c$
c_n	Normal force coefficient, $c_n = \frac{N}{\frac{1}{2}\rho_\infty V_\infty^2} c$
c_p	Pressure coefficient, $c_p = \frac{p - p_\infty}{\frac{1}{2}\rho_\infty V_\infty^2}$
c_Λ	Camber force coefficient
$[C]$	Damping matrix
C	Rotation matrix
$C(k)$	Theodorsen function
C_T	Thrust coefficient, $\frac{T}{\pi R^2 (\Omega R)^2}$
C_P	Power coefficient, $\frac{P}{\pi R^2 (\Omega R)^3}$

C_ν, C_ϵ	Coefficients in the LES k equation
d	Distance, m
D	Drag per unit span, N/m
D_0	Profile drag per unit span, N/m
D_k	Turbulence dissipation term
e	Specific internal energy, J/g
E	Energy, J/m^3
E^*	Normalized error over one revolution
f_i	Force in direction i, N
$\mathcal{F}$	Turbulence blending function
$\vec{F}$	Normal force vector, N
F_x	Force in x-direction, N
F_y	Force in y-direction, N
F_z	Force in z-direction, N
FM	Figure of merit, FM $= \dfrac{C_T^{3/2}}{\sqrt{2}C_P}$
g	Current trim value
G	Target trim value
$[G]$	Greenberg matrix
h	Local vertical displacement of airfoil, m
h	Specific enthalpy, J
h_c	Characteristic length of beam cross-section, m

h_c	Characteristic length of initial curvature and twist of a slender beam, m
h_n	Generalized vertical deflection modes
J	Trim Jacobian
k	Turbulence kinetic energy, J
k	Reduced frequency, $k = \omega b / V_\infty$
k_α	Torsional spring coefficient, N-m/rad
k_ζ	Translational spring coefficient, N/m
$[K]$	Stiffness matrix
L	Lift per unit span, N/m
L_c	Characteristic wavelength of structural response along reference line, m
L_{fs}	Aerodynamic loading operator
L_{ij}	Leonards' stress
L_n	Generalized loads
L_y	Dimension of grid normal to wall, m
m	Mass per unit span, kg/m
M	Mach number, $\frac{V}{a}$
$[M]$	Mass matrix
M_{ab}	Pitching moment at elastic axis per unit span, N-m/m
M_{qc}	Pitching moment at quarter chord per unit span, N-m/m
M_x	Moment about x-axis (roll moment), N-m
M_y	Moment about y-axis (pitch moment), N-m

M_z	Moment about z-axis (yaw moment), N-m
N	Force normal to chordline per unit span, N/m
N	Shape function
p	Pressure, Pa
P	Power required, N-m/s
P_k	Turbulence production term
Pr	Prandtl number, $\frac{\nu}{\alpha}$
q	Dynamic pressure, $q = \frac{1}{2}\rho V_\infty^2$, Pa
q	Heat flux, W/m^2
$\vec{q}$	Displacement vector
q_L	Laminar transport of heat, W/m^2
q_m	Finite section displacements
q_T	Turbulence transport of heat, W/m^2
r	Undeformed reference line along the dominant direction of a slender beam
r	Local radial distance from the hub center, m
r_α	Radius of gyration, m
r_δ	Moment of inertia of the camber mode, $r_\delta = \sqrt{I_\delta/m}$, m
R	Rotor radius
$\mathcal{R}$	Deformed reference line along the dominant direction of a slender beam
Re	Reynolds number, Re= $\frac{\rho_\infty V_\infty x}{\mu}$
s	Nondimensional time, $s = \frac{tV_\infty}{b}$

s_{ij}	Instantaneous strain-rate tensor
$[S]$	Drag matrix
S	Structural matrix operator
S_{ij}	Mean strain-rate tensor
t	Time, s
t_{ij}	Viscous stress tensor
T	Period, s
T	Temperature, K
T_n	Chebyshev polynomials
u, v, w	Velocity in x, y, and z directions, respectively, m/s
u_i	Velocity in dimension i, m/s
v_n	Generalized inflow velocity modes, m/s
V_{cell}	Cell volume, m^3
V	Velocity, m/s
V^*	Nondimensional velocity, $V^* = \frac{V}{\omega_\delta b}$
w	Weight function
$\vec{w}$	Warping vector – cross-sectional deformations after rigid-body translation and rotation has been removed
W	Work, N-m
x, y, z	Cartesian coordinate axes, m
$\vec{x}$	Undeformed position vector

x_i	Cartesian coordinates in direction i, m
x_α	Coordinates along reference frame defining cross-section of airfoil, m
$\vec{X}$	Deformed position vector
y	Distance to nearest wall
$y+$	Non dimensional distance from wall, $y+ = \frac{y}{\nu}\sqrt{\frac{\tau_w}{\rho}}$
α	Pitch deflection, rad
α	Thermal diffusivity, m^2/s
α, β	State coefficients for dynamic inflow model
β	Flap angle, rad
γ	Ratio of specific heats
Γ_s	Dynamic stall states
δ	Camber deflection, m
δ	Boundary layer thickness, m
δ_{ij}	Kronnecker delta
Δ	Characteristic grid-scale length, $\Delta = V_{cell}^{1/3}$, m
$\hat{\Delta}$	Test filter characteristic length, m
$\vec{\epsilon}$	Strain, m
ϵ	Normalized error
ε	Force strain
ζ	Lead/lag angle, rad
ζ	Plunge deflection, m

ζ_d	Damping ratio
ζ_n	Bound circulation due to source other than airfoil, m^2/s
θ	Pitch angle, rad
θ_0	Collective control pitch, rad
θ_{1c}	Lateral cyclic control, rad
θ_{1s}	Longitudinal cyclic control, rad
κ	Inverse mass ratio $\kappa = \pi\rho b/m$
κ_i	Moment strain, rad
λ_n	Generalized induced velocity due to wake vorticity
Λ	Camber force per unit span, N/m
μ	Advance ratio, $\frac{V_\infty}{\Omega R}$
μ	Molecular viscosity, Pa-s
μ_t	Eddy viscosity, Pa-s
ν	Kinematic viscosity, m^2-s
ν_t	Kinematic eddy viscosity, m^2-s
ξ	Nondimensional distance from midchord, semichords
ρ	Density, kg/m^3
τ	Stress, N-m^2
τ_{ij}	Reynolds stress tensor
ϕ	Set of radial expansion functions for dynamic inflow model
ψ	Azimuth angle, rad

ψ_{qm}	Finite section deformation modes
Ψ	Camber mode, m
ω	Dissipation per unit k, m^2/s^3
ω	Natural mode frequency, rad/s
Ω	Vorticity, s^{-1}
Ω	Rotational velocity of rotor, rad/s
$(\cdot)''$	Fluctuating value in relation to Favre-averaged values
$(\cdot)'$	Fluctuating value
$(\cdot)'$	Spatial derivative
$\ddot{(\cdot)}$	Second time derivative
$\dot{(\cdot)}$	Time derivative
$\hat{(\cdot)}$	Nondimensional value
$\langle(\cdot)\rangle$	Variable filtered at test level
$\overline{(\cdot)}$	Time-averaged value
$\tilde{(\cdot)}$	Favre-averaged value
$(\cdot)^{CFD}$	CFD value
$(\cdot)^{CSD}$	CSD value (using low-order aerodynamics)
$(\cdot)^{HYBRID}$	Hybrid RANS/LES turbulence property
$(\cdot)^n$	Value at time step n
$(\cdot)^{RANS}$	Turbulence property calculated by RANS formulation
$(\cdot)^{SGS}$	Subgrid-scale turbulence property

$(\cdot)_\infty$	Freestream value
$(\cdot)_F$	Value at flutter speed
$(\cdot)_{r-t}$	Average root-to-tip value
$(\cdot)_{root}$	Value at blade root
$(\cdot)_{tip}$	Value at blade tip

SUMMARY

Helicopter performance capabilities are limited by maximum lift characteristics and vibratory loading. In high speed forward flight, dynamic stall and transonic flow greatly increase the amplitude of vibratory loads. Experiments and computational simulations alike have indicated that a variety of active rotor control devices are capable of reducing vibratory loads. For example, periodic blade twist and flap excitation have been optimized to reduce vibratory loads in various rotors. Airfoil geometry can also be modified in order to increase lift coefficient, delay stall, or weaken transonic effects.

To explore the potential benefits of active controls, computational methods are being developed for aeroelastic rotor evaluation, including coupling between computational fluid dynamics (CFD) and computational structural dynamics (CSD) solvers. In many contemporary CFD/CSD coupling methods it is assumed that the airfoil is rigid to reduce the interface by single dimension.

Some methods retain the conventional one-dimensional beam model while prescribing an airfoil shape to simulate active chord deformation. However, to simulate the actual response of a compliant airfoil it is necessary to include deformations that originate not only from control devices (such as piezoelectric actuators), but also inertial forces, elastic stresses, and aerodynamic pressures. An accurate representation of the physics requires an interaction with a more complete representation of loads and geometry. A CFD/CSD coupling methodology capable of communicating three-dimensional structural deformations and a distribution of aerodynamic forces over the wetted blade surface has not yet been developed.

In this research an interface is created within the Fully Unstructured Navier-Stokes (FUN3D) solver that communicates aerodynamic forces on the blade surface to University of Michigan's Nonlinear Active Beam Solver (UM/NLABS – referred to as NLABS in this thesis). Interface routines are developed for transmission of force and deflection information

to achieve an aeroelastic coupling updated at each time step. The method is validated first by comparing the integrated aerodynamic work at CFD and CSD nodes to verify work conservation across the interface. Second, the method is verified by comparing the sectional blade loads and deflections of a rotor in hover and in forward flight with experimental data. Finally, stability analyses for pitch/plunge flutter and camber flutter are performed with comprehensive CSD/low-order-aerodynamics and tightly coupled CFD/CSD simulations and compared to analytical solutions of Peters' thin airfoil theory to verify proper aeroelastic behavior. The effects of simple harmonic camber actuation are examined and compared to the response predicted by Peters' finite-state (F-S) theory.

In anticipation of active rotor experiments inside enclosed facilities, computational simulations are performed to evaluate the capability of CFD for accurately simulating flow inside enclosed volumes. A computational methodology for accurately simulating a rotor inside a test chamber is developed to determine the influence of test facility components and turbulence modeling and performance predictions. A number of factors that influence the physical accuracy of the simulation, such as temporal resolution, grid resolution, and aeroelasticity are also evaluated.

CHAPTER I

INTRODUCTION

1.1 Motivation

Helicopter performance in forward flight is limited by maximum lift characteristics and vibratory loads [1]. As the advance ratio increases, large fluctuations in relative wind speed increase variations in blade loading, resulting in larger vibratory hub loads. Transonic flow over the advancing side of the rotor and dynamic stall on the retreating side introduce additional sources of vibratory loading [2, 3]. Vibratory hub loads shorten pilot endurance, decrease the life of structural components, and limit performance capabilities, such as lift, forward speed, and maneuverability [4, 5].

Several design concepts have been investigated with the intention of expanding the flight envelope and improving helicopter performance. These can be categorized as: 1) methods in which one or more discrete control surfaces are rigidly deflected, and 2) methods in which the blade is elastically deformed. One disadvantage of rigid control surfaces is the increase in drag due to hinge gap and discontinuous surface geometry [6, 7]. Active blade morphing concepts present a control solution in which this drag penalty is avoided, since the blade surface remains continuous as it is deformed. A number of airfoil morphing schemes have been developed in which the cross-sectional thickness or camber is altered to actively adapt stall, lift, and moment characteristics [8, 9, 10, 11, 12, 13]. As deflection of the camber line can affect the pitching moment, active airfoil morphing may also be implemented as a means for achieving active blade twist.

Currently the state of the art for the structural model of a rotor blade in computational aeroelastic analyses is a one-dimensional beam model. While some CFD/CSD rotor simulations have included prescribed airfoil deformations [10, 14] to simulate active camber, in most cases it is assumed that the airfoil shape is rigid. Traditionally, aerodynamic pressures have little effect on airfoil deformation, since the cross section of a rotor blade is usually

constructed to be very stiff to ensure stability. However, if compliant materials are integrated into the blade structure [15] to decrease the force required from control devices for airfoil deformation, then the airfoil becomes more susceptible to aeroelastic deformations.

Experimental results [16, 17] reveal that recirculation of the wake can influence thrust and torque characteristics as well as vibratory hub loads. Therefore, to evaluate the influence of active controls on blade loading, the influence of test facility components on rotor performance must also be determined. If significant non-periodic vibratory loads result from recirculatory effects or the test rig, then it may not be possible to isolate the aeroelastic effects of active controls from those of the test facility.

1.2 Control Mechanisms

Various concepts for flow control, including leading edge slats, trailing edge flaps, active blade twist, and active airfoil morphing, have been investigated to improve the performance capabilities of rotorcraft. The intended effects of these blade modifications include: increasing maximum lift coefficient, reducing drag, and minimizing vibratory loads [8, 9, 10, 11, 12, 13]. A description of various control devices under current development and the contributions of past and current research efforts are presented in the following sections.

1.2.1 Actuator Materials

Due to weight and space limitations, designing an actuation mechanism that can feasibly be implemented can be a challenge. Smart materials are useful in the design of control mechanisms, as they are lightweight and capable of supplying the forces required for effective control surface excitation. A combination of active and compliant materials can be applied in order to achieve the desired elastic deformations. Shape memory alloys and piezoelectrics are two classes of materials that are commonly integrated into active control mechanisms.

1.2.1.1 Shape Memory Alloy

Shape memory alloys (SMA) are alloys which can revert to multiple structural shapes upon activation. Activation is accomplished by simply heating or cooling the SMA, causing

a phase change in the crystal structure from martensite to austenite or vice versa, and allowing the structural geometry to be changed during flight [18]. Roglin and Hanagud [19] applied SMA technology to rotor blades as a collective control device. In their approach SMA wires were configured to adjust the trailing edge flap deflection when activated. This concept was successfully demonstrated on a model-scale helicopter. Although SMA devices are capable of producing large deflections, they generally have a slow response due to the time required for heating and cooling the materials, and therefore they are not suitable for applying high-frequency deflections.

1.2.2 Piezoelectric Materials

Piezoelectric devices are ideal for active blade controls because they are lightweight, compact, and capable of producing large forces at high frequencies [20]. The main disadvantage is that they are only capable of generating very small strains. Therefore, control systems must be configured in such a way that small strains in piezoelectric devices are amplified to provide sufficient blade surface deflections. There are two principal methods for implementing piezoelectric devices. The first is to integrate piezoelectric stacks within the airfoil structure. Internal piezoelectric stacks can actuate a hinged control device, such as trailing edge flap. A number of mechanisms have been developed for amplification of piezoelectric stroke, such as double-lever (L-L) amplification mechanisms [21], double C-block actuators [22], double X-frame actuators [23], and bimorph levers [24]. In an L-L mechanism (Fig. 1(a)) two levers are connected serially to the piezoelectric stack to amplify the stroke. A C-block actuator (Fig. 1(b)) embeds a series of curved piezoelectric materials in a "C"-shaped structure. A pair of C-block actuators can be mounted to a flap and, by expanding one actuator and contracting the other, apply a deflection. When the piezoelectric material on an X-frame actuator (Fig. 2(a)) is excited, the two outer ends move together, and an output lever is deflected. The deflection of piezoelectric bimorphs (Fig. 2(b)), which bend when a voltage is applied, can be amplified by a lever mechanism to increase the deflection of a the trailing edge flap. To maintain a continuous blade surface, the internal structure can be covered by a flexible skin so that the surface remains smooth but deformable.

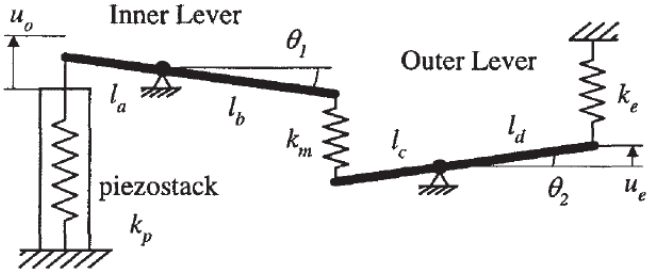

(a) Double lever [21]

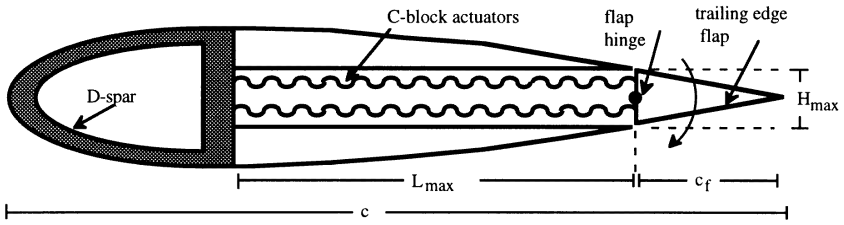

(b) C-block actuator [22]

Figure 1: Schemes for using piezoelectric material for airfoil deformation.

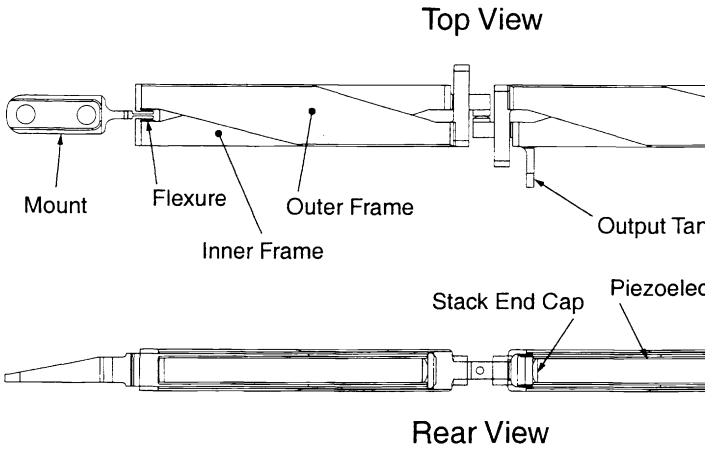

(a) Double X-frame actuator [23]

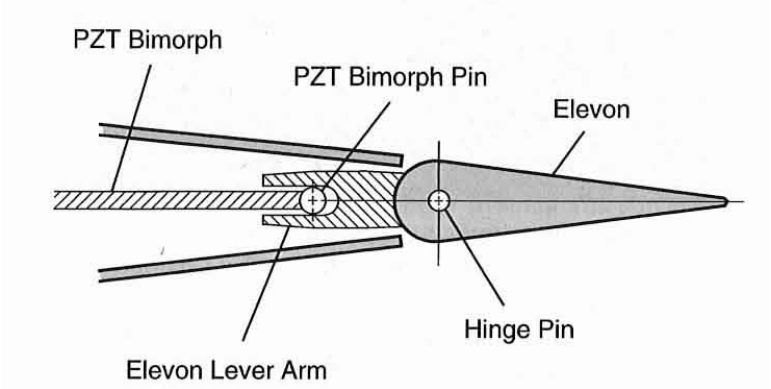

(b) Bimorph levers [24]

Figure 2: Continued, schemes for using piezoelectric material for airfoil deformation.

1.2.3 Flaps and Slats

Sufficient improvements in rotor performance must be demonstrated to justify the increased cost of developing and manufacturing control devices. Chandrasekhara et al. [8] performed an experiment comparing stall characteristics of a RC(6)-08 airfoil (Fig. 3a) with and without a leading edge slat. When the slat was deployed stall was delayed as airflow through the slot prevented the flow from detaching from the main section of the airfoil at higher angles attack. Deep stall could be delayed by about 2° if a 6° slat was attached (Fig. 3b), and by 3.5 degrees if a 10° slat was attached (Fig. 3c).

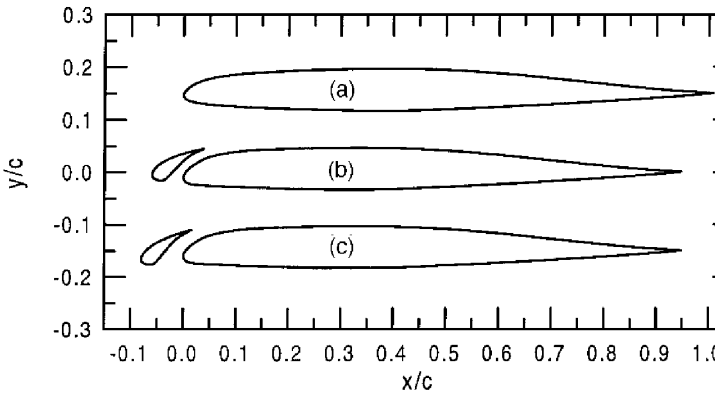

Figure 3: Airfoils with a) no leading edge slat b) 6° leading edge slat c) 10° leading edge slat [8].

Gurney flaps have also been investigated as a means of increasing the maximum lift. These small tabs are typically attached to the trailing edge of an airfoil, normal to the blade surface [25] (Fig. 4). Maughmer et al. [26] measured up to 30% increase in maximum lift coefficient for the S903 airfoil when applying a $0.02c$ Gurney flap at the trailing edge. However, the nose-down pitching moment increased in magnitude by about 0.1 for most angles of attack. In addition, significant increases in drag were measured in the pre-stall regime. Lee and Su [27] conducted experimental studies on a NACA 0015 airfoil which demonstrated that lift increases as Gurney flap height increases, but again an increase in drag and pitching moment was observed. In rotorcraft applications a deployable Gurney flap may be useful for increasing maximum lift for short periods of time on the retreating side of the blade. If the Gurney flap is moved forward of the trailing edge, then it is more

feasible to design an active Gurney flap which is periodically retracted. Thus, during times when the Gurney flap is not beneficial, it can be retracted to avoid the adverse effects on drag and pitching moment. Shifting the Gurney flap location does, however, reduce its effectiveness.

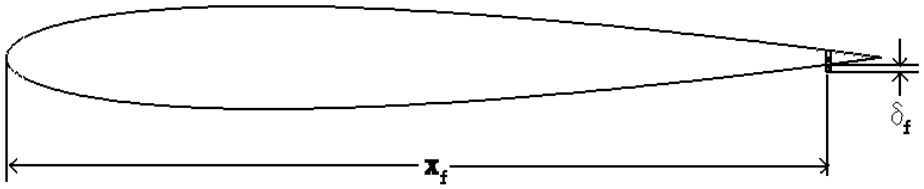

Figure 4: Airfoil with Gurney flap.

1.2.4 Active Trailing Edge Flaps

Trailing edge flaps (Fig. 5) can optimize performance in various flow conditions by altering the effective camber of an airfoil and thereby the lift and moment characteristics. The deflection angle of the flap can be activated at various frequencies to reduce harmonic loads.

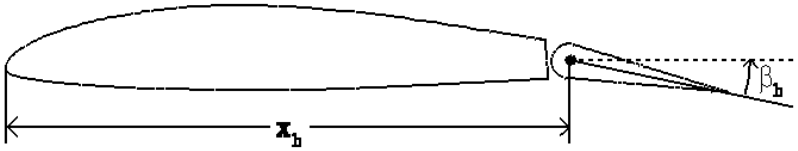

Figure 5: Airfoil with active trailing edge flap.

Straub et al. [28] introduced a Smart Material-Actuated Rotor Technology (SMART) design in which trailing edge flap deflections are driven by piezoelectric stacks. In 2009 Straub et al. [29] demonstrated through extensive wind tunnel testing that by optimizing the excitation frequency and amplitude of active trailing edge flaps, vibratory normal forces could be reduced by up to 80% for five-per-revolution loading, 98% for one-per-revolution loading, and 83% for the RMS unsteady loads of all harmonics. This experiment confirmed

that periodic adaptation of the airfoil shape can offer substantial reductions in vibratory loads.

Kim et al. [30] investigated blade load control using classical incompressible theory for rotor blades with one-per-revolution active trailing edge flaps. The aeroelastic model was used to develop an optimized control function that reduced maximum flap bending moment by 33%. They also predicted that maximum pitch link loads could be reduced by 40% to 81%, depending on the camber of the airfoil.

The disadvantage of flap mechanisms is that the surface of the blade is discontinuous at the hinge and ends of the flaps, resulting in a drag increase. In addition, trailing edge flaps greatly increase the complexity of the blade structure with additional hinges and activation mechanisms.

1.2.5 Active Twist Rotors

Elastic blade deformation is preferable to flaps, because the blade surface remains smooth, and therefore the control device does not introduce drag penalties. An active twist rotor (ATR) allows the blade pitch to be controlled as a function of both azimuth and radial position and therefore offers more control over cyclic loading and provides a means for vibration reduction. Shin et al. [31, 32] demonstrated through experimental tests that active twist, achieved through actuation of piezoelectric fibers embedded in the skin, can reduce vibratory loads by 90% in forward flight. In wind tunnel tests, one-per-revolution and 4 per revolution normal hub forces were successfully reduced by up to 40 dB [32] through application of closed-loop cyclic control. Bernhard et al. [33] obtained similar results using piezoelectric plies to apply active twist, reducing the vibratory loads by 63% in forces, 90% in rolling moment, and 74% in pitching moment at advance ratio $\mu = 0.33$.

Coupling between twist modes and other elastic modes in composite materials can be used advantageously for active twist control. Haynes [34] determined through finite-element analysis that extension-twist and bend-twist coupling can be achieved by applying the proper layup of composite laminates. He derived the necessary conditions for stability, determined the minimum number of plies for stability, and optimized the laminates for

extension-twist, bend-twist, anticlastic, extension-bend, and shear-twist coupling. The optimized configuration for extension-twist and bend-twist were demonstrated experimentally. This verifies that optimized layup of composite materials can be applied for active twist and reduction of hub loads.

1.2.6 Airfoil Morphing

Airfoil shape may also be modified to alter the aerodynamic characteristics of a blade. Chandrasekhara [8] demonstrated that the radius of the leading edge may be increased to increase the lift-to-drag ratio at high angles of attack. His experiments demonstrated that an airfoil with a large radius at the leading edge is less susceptible to separation at high angles of attack.

Variable droop leading edges (VDLE) have also been investigated for delaying leading-edge separation. In VDLE applications a significant portion of a leading edge of the airfoil is deflected downward [10, 11]. At high angles of attack this can prevent leading-edge separation, allowing larger maximum values of lift to be produced.

Active trailing edge deflection can also enhance rotor performance. Bilgen et al. [35] conducted wind tunnel tests of a wing section in which variable camber was applied by macro-fiber composites (MFC) embedded in the skin on the trailing section of the airfoil. The lift coefficient was increased near stall by up to 5.2%. Gandhi et al. [36] designed and optimized a variable-camber wing section through integration of piezoelectric stacks within the wing structure, with a compliant skin applied on the wing surface. Two optimum designs – highest tip deflection per unit strain energy and maximum trailing edge deflection – were determined in an ANSYS analysis. In both the computational study and in a structural prototype 0.73%c and 1.2%c trailing edge deflections were achieved when applying 1000 V across the actuators for the maximum ratio and maximum deflection objectives, respectively. The latter results in $17-22\%$ increase in predicted lift at 5° angle of attack. Aerodynamic loads computed by X-FOIL were applied in the computational analysis, in which a 0.064%c deflection was predicted.

Grohmann et al. [37] presented the design of an active trailing edge and active tab

which were deformed by layers of piezoelectric fibers. The design was successful at providing deflections at frequencies ranging from two-per-revolution to six-per-revolution. In hover conditions aerodynamic effects reduced the control authority by approximately 20%, indicating that aeroelastic effects must be included in analysis of blade loading response.

In an experimental study Bilgen et al. [12] demonstrated that adding energy in the boundary layer can also improve performance at high angles of attack. The energy is added via piezoelectrically-excited surface deformation on the suction surface near the leading edge. Bilgen et al. demonstrated that the technique can delay stall, and in doing so increase the maximum lift by up to 7.6%.

These methods represent several applications of surface deformation have potential for improving maximum-lift characteristics and delaying stall.

1.3 Computational Methods for Aeroelastic Analysis

Early methods of calculating lift coefficient developed by Young [38] were used to predict lift based on empirical lift increments for deflected flaps, with adjustments for the ratio of chord length to the effective chord length. The Douglas Aircraft Company [39], employed a simple empirical method for extending two-dimensional characteristics by applying a ratio of the control surface areas $\frac{S_r}{S}$ for trailing-edge flaps or fraction of the affected span $\frac{b_r}{b}$ for leading-edge flaps. Generally error in these predictions ranged from 10% to 30% [40]. In the 1970's Smith [41] formulated a theoretical approach for calculating lift of a multi-element airfoil. This theory was based on the influence of induced velocity from one element on upstream elements, which he called the "dumping effect."

As computational methods were developed and more resources became available, implementation of the Euler and Navier-Stokes solutions became feasible for aerodynamic analyses. Brune and McMasters [42] demonstrated the importance of viscous effects in determining the lift characteristics of flapped and slotted airfoils with computational analysis. Unstructured grid methodologies simplified grid generation for complex structures, such as those which include leading edge slats and trailing edge flaps. For example, Newman et al. [43] performed a two-dimensional CFD analysis for shape optimization of a four-element

airfoil designed for high lift.

Computational fluid dynamics analysis has greatly extended the capability to evaluate aeroelastic behavior of wings, especially in flows where nonlinear aerodynamic behavior, such as transonic flow or stall, is significant. Guruswamy [44] developed an aeroelastic method for coupling a structural analysis with an Euler solution from the CFD code ENSAERO. In his work, structural modes were computed via finite element analysis applying the Rayleigh-Ritz method. The time-accurate aeroelastic equations of motion were then solved:

$$[M]\{\ddot{q}\} + [C]\{\dot{q}\} + [K]\{q\} = \{F\} \tag{1}$$

where $\{q\}$ is the generalized displacement vector, $[M]$, $[C]$, and $[K]$ are the modal mass, damping and stiffness matrices, respectively, and $\{F\}$ is the generalized aerodynamic force vector. Guruswamy applied this method to flutter analysis of a wing in transonic flow, and the computed pressure results agreed well with experimental data, although some discrepancies arose due to grid resolution. His results demonstrated the potential value of computational aeroelastic analysis, especially in flows where small-disturbance assumptions are not valid.

Bauchau and Ahmad [45] outlined a method for coupling CFD and CSD for aeroelastic rotor simulation. The blade is modeled as a one-dimensional beam with a number of airstations along the span. Aerodynamic sectional forces and moments are calculated at each section and communicated to the CSD solver. Deflections and rotations of each section are communicated from the CSD solver to the CFD solver and applied to the grid nodes in a coordinate transformation. This method provides a basis upon which most other coupling methods are based [46, 47, 48, 49]. Bauchau and Ahmad also describe three schedules in which information is exchanged in the fluid-structure interface:

1. Full coupling – The structural and aerodynamic solutions are solved simultaneously. This is the most accurate method of aeroelastic analysis, but is computationally expensive.

2. Tight coupling – Information between the structural and aerodynamic solvers is exchanged every time step. For better convergence multiple iterations of the data exchange and solutions may be performed for a single time step.

3. Loose coupling – Information is exchanged in the fluid-structure interface periodically, usually once per revolution or N_b times per revolution, where N_b is the number of blades. The process is repeated until convergence is reached, at which time the solution becomes periodic.

Farhat [50] contributed valuable insight into methods for parallel CFD/CSD coupling and development of fluid-structure interfaces (FSI). In particular, he presented a method for communication of data between "incompatible" mesh interfaces, in which the CFD and CSD nodes are not coincident. In this methodology the aerodynamic forces are communicated to the structural solver by integrating over the wetted surface of structural elements. For a node i on the fluid interface, the force f_i on a structural element e is:

$$f_i = -\int_{\bar{\Omega}(e)} N_i p v d\sigma \tag{2}$$

where $\bar{\Omega}(e)$ is the domain of element e, N_i is the shape function associated with i, p is the pressure, and v is the unit normal to $\bar{\Omega}(e)$. Farhat notes that most structural codes evaluate this integral via the quadrature rule,

$$f_i = -\sum_{g=1}^{n_g} w_g N_i(X_g) p(X_g), \tag{3}$$

where w_g is the weight of Gauss point X_g. In this manner forces can be integrated from a pressure distribution defined on the fluid mesh. Likewise, the structural deformations can be transferred to fluid nodes by finite element interpolation:

$$\vec{x}(S_j) = \sum_{k=1}^{wne} N_k(\xi_j)\vec{q}(e)_k, \tag{4}$$

where S_j represents a fluid grid point on the interface surface, wne represents the number of nodes in the nearest structural element e, ξ_j are the natural coordinates of S_j in $\bar{\Omega}(e)$, and $\vec{q}_k$ is the structural displacement of node k. This contribution from Farhat is valuable, as

structural and fluid grids are often generated independently and are governed by a different set of criteria for grid resolution.

In cases where the airfoil is flexible, methods have been developed for including cross-sectional deformations. Yeo [11] performed two-dimensional airfoil analyses on various airfoils at several Mach numbers and angles of attack and tabulated the aerodynamic characteristics. He performed an aeroelastic analysis by applying lifting-line theory to the tabulated airfoil characteristics. This method lacks accuracy due to the two-dimensional assumption, but may be able to estimate the effectiveness of cyclic airfoil deformations. In order to achieve a more accurate analysis, Kerho [10] created several volume grids with variable droop leading edges and interpolated between grids to create a blade with partial droop at each time step. Such a method has improved accuracy over a lifting-line method in estimating the effectiveness of an airfoil deformation.

Pawar et al. [51] performed a comprehensive analysis for an active-twist rotor (ATR), applying a free-wake model developed by Bagai and Leishman [52] for computation of aerodynamic forces and moments. The structural model was represented by a one-dimensional beam, which was actively deformed by single-crystal piezoceramics. In forward flight cases at $\mu = 0.15$ and 0.30, it was predicted that over 90% of the vibratory shear forces could potentially be eliminated through use of ATR.

Jain et al. [14] performed a CFD/CSD analysis implementing loose coupling between CFD solver WIND-US-HELI and CSD solver RCAS. A delta-loads technique [49, 53, 54] was applied for trim convergence. Various simulations were performed to examine the effects of active twist, trailing-edge deflection (TED), and leading-edge deflection (LED) on rotor performance. Blade deflections were computed via the conventional one-dimensional beam model. In order to define the LED and TED, points at the leading edge or trailing edge were shifted downward. A set of B-splines were defined to smoothly deform the airfoil to conform to the leading-edge and trailing-edge points.

Padthe et al. [55] conducted a computational analysis that predicted a potential reduction in vibratory loads as large as 92% using a single $0.015c$ deployable Gurney flap between $86\%R$ and $90\%R$, using an active $0.2c$ trailing edge flap on a four-bladed rotor at advance

ratio $\mu = 0.15$ and descending flight angle of 6.5°, with weight coefficient $C_W = 0.005$. Jain et al. [14] implemented CFD/CSD coupling to predict rotor loads affected by active leading edge and trailing edge deflections. They demonstrated that LED is well suited to high-thrust forward flight conditions, in which power could be reduced by 12.4% and vibratory hub loads could be reduced by 40%. TED is better suited for high speed forward flight, as 30% to 54% reduction in vibratory loads, 4.7% to 7.3% gain in lift-to-drag, and 2.3% to 3.3% reduction in power were observed.

Ravichandran et al. [56] performed a comprehensive analysis of rotor blades with slats, modeled as Euler-Bernoulli beams with lifting-line aerodynamic loads applied. At high advance ratios, $\mu = 0.2 - 0.4$, results indicated that the leading edge slats could increase maximum lift capabilities by 25-30% and reduce torque by 10-20%.

Other efforts have improved structural modeling for components that cannot accurately be reduced to a one-dimensional model. Near the hub there are components with smaller aspect ratios and certain constraints in which a beam approximation is not appropriate. Datta and Johnson [57] developed a three-dimensional brick finite-element method (FEM) for rotorcraft applications that may improve structural accuracy in CFD/CSD coupling. This method is particular beneficial for structural components with smaller aspect ratios, such as the pitch link and hub joint. Although it has a much larger computational cost than a beam model analysis, the computational expense is of the same order of magnitude as CFD analysis over a given azimuthal interval, and grid partitioning for parallelization has been developed for reduction of computation wall time and efficient use of processors in future CFD/CSD coupling efforts. Load distributions have been applied for testing purposes, but CFD/CSD coupling that implements this structural model is yet to be developed.

Flutter has been evaluated via CSD/CFD analysis [58, 59] to improve on the classical analysis, particularly in cases where nonlinear aerodynamic behavior is significant. Taylor et al. [60] investigated two structural models for CFD/CSD aeroelastic analysis: mode extraction and mass/stiffness matrix analysis. It was determined that the latter of these methods tends to provide more consistent results, while in a modal analysis it is often unclear *a priori* how many modes are necessary to obtain an equally accurate solution.

Parabolic camber deformation has also been tested for vibratory load reduction. In 2008 Palacios and Cesnik investigated the effects of camber deformation on harmonic loading, and determined that the camber deformation due to aerodynamic loads is usually small except for very thin airfoils [61]. They modeled a 2.0 x 0.2 m cantilevered strip of aluminum and performed an aeroelastic simulation at 25 m/s sea-level airflow at 5° angle of attack using a comprehensive CSD analysis. The aluminum strip was perturbed by 1 degree angle of attack over $\pi/10$ seconds. Without camber actuation the system was very lightly damped, and after several seconds the amplitude of normal force oscillation showed very little attenuation. They applied a harmonic parabolic camber force, or camber bi-moment, at 70% span to create harmonic camber actuation. They were able to reduce the normal force oscillations by an order of magnitude within 2 seconds. Their results demonstrated the capability of CFD/CSD coupling for analyzing the effects of camber actuation in vibratory load reduction.

Kumar and Cesnik [62] developed an optimization technique for use with the University of Michigan, Nonlinear Asymptotic Beam Solver - Aerodynamics (UM/NLABS-A) to optimize camber actuation frequency and phase for minimization of vibratory loads and improvement of rotor performance at an advance ratio of 0.33. A combination of surrogate models and an Efficient Global Optimization (EGO) technique were applied to determine optimal control settings. Results indicated that 4 per revolution vertical forces could be reduced by 99% with optimized camber actuation, and 50% of the combined vibratory forces and moments could be eliminated simultaneously. In addition, optimized camber actuation was determined for minimized shaft torque to improve performance by 3.5%. The EGO method requires numerous samples of actuation schedules and magnitudes, and would not be computationally feasible for application in CFD/CSD simulation. However, a solution obtained via a comprehensive analysis may serve as a preliminary solution which could be further optimized in a CFD/CSD analysis by applying other techniques, such as a Jacobian-based approach in which phase and magnitude are adjusted based on their influence on vibratory loads.

Murua et al. [63] conducted a two-dimensional aeroelastic analysis using a Peters aerodynamic model [64] to include pitch, plunge, and parabolic camber modes. Numerical results indicated that camber effects alone can cause flutter, and that the camber mode greatly influences stability boundaries when coupled with pitch and plunge modes. This linearized aerodynamic formulation is limited to thin airfoils with subsonic, attached flow. Transonic flow, dynamic stall, and wake effects add to the physical complexity of the system in forward or maneuvering flight conditions.

Dunn and Dugundji [65] addressed the influence of nonlinear effects on flutter behavior by applying a semi-empirical unsteady aerodynamic theory developed at the Office National d'Etudes et de Recherches Aérospatiales (ONERA). They conducted aeroelastic simulations of a cantilevered wing in the nonlinear flutter regime and were able to match trends of experimental data. The same method was later applied to a rotor with hingeless composite blades in hover, by Kim and Dugundji [66]. Using this method they were able to predict the aeroelastic behavior of dynamic stall.

For types of flows that include multiple complex phenomena, such as a stalled flexible airfoil in transonic flow, a full solution of the Navier-Stokes equations remains the most reliable solution method for accurately obtaining performance characteristics. Therefore, a coupled CFD/CSD analysis including aeroelastic camber deformations is expected to provide more accurate performance predictions than linearized thin airfoil theory.

1.4 Influence of Wake Vorticity and Turbulence

The influence of a rotor wake can have significant effects on performance and blade loading, as demonstrated by Caradonna and Tung [67]. They constructed a hovering rotor and conducted tests at various Mach numbers inside an enclosed chamber in which the wake flowed into an exhaust duct to avoid recirculation effects. Pressure distributions on the blade were tabulated, along with locations of tip vortices, and it was evident that tip vortex strength and position had a large effect on the spanwise blade loads. This experiment demonstrated that correctly modeling tip vortices is necessary for accurate blade load prediction.

Until the mid-1990's the nature of turbulence in tip vortices was debated. In 1996 a

wing-tip experiment performed by Devenport et al. [68] conclusively determined that a tip vortex core, though initially very turbulent due to roll-up of the boundary layer, quickly becomes laminar due to large strain rates in the core, which drive the core toward rigid-body-rotation. Thus near the core very little turbulence production is observed. In 1997 Chow et al. [69] confirmed the results of Devenport. Utilizing "triple-wire" probes, they were able to measure individual components of the Reynolds stress. In doing so they found that the tip vortex is not isotropic, as there is a 45° rotation in the $v'w'$ turbulent stress with respect to the corresponding strain. Later experiments by Ramasay et al. [70], in which fluid velocities were measured with dual-plane stereoscopic particle image velocimetry, confirmed the anisotropic behavior of tip vortices. Ramasay et al. [70] determined that shear stresses decreased and shifted away from the center of the vortex as its age increases. These findings indicate that numerical simulations in which large amounts of turbulence are present in the vortex core are erroneous, and that assumptions based on isotropic vorticity are incorrect. The re-laminarization of the tip vortex preserves the maximum velocities in the vortex and prevents its dissipation.

1.5 Influence of Test Facility

In order to evaluate the influence of active controls, tests must be performed in an environment in which the source of unsteady blade loads can be determined. In enclosed facilities this can be a challenge, as aperiodic loads can result from interference of test facility components or vorticity in the recirculating wake. It has been shown through experimentation [71, 72, 73] that nearby components, such as walls, can alter rotor performance significantly and introduce large fluctuations in hub loads. In computational efforts the primary challenges include accurately resolving complex wake features in the recirculating wake and accurately modeling turbulence properties in the wake.

In an experiment conducted by Felker and Light [71], the presence of a wing under the rotor increased the thrust by 3%. When an image plane was added $1.21R$ from the rotor axis the figure of merit reduced 1.6% less than in the isolated case. In subsequent investigations experimental data [72] and computational results [73] reveal that the combination of a wing

and image plane can cause small regions of recirculation, also known as "fountain flow", near the image plane. Although the image plane does not affect the mean inflow over most of the rotor disk, lift is greatly reduced on the outboard portion of the blade when the blade tip is in the fountain flow region. The induced velocity through the rotor causes a reduction in time-averaged thrust and an increase in vibratory loading.

The influence of the wake in ground effect was quantified at low advance ratios by Ganesh [74], who found that at very low advance ratios the wake is reingested through the rotor, while at slightly higher advance ratios a ground vortex forms on the upwind side of the rotor. The ground vortex entrains vorticity from the tip vortices and can increase to over 4 times the magnitude of the tip vortices. Ganesh [75] was also able to determine that long-period unsteadiness in the ground vortex resulted in increased unsteadiness of the loads in ground effect. These indicate that even at low advance ratios the influence of the ground can cause unsteady loading via a different phenomenon other than recirculation.

In an enclosed test facility the effects of fountain flow can significantly alter time-averaged and unsteady loads even if the walls are located far from the rotor. Shivananda [16] investigated the effects of recirculation and applied a method for reducing these effects. He tested a series of rotors ranging in diameter from 7 inches to 14 inches in two configurations: a "free air" configuration inside a large room, and an enclosed configuration inside a chamber measuring 27 inches wide, 27 inches long, and 62 inches tall. Inside the chamber the observed thrust was reduced by as much as 25% compared to the free air value, and variations in thrust were as large as 8% of the mean value. A honeycomb structure with a hole cut out for the wake region was installed downstream of the rotor to straighten the return flow, and as a result the thrust inside the chamber increased to 99% of the free air value. Thus, the effects of recirculation, though significant in some cases, may be largely reduced by taking proper measures to reduced vorticity and velocity fluctuations in the return flow.

Piziali and Felker [17] later conducted a similar experiment on a larger-scale rotor of diameter 6 feet in a pentagonal room in which each wall was $6R$ from the hub at the nearest point and the ceiling height was $30R$. Although the room was very large in comparison to

the rotor size, significant oscillations in thrust, torque, and flapping (12% peak-to-peak) were measured. Applying the same approach as Shivananda, a honeycomb structure was placed downstream of the rotor with a cutout for the wake region. A layer of plastic window screening was laid on top of the honeycomb structure to smooth random variations in return flow by providing flow resistance proportional to velocity. This modification decreased variations in normal hub forces to within 1.5% of the mean values. The experiments of Shivananda and of Piziali and Felker demonstrate the large influence that wake recirculation can have on hub loads inside a closed facility.

Timm [76] demonstrated experimentally that when a rotor is near the ground even small obstructions can cause local recirculation. Timm explored several factors, including size of the obstruction, distance from the rotor, and height of the rotor above the ground. The experiment indicated that when a rotor is near the floor that relatively small protrusions can have a significant effect on recirculation patterns.

1.6 Computational Modeling of a Rotor Inside a Test Facility

Computational simulations can provide some insight into what configurations may be most suitable for evaluation of vibratory loads. To provide accurate computational modeling it must be verified that the wind tunnel and test rig geometry and the turbulence are properly modeled.

1.6.1 Wake and Wind Tunnel Modeling

The long-term influence of the wake can significantly alter rotor loads. In free wake simulations by Kini and Conlisk [77] in 2002, it was observed that even in free air that variations in thrust were present due to interaction of the vortices. In climb tip vortices were spaced a sufficient distance to preclude interaction of the vortices, resulting in steady thrust. However, simulations of one-bladed and two-bladed rotors in hover demonstrated the tendency of vortex pairs to approach each other when they are close in proximity. This interaction can lead to aperiodic wake solutions, which alter the induces velocity and cause variations in hub loads.

Singh and Brown [78] performed CFD simulations for a hovering rotor using an actuator

disk rotor model to calculate pressure loads. The observed impact of the test stand and shroud was a 6% increase in thrust and 3% increase in torque compared to an isolated rotor. The test stand and ground caused contraction of the rotor wake, altering the induced inflow. After inverting the rotor the thrust and torque predictions were nearly identical to those of the isolated rotor case.

Computational analyses of a rotor inside a test facility that include solid boundaries of the ceiling, walls, and floor are limited, but recent efforts are being made toward understanding the influence of tunnel walls. For example, Romander et al. [79] simulated a rotor in forward flight with free air boundary conditions and with facility walls. They observed that at $\mu = 0.15$ the torque prediction increased by approximately 5% when including the facility walls in the simulation model.

These computational efforts demonstrate the necessity for further evaluation of the physics in an enclosed facility and investigation of computational requirements for accurately simulating such cases. If accurate results can be achieved through computational simulations, then hub loads of a rotor in a test facility can be predicted before conducting experiments to determine if the configuration is suitable. In addition, computational studies may provide insight into the source of vibratory loads. Proper adjustments can then be made to reduce vibratory loads when configuring the experiment.

1.6.2 Turbulence Modeling

In free air Reynolds-Averaged Navier-Stokes (RANS) turbulence models can provide accurate results if the flow remains attached to solid surfaces. In these cases the wake travels downstream, and the modeled and resolved turbulence have little influence on surface pressures. Inside an enclosed facility the wake recirculates, and the influence of turbulence model on the rotor loads is unknown. Models that rely on higher fidelity turbulence resolution require much more temporal and spatial resolution to accurately predict flow features. Direct Numerical Simulation (DNS) must be implemented to completely resolve turbulent features. However, DNS simulations are extremely computationally expensive, and this limits simulations to very small domains for a very short physical time, relative

to the duration of a single rotor revolution. Turbulence models greatly reduce the computational expense, but the accuracy has a high level of dependence on geometry and flight conditions. Modifications have been developed for various turbulence models to improve prediction of turbulence properties. These models are often tuned to wall-bounded flows using experimental data, and although they may be very useful in some circumstances, their performance is case-dependent. In many cases RANS models have the ability to produce reasonably accurate results with a relatively small computational cost. RANS models are primarily tuned for boundary layer flow in steady-state cases. In Unsteady RANS (URANS) simulations a RANS turbulence model is applied to find Reynolds-averaged velocities in the boundary layer, but a global time step is applied for uniform time marching so that large-scale unsteady flow can be resolved. Computational modeling of turbulence production and dissipation is generally based on distance from the nearest viscous surface. However, in the wake this dependence is non-physical, since turbulence is affected to a greater extent by flow features far from the solid bodies. In general, RANS and URANS models are not physically valid in separated flow and other regions of vorticity-dominated flow [80].

One of the greater challenges in capturing tip vortices is limiting the dissipation of the vortices to physically-accurate levels. In turbulent rotor simulations Duraiswamy and Baeder [81] identify two sources of tip vortex dissipation: 1) numerical dissipation due to spatial discretization of the computational grid, and 2) viscous dissipation. The first source of dissipation can be remedied by increasing the grid resolution and spatial order of accuracy. The second source of dissipation is dependent on fluid viscosity, and in turbulent simulations the viscous dissipation relies heavily on the turbulence model that is applied. These two sources of dissipation are discussed in more detail below.

While it is simple to uniformly refine a grid, the number of grid nodes, and therefore the computational expense, increase rapidly as the grid spacing is reduced. The tip vortex core, defined as the distance from the minimum value of the cross-flow velocity to the maximum value, has been experimentally measured to be approximately $10\%c$ [82, 83] shortly after leaving the trailing edge. In a computational simulation of the Tilt Rotor Aeroascoustic Model (TRAM) Holst and Pulliam [84] estimated that providing a uniform grid spacing

that would guarantee 10 nodes across the vortex core in the wake (for a distance of 20 chord lengths below the rotor) would require 8 billion nodes in the wake alone. Given the current state of computational capabilities it is not feasible to perform simulations with a grid this size. Therefore, in order to accurately capture tip vortices, it is necessary to refine the grid in a more intelligent manner. Holst and Pulliam have modified the CFD solver OVERFLOW2, developed by Benek et albbbbbb. [85] and Buning et al. [86] – a Navier-Stokes solver for overset structured grids. They implemented an adaptive mesh refinement (AMR) [87] methodology where an off-body Cartesian grid is first generated and then refined. A threshold may be specified for flowfield gradients, so that in regions where the threshold is exceeded, overset meshes are added to the grid set. The grid can be refined by an arbitrary number of levels to comply with the threshold limit. The grid set is updated periodically to maintain optimal refinement as the vortices move. With two levels of grid adaptation Holst and Pulliam reduced the error in figure of merit prediction from 6% to 4%, and with increased nearbody grid resolution and three levels of grid adaptation, they reduced the error to 1.3%.

Following this methodology of AMR, the High Performance Computing Institute for Advanced Rotorcraft Modeling and Simulation (HI-ARMS) and the Air Vehicles element of the Computational Research and Engineering for Acquisition Tools and Environments (CREATE-AV) [88] developed a multi-disciplinary computational tool called Helicopter Overset Simulations (Helios) [89]. The adaptive mesh aspect of Helios is similar to that of OVERFLOW2; however, the solution for a near-body unstructured grid is resolved by the CFD solver NSU3D developed at the University of Wyoming [90, 91], while the off-body Cartesian grid is obtained by the SAMARC solver developed by Lawrence Livermore National Laboratory [92, 93] and the NASA Ames Research Center [94]. This overset method simplifies grid generation for complex geometries by applying unstructured grids near surfaces while taking advantage of the computational efficiency of Cartesian grids in off-body regions. To account for structural deformations, a loose-coupling technique using delta-loads is implemented, with the Rotorcraft Comprehensive Analysis System (RCAS)

developed by the U.S. Army Aeroflightdynamics Directorate (AFDD) and Advanced Rotorcraft Technology, Inc. (ART) [95]. The three-dimensional surface patch forces from NSU3D are applied to a one-dimensional beam model in RCAS to compute aeroelastic deformations. Kamkar and Wissink [96] explored the numerical accuracy of the solver for various temporal and spatial resolutions and applied the Helios methodology to the TRAM rotor, and they succeeded in predicting figure of merit with 0.4%. Wissink et al. [97] further extended the capabilities of Helios for coupling with CSD solver CAMRAD II, and application of detached eddy simulation (DES) turbulence modeling in the near-body grid.

Another source of dissipation is fluid viscosity, and in turbulent simulations the viscous dissipation relies heavily on the turbulence model that is applied. In addition to molecular viscosity, many turbulence models prescribe an eddy viscosity term, which is an artificial viscosity meant to approximate the influence of turbulent mixing caused by features too small for the grid to resolve. Eddy viscosity models are commonly used for modeling boundary layer turbulence, as the flow features are very small in this region. However, care must be taken to ensure that the levels of eddy viscosity are valid and do not adversely affect the solution.

Réthoré [98] explored the influence of ambient eddy viscosity on the axial induction of a wind turbines with diameters of 35–40 m and freestream velocity of 8 m/s. He performed a numerical actuator disk analysis to determine a "threshold value" for eddy viscosity of the ambient flow. Above the threshold value the eddy viscosity had significant influence on the axial induction factor and the velocity profile of the wake. Réthoré determined that the threshold value in the wind turbine simulations was 0.1 kg/(m-s), which is equivalent to a nondimensional value of $\mu_t = 5.6\text{E}3$. He also found that in the presence of atmospheric turbulence, LES provided velocity profiles and turbulence levels comparable to experimental measurements, while an unsteady $k - \epsilon$ RANS model performed poorly. It was concluded that the URANS simulation was unable to simultaneously model the large-scale atmospheric turbulence and the small-scale turbulence in the wake, and was therefore not suitable for wind turbine simulations with turbulent freestream flow. Similar results were observed in an analysis performed by Gundling et al. [99] in an actuator disk simulation performed

with DiskFloW. Gundling et al. also determined that replacing the actuator disk with discrete blades improved turbulence levels in the wake and predictions of wind speed deficits compared to experimental measurements.

1.6.2.1 Unsteady Reynolds-Averaged Navier-Stokes Model

Many rotor simulations produce acceptable predictions for blade loading using unsteady RANS. To apply Reynolds-averaging the variables ρ and p are separated into mean ($\overline{f}$) and fluctuating (f') components. The u_i, e, and h terms are decomposed into Favre or mass-averaged values, such that $\tilde{f} = \overline{\rho f}/\overline{\rho}$ and $f = \tilde{f} + f''$. The Favre-averaged Navier-Stokes equations can be written

$$\begin{aligned}
\frac{\partial \overline{\rho}}{\partial t} + \frac{\partial}{\partial x_j}\left(\overline{\rho}\tilde{u}_j\right) &= 0 \\
\frac{\partial}{\partial t}\left(\overline{\rho}\tilde{u}_i\right) + \frac{\partial}{\partial x_j}\left(\overline{\rho}\tilde{u}_j\tilde{u}_i\right) &= -\frac{\partial \overline{p}}{\partial x_i} + \frac{\partial}{\partial x_j}\left(\overline{t}_{ji} + \overline{\rho}\tau_{ji}\right) \\
\frac{\partial}{\partial t}\left[\overline{\rho}\left(\tilde{e} + \frac{1}{2}\tilde{u}_i\tilde{u}_i\right)\right] + \frac{\partial}{\partial x_j}\left[\overline{\rho}\tilde{u}_j\left(\tilde{h} + \frac{1}{2}\tilde{u}_i\tilde{u}_i\right)\right] &= \frac{\partial}{\partial x_j}\left(-q_{L_j} - q_{T_j}\right) - \frac{\partial}{\partial t}\left(\overline{\rho}k\right) \\
&\quad + \frac{\partial}{\partial x_j}\left(\overline{t_{ji}u_i''} - \overline{u_j''\rho u_i''u_i''}\right) \\
&\quad + \frac{\partial}{\partial x_j}\left[\tilde{u}_i\left(\overline{t}_{ij} - \overline{\rho}\tau_{ij} + k\right)\right], \qquad (5)
\end{aligned}$$

where the Reynolds stress tensor τ_{ij} is defined $\overline{\rho}\tau_{ij} = -\overline{\rho u_i'' u_j''}$, the turbulence kinetic energy k is defined $\overline{\rho}k = \frac{1}{2}\overline{\rho u_i'' u_i''}$, and the turbulent transport of heat is $q_{T_j} = \overline{\rho u_i'' h''}$. The $\overline{t_{ji}u_i''}$ and $\overline{u_j''\rho u_i''u_i''}$ terms are the molecular diffusion and turbulent transport of turbulence kinetic energy, and are neglected. Closure for the Reynolds-stress tensor is obtained via the Boussinesq approximation [100] as

$$\tau_{ij} = 2\nu_t S_{ij} - \frac{2}{3}k\delta_{ij} \qquad (6)$$

The Menter SST turbulence model solves two equations that model the turbulence kinetic energy k and the dissipation rate per unit turbulence kinetic energy ω. The equations

implemented to resolve these equations are

$$\begin{aligned}
\frac{\partial}{\partial t}(\rho k) &= \tau_{ij}^{RANS}\frac{\partial u_i}{\partial x_j} - \beta^*\rho\omega k + \frac{\partial}{\partial x_j}\left[\left(\mu + \sigma_k\mu_t^{RANS}\right)\frac{\partial k}{\partial x_j}\right] \\
\frac{\partial}{\partial}(\rho\omega) + \frac{\partial}{\partial x_j}(\rho u_j\omega) &= \frac{\gamma\rho}{\mu_t}\tau_{ij}^{RANS}\frac{\partial u_i}{\partial x_j} - \beta\rho\omega^2 + \frac{\partial}{\partial x_j}\left[\left(\mu + \sigma_\omega\mu_t^{RANS}\right)\frac{\partial\omega}{\partial x_j}\right] \\
&\quad +2(1-F_2)\rho\sigma_{\omega 2}\frac{1}{\omega}\frac{\partial k}{\partial x_j}\frac{\partial\omega}{\partial x_j}, \qquad (7)
\end{aligned}$$

where the $RANS$ subscript indicates a variable based on a RANS formulation. The constants in Eq. 7 are $\beta^* = 0.09$, $\sigma_k = 0.85$, $\sigma_\omega = 0.5$, $\sigma_{\omega 2} = 0.856$, and F_2 is defined as

$$F_2 = \tanh\left\{\left[\max\left(\frac{2\sqrt{k}}{\beta^*\omega y}, \frac{500\nu}{y^2\omega}\right)\right]^2\right\}. \qquad (8)$$

where y is the distance to the nearest wall. The original formulation of Menter [101] models the term $\tau_{ij}^{RANS}\frac{\partial u_i}{\partial x_j}$ based on the vorticity magnitude $\Omega = \sqrt{\Omega_{ij}\Omega_{ij}}$ where

$$\Omega_{ij} = \frac{1}{2}\left(\frac{\partial\overline{u}_i}{\partial x_j} - \frac{\partial\overline{u}_j}{\partial x_i}\right). \qquad (9)$$

Recent modifications to the model [102] replace Ω with the strain rate $S = \sqrt{2S_{ij}S_{ij}}$ where

$$S_{ij} = \frac{1}{2}\left(\frac{\partial\overline{u}_i}{\partial x_j} + \frac{\partial\overline{u}_j}{\partial x_i}\right). \qquad (10)$$

URANS turbulence models typically base the turbulence kinetic energy production k on either vorticity or strain rate. Spalart [80] demonstrates that while vorticity is more commonly used, the actual physics of turbulence production are based on strain rate. In the boundary layer the choice of vorticity or strain-rate makes little difference, since the values are similar in that region. However, in other regions where vorticity is much larger than the strain rate, k can be over predicted in a vorticity-based model. The original k-ω SST model presented by Menter [101] was based on vorticity. Moore [103] declares that this model produces realizable turbulence properties if strain rate replaces vorticity and the blending function is neglected. Recently the SST model has been modified by Smirnov and Menter [104] with a formulation based on strain rate.

Dacles-Mariani et al. [105, 106] introduced a method for reducing large non-physical values of turbulence kinetic energy in tip vortex cores by replacing Ω terms with $(\Omega +$

$2\min(0, |S| - |\Omega|)$ in production terms. This limits production in regions where vorticity is much larger than strain rate, such as in the tip vortex, while having little influence in regions where vorticity and strain rate are approximately equal, such as the boundary layer. Application of the method resulted in a reduction of tip vortex dissipation and reduced the error in total velocity in the tip vortex core from 25% to less than 3%. While this method improves turbulence modeling of some URANS models, more physically valid models, such as large eddy simulation (LES) can be also be applied for improved results.

1.6.2.2 Large Eddy Simulation Model

Large eddy simulation was originally proposed by Smagorinsky [107] for weather forecasting applications. In LES larger eddies are resolved while subgrid-scale turbulence is modeled. Since LES can still be computationally intense in boundary layer regions, hybrid methods have been formulated in which URANS equations are applied in viscous regions dominated by small-scale turbulence features, while LES is applied in vorticity-dominated regions where larger-scale turbulence features are present. Detached Eddy Simulation (DES) is a hybrid method in which the transition from URANS to LES is determined by grid metrics. Travin et al. [108] demonstrated that DES is able to capture wake features in flow past a cylinder that resemble those in experiments with much better fidelity than URANS simulations. In Hybrid RANS-LES (HRLES) simulations the RANS-to-LES transition is determined from flow properties rather than grid metrics. A HRLES model was implemented in FUN3D by Lynch [109], in which significant improvements in the wake of a cylinder were observed, and drag predictions were greatly improved in comparison to URANS simulations. The HRLES model implemented by Lynch blends the Menter Shear Stress Transport (SST) [101] and the Smagorinsky approach [107] for Large Eddy Simulation [109, 110].

The LES formulation was successfully implemented by Lynch [109] to solve a single equation for resolving the subgrid scale turbulence kinetic energy:

$$\frac{\partial}{\partial t}\left(\overline{\rho}k^{SGS}\right) + \frac{\partial}{\partial x_j}\left(\overline{\rho}\tilde{u}_j k^{SGS}\right) =$$
$$\tau_{ij}^{SGS}\frac{\partial \tilde{u}_i}{\partial x_j} - C_\epsilon \overline{\rho}\frac{\left(k^{SGS}\right)^{3/2}}{\Delta} + \frac{\partial}{\partial x_j}\left[\left(\frac{\tilde{\mu}}{Pr} + \frac{\mu_t^{SGS}}{Pr_t}\right)\frac{\partial k^{SGS}}{\partial x_j}\right], \tag{11}$$

where $C_\epsilon = 0.916$ and Δ is the characteristic length given by $\Delta = V_{cell}^{1/3}$ where V_{cell} is the dual cell volume. Subgrid scale eddy viscosity is

$$\nu_t^{SGS} = C_\nu \Delta \sqrt{k^{SGS}}, \tag{12}$$

where C_ν is a constant value 0.0667.

Kim and Menon [111] presented a localized dynamic kinetic energy model (LDKM) in which the C_ν and C_ϵ coefficients are solved at a test filter scale and then applied to the turbulence equations at the subgrid scale, rather than assuming a constant value. This model was first derived for incompressible flow and later extended for compressible flow by Menon and Patel [112].

Menon et al. [112] base the formulation on experimental results which indicate that the subgrid-stress tensor τ_{ij}^{SGS} at the grid level Δ and the Leonard's stress $L_{ij} = (\langle \overline{\rho} \tilde{u}_i \tilde{u}_j \rangle - \langle \overline{\rho} \tilde{u}_i \rangle \langle \overline{\rho} \tilde{u}_j \rangle)/\langle \overline{\rho} \rangle$ at the test filter level $\hat{\Delta}$ are self-similar, where $\langle f \rangle$ indicates application of the test filter to a variable f. Typically the test filter length is $\hat{\Delta} = 2\Delta$. In the LDKM method it is assumed that the subgrid stress $\hat{\tau}_{ij}^{SGS}$ is also self similar, so that

$$\hat{\tau}_{ij}^{SGS} = \hat{C}_L L_{ij}, \tag{13}$$

where $\hat{C}_L$ is a constant that is assumed to be 1 in computations performed by Menon et al. If the sub-scale kinetic energy $\hat{k}$ at the test filter is defined as

$$\hat{k} = \frac{1}{2} \left(\frac{\langle \overline{\rho} \tilde{u}_k^2 \rangle}{\langle \overline{\rho} \rangle} - \frac{\langle \overline{\rho} \tilde{u}_k \rangle^2}{\langle \overline{\rho}^2 \rangle} \right) \tag{14}$$

then the Leonard's stress (and test-level stress tensor) can be written as

$$L_{ij} = \langle \tau_{ij}^{SGS} \rangle = -2 \langle \overline{\rho} \rangle C_\nu \sqrt{\hat{k}} \hat{\Delta} \left(\langle \tilde{S}_{kk} - \frac{1}{3} \langle \tilde{S}_{kk} \rangle \delta_{ij} \right) + \frac{2}{3} \langle \overline{\rho} \hat{k} \delta_{ij} \rangle. \tag{15}$$

In the set of equations above the only unknown is C_ν; therefore Menon et al. implement a least-squares method presented by Lilly [113]:

$$C_\nu = -\frac{L'_{ij} M_{ij}}{2 M_{ij} M_{ij}}, \tag{16}$$

where

$$L'_{ij} = L_{ij} - \frac{2}{3} \langle \overline{\rho} \hat{k} \delta_{ij} M_{ij} = \langle \overline{\rho} \sqrt{\hat{k}} \hat{\Delta} \left(\langle \tilde{S}_{ij} \rangle - \frac{1}{3} \langle \tilde{S}_{kk} \rangle \delta ij \right). \tag{17}$$

The C_ϵ coefficient is determined in a similar manner:

$$C_\epsilon = \frac{\hat{\Delta}\,(\mu+\mu_t)}{\langle\overline{\rho}\rangle\hat{k}^{3/2}}\left(\langle\tilde{T}_{ij}\frac{\partial\tilde{u}_j}{\partial x_i}\rangle - \langle\tilde{T}_{ij}\rangle\langle\frac{\partial\tilde{u}_j}{\partial x_i}\rangle\right), \tag{18}$$

where the tensor $\tilde{T}_{ij}$ is defined as

$$\tilde{T}_{ij} = \left[\frac{\partial\tilde{u}_i}{\partial x_j} + \frac{\partial\tilde{u}_j}{\partial x_i} - \frac{2}{3}\frac{\partial\tilde{u}_k}{\partial x_k}\delta_{ij}\right]. \tag{19}$$

The filter is applied for every grid point at each time step to determine the local coefficients. This method has been successfully demonstrated by Kim and Menon [111] and by Menon and Patel [112], who obtained accurate results for incompressible and compressible turbulent flows, respectively.

1.6.2.3 Hybrid Blending Function

In many HRLES approaches it is assumed that the URANS and LES regions transition can be applied through a simple blending function:

$$\vec{G}_T^{HYBRID} = \mathcal{F}\vec{G}_T^{RANS} + (1-\mathcal{F})\vec{G}_T^{SGS}, \tag{20}$$

where $\mathcal{F}$ is the blending function, and is equal to 1 in purely URANS zones and 0 in purely LES zones.

The work of Sánchez-Rocha [114] indicates that simply blending the terms is not sufficient, since the turbulence that was modeled in the URANS zone is not immediately resolved upon transitioning to the LES zone. Non-physical effects were reported to be greatest in regions in which there was an abrupt transition from URANS to LES. Sánchez-Rocha derived specific hybrid terms which he included in the governing equations for a more physical accurate model. He determined, however, that the computational expense of solving the exact equations too great for practical purposes and instead proposed approximation terms. Although implementation of the hybrid terms outlined by Sánchez-Rocha is beyond the scope of this research, it is worth noting that without including the mixing terms the flow solution was more sensitive to the blending function.

Sánchez-Rocha applied various blending functions, two of which have the following form:

$$\mathcal{F}_o(y) = \frac{1}{2}\left\{1 - \tanh\left[\frac{C_1(y/L_y - C_2)}{(1-2C_2)y/L_y + C_2}\right] / \tanh(C_1)\right\}, \tag{21}$$

where C_1 and C_2 are selected to be 2 and 0.2, respectively, and $\mathcal{F}_o$ is based on the function defined by Kawai and Fujii [115], and is used in blending functions $\mathcal{F}_1$ and $\mathcal{F}_2$. Sánchez-Rocha implemented five blending functions and compared the results of each:

$$
\begin{aligned}
\mathcal{F}_1(y) &= \begin{cases} \mathcal{F}_o(y) & \text{for } y \le d = L_y/4 \\ 0 & \text{for } y > d \end{cases} \\
\mathcal{F}_2(y) &= \mathcal{F}_o(y), \quad d = L_y \\
\mathcal{F}_3(y) &= \begin{cases} 1 & \text{for } y \le L_1 \\ 1 - (y - L_1)/(L_2 - L_1) & \text{for } L_1 \le y \le L_2 \\ 0 & \text{for } y > L_2 \end{cases} \\
\mathcal{F}_4(y) &= e^{-y/L_y} \left[\cos(5\pi y/L_y) + 1\right]/2 \\
\mathcal{F}_5(y^+) &= \begin{cases} 1 & \text{for } y^+ < 45 \\ 0 & \text{for } y^+ \ge 45 \end{cases},
\end{aligned}
\tag{22}
$$

where L_y is the dimension of the grid normal to the viscous wall and is equal to 3δ to 3.5δ (where δ is boundary layer thickness) for Reynolds numbers 1400 to 3300. For $\mathcal{F}_3$, blending terms are set as $L_1 = L_y/100$ and $L_2 = L_y/3$. The blending functions in these cases are all based on distance from the wall.

When Sánchez-Rocha did not apply hybrid terms skin friction was under predicted by HRLES simulations by 2–14%, depending on the blending function, while the error was only 1.5–5.8% when hybrid terms were included.

For the HRLES model implemented in FUN3D there are currently two blending functions simultaneously applied to different turbulence terms. These functions are based on turbulence properties rather than distance from the nearest viscous surface. The first function,

$$
\begin{aligned}
x &= \max\left(\frac{\sqrt{k}}{\beta^*\omega y}, \frac{500\nu}{y^2\omega}\right) \\
\mathcal{F}_1 &= \tanh(x^4),
\end{aligned}
\tag{23}
$$

is applied to turbulence production terms. The second function,

$$
\begin{aligned}
x &= \max\left(2\frac{\sqrt{k}}{\beta^*\omega y}, \frac{500\nu}{y^2\omega}\right) \\
\mathcal{F}_2 &= \tanh(x^2),
\end{aligned}
\tag{24}
$$

is applied to turbulence eddy viscosity. While these have been demonstrated to greatly improve results [116] compared to the URANS equations in many cases, in other cases non-physical results may result in zones where location of the RANS-to-LES transition is very different between the blending functions.

In this research the Menter-SST model is used for forward flight cases, two-dimensional cases, and hover cases, as specified. In enclosed test facility cases, although the flow is attached on the blade surface, there are large regions of flow separation from nearby components, which may influence blade loads. Because URANS turbulence models are only accurate for attached flow, the HRLES model is applied in enclosed facility cases for improved turbulence modeling in the wake.

1.6.2.4 Realizability Constraints

In many instances turbulence models can produce turbulence properties which are not physically possible. Non-realizable properties can be produced due to approximations of the turbulence model and numerical error. Realizability constraints are often enforced for numerical stability and more realistic predictions of turbulence kinetic energy. A set of conditions that should be met to ensure physically realizability in two-equations RANS equations is outlined by Vreman [117]:

$$\begin{aligned} \tau_{ii} &\geq 0 \\ (\tau_{ij})^2 &\leq \tau_{ii}\tau_{jj} \quad \text{for} \quad i \neq j \\ \det(\tau_{ij}) &\geq 0. \end{aligned} \tag{25}$$

Equation 25 implies that the turbulence kinetic energy must be greater than or equal to zero. Equation 25 can also be used to determine other constraints for turbulence properties, based on the turbulence model, as described below.

Menter [101] proposed limits for turbulence kinetic energy and eddy viscosity to eliminate nonphysical buildup of eddy viscosity in stagnation regions and improve numerical

stability:

$$P_k = \min(P_k, C_l D_k)$$
$$\mu_t \leq \frac{a_1 k}{\sqrt{2}|\Omega|}, a_1 = 0.31 \tag{26}$$

where P_k is turbulence kinetic energy production term, D_k is the dissipation term, and Ω is vorticity. In the original formulation $C_l = 20$ and $a_1 = 0.31$. These constraints were applied in the current version of FUN3D.

Realizability conditions have also been determined for the LES equations. Fang and Menon [118] derived realizability constraints for a Kinetic-Eddy Simulation (KES) approach. In most of the computational domain the KES formulation is similar to the LES formulation. In coarser regions where the grid scale is not sufficient for LES, the behavior of KES approaches that of Very Large Eddy Simulation (VLES). From the second realizability constraint (Eq. 25) Fang and Menon derived the constraint,

$$k^{SGS} \geq \frac{\sqrt{3}}{C_\alpha}\nu_t\sqrt{2S_{ij}S_{ij} - \frac{2}{3}S_{kk}^2}, \tag{27}$$

where C_α is the constraint coefficient which is taken as $C_\alpha = 1$ in the cited work. Fang and Menon utilized the third constraint (Eq. 25) to provide a limit on the coefficient C_ν used in Eq. 12 for computing eddy viscosity:

$$C_\nu = \min\left(C_\nu, \frac{1}{\sqrt{6}}\frac{\sqrt{k^{SGS}}/l^{SGS}}{\sqrt{S_{ij}S_{ij} - \frac{1}{3}S_{kk}^2}},\right) \tag{28}$$

where l^{SGS} is the turbulence length scale. As the value of l^{SGS} approaches Δ the KES formulation approaches LES; therefore, in Eq. 28, l^{SGS} is set to Δ when implementing this LES realizability constraint in FUN3D.

1.7 Contributions to State of the Art

Fully three-dimensional coupling between CFD and CSD solvers has not yet been applied to rotor applications. The primary objective of this research is to develop an interface for CFD/CSD coupling that communicates three-dimensional blade deformations and a three-dimensional distribution of forces on the blade surface. Rather than communicating

information at the quarter-chord, according to the standard convention, all information is exchanged at individual nodes and faces on the CSD and CFD surface meshes. Since the meshes are not identical, data interpolation is required for communication between each set of nodes. This type of interface permits both cross-sectional and spanwise aeroelastic coupling and facilitates the simulation of active controls that produce airfoil deflections.

Verification is achieved in part through a work conservation analysis across the interface and also by performing an aeroelastic stability analysis including pitch, plunge, and camber modes and comparing to analytical solutions. Computational hover and forward flight performance predictions are also compared with experimental data to verify blade torsion and flap bending aeroelastic behavior. In addition, response to camber actuation is verified by comparison to theoretical response as computed by Peters' finite-state theory for flexible airfoils. A stability analysis for varying camber stiffness in compressible flow is also demonstrated in two-dimensional analyses for a section of the HART blade.

Effects of camber actuation on blade deformations as well as hub loads are examined. Specifically, the vibratory load magnitudes are analyzed to determine the potential for camber actuation to be used for reduction in vibratory loading. Results of finite-state-based and CFD-based computations are compared to evaluate accuracy of the finite-state approach and determine any advantages of the CFD-based approach.

Simulations are performed inside a test facility configuration to determine the influence of the facility walls and components. Results are verified for free air and enclosed facility cases by comparing to experimental data from the HART II [119] and HOTIS [120] experimental tests. The influence of turbulence models and implementation of LDKM in the HRLES turbulence model are examined to determine requirements for physical results to be achieved during the simulation.

CHAPTER II

DESCRIPTION OF CODE

An interface was developed in which a distribution of forces over the entire wetted surface of the blade is transmitted from the CFD solver to the CSD solver, and then updated CFD surface mesh coordinates of the deformed blade are returned to the CFD solver. This coupling method permits communication of arbitrary force distributions and deformations in both the spanwise and chordwise directions. The capabilities introduced by this research include simulation of active camber and introduction of camber bending due to aerodynamic pressure distribution, inertial terms, and elastic stresses.

2.1 CSD Model – UM/NLABS

The CSD code chosen to demonstrate the coupling methodology presented in this thesis is the University of Michigan Nonlinear Active Beam Solver (UM/NLABS, simply called NLABS in this thesis). This CSD solver is ideal because it accurately and efficiently computes three-dimensional deformations of a rotor. The structural method implemented in NLABS separates a nonlinear three-dimensional blade structure into a series of two-dimensional blade sections and a nonlinear one-dimensional beam. By combining the two solutions, the deformed three-dimensional rotor blade surface can be recovered. This method was introduced by Cesnik and Hodges [121]. Structural properties of a cross section are computed by a finite-element analysis performed in the University of Michigan Variational Asymptotic Beam Sectional analysis (UM/VABS), and these properties are then utilized by NLABS for the cross-section analysis [13, 122]. This method of approximating three-dimensional blade deformations is much more computationally efficient than an equivalent three-dimensional structural method. NLABS can compute aerodynamic loads as well as prescribed forces that are applied to the structure. A finite-state model based on Peters' finite-state theory for flexible airfoils [64] is provided in NLABS for aeroelastic analysis at a much smaller computational cost, although it is of lower fidelity than CFD

computations. A comprehensive solution using the finite-state and structural models can be utilized as a fast approximation of blade deflections, motion, and an initial trim solution before coupling with FUN3D. Interface routines in NLABS contributed by Thepvongs et al. [123] facilitate the coupling procedure.

2.1.1 Structural Model

In the structural formulation of NLABS the rotor blade is modeled as a one-dimensional beam with its span along a reference line that may have curvature and twist. Deflections are solved via nonlinear beam equations so that large deflections can be accurately computed. Unlike typical methods for rotor blade analysis, the cross-section of the blade is allowed to dynamically deform.

To construct a three-dimensional model from the cross-section and beam deformations, a transformation of the cross-sectional reference frame is constructed. The method follows the formulation developed by Palacios and Cesnik [122]. A reference line r is defined along the dominant direction of the structure (such as the elastic axis or quarter chord of a rotor blade). Vector $\vec{r}$ is defined as the position of a point along r, and $\vec{x}$ is defined as the position vector for a point inside the undeformed three-dimensional structure, as illustrated by Palacios and Cesnik [122] in Fig. 6. A reference frame $\mathbf{b}$ is defined such that $\mathbf{b}_1(x_1)$ is tangent to r, and $\mathbf{b}_\alpha(x_1)$ defines the undeformed cross-section. For convenience, the subscript α is used to indicate indices 2 and 3. In this manner the position of a point in the undeformed structure has been separated into spanwise and cross-sectional components:

$$\vec{x}(x_1, x_2, x_3) = \vec{r}(x_1) + x_\alpha \mathbf{b}_\alpha(x_1). \tag{29}$$

In order to define the deformed structure, $\vec{X}$ is defined as the position after deformation of a particle initially at $\vec{x}$, and $\vec{R}$ is equal to the averaged value of $\vec{X}$ on the cross sections of r, defining the deformed reference line $\mathcal{R}$. Vector $\vec{B_1}$ is defined as the deformation tangent to $\mathcal{R}$, and $\vec{B_\alpha}$ is the deformation of $\vec{b}$. The deformed position of any point in the structure can then be defined as:

$$\vec{X}(x_1, x_2, x_3) = \vec{R}(x_1) + x_\alpha \vec{B}_\alpha(x_1) + \vec{w}(x_1, x_2, x_3), \tag{30}$$

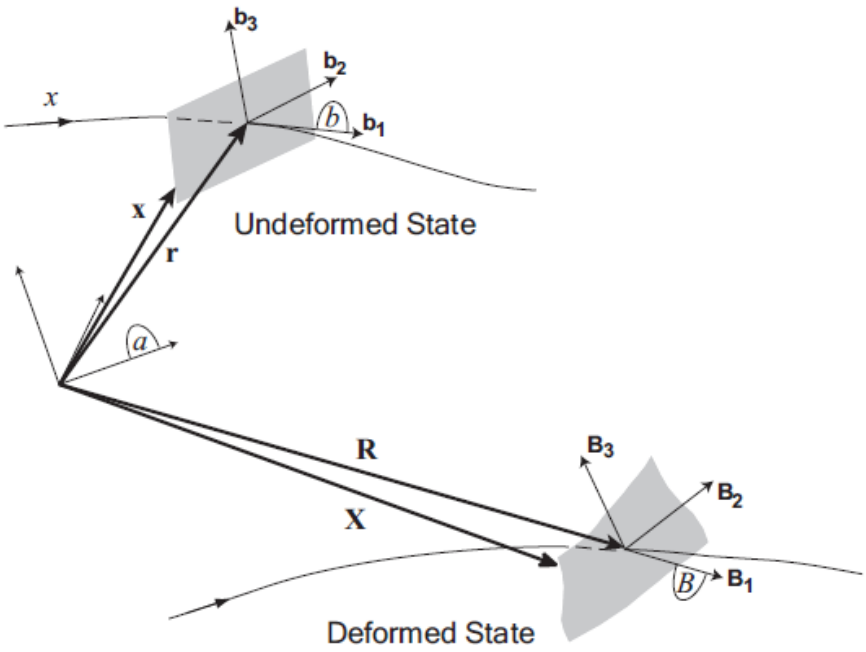

Figure 6: Structural deformation model of Palacios and Cesnik [122].

where $\vec{w}$ is a measure of the cross-sectional deformation after rigid-body translations and rotations have been removed. The warping, which is assumed to be small, is decomposed using a Ritz approximation into a set of assumed cross-sectional deformation functions and residual three-dimensional warping:

$$\vec{w}(x_1, x_2, x_3) = \sum_{m=1}^{N_q} q_m(x_1)\psi_{qm}(x_2, x_3) + \vec{w_r}(x_1, x_2, x_3). \tag{31}$$

Distributions of cross-sectional displacements $\{\psi_{qm}\}$ or "finite section deformation modes" form a complete and orthogonal set of cross-sectional deformation functions. The values of $\{q_m\}$ are the corresponding amplitudes. Kinematics of the one-dimensional beam are represented by torsion, the bending in two directions, and axial strain. These strains are written as vector $\vec{\epsilon}$:

$$\vec{\epsilon}(x_1) = \{\varepsilon_{11}, h_c\kappa_1, h_c\kappa_2, h_c\kappa_3\}, \tag{32}$$

where h_c is the characteristic length of the cross section, ε_{11} is the axial force strain measure and κ_i are the moment strain measures. The three-dimensional strain is written as a column matrix $\vec{\varepsilon}^T = \{\varepsilon_{11}, 2\varepsilon_{12}, 2\varepsilon_{13}, \varepsilon_{22}, 2\varepsilon_{23}, \varepsilon_{33}\}$, and combining components of the beam

deflections and cross-sectional warping, the strain is:

$$\varepsilon(\vec{x}) = \varepsilon_h \hat{w}(\vec{x}) + (h_c/R_C)\varepsilon_R \hat{W}(\vec{x}) + (h_c/L_C)\varepsilon_l \hat{w}', \tag{33}$$

where $\hat{w}$ is the nondimensional warping vector $\vec{w}/h_c$ and the matrix operators are defined by Cesnik and Hodges [121].

To perform a dimensional reduction, three characteristic lengths are identified: 1) the cross-sectional characteristic dimension, h_c; 2) the characteristic wavelength of the response along the reference line, L_c; and 3) the characteristic length of the initial curvature and twist, R_c. It is assumed that $h_c \ll L_c \approx R_c$. The cross-sectional characteristic length $\hat{h_c}$ is defined as

$$\hat{h_c} = h_c/L_c \approx h_c/R_c \ll 1. \tag{34}$$

It is also assumed that the classical beam strains ϵ are on the same order as $\hat{h_c}$, and a scaled strain parameter is introduced:

$$\hat{\epsilon} = \hat{h_c}^{-1}\epsilon \sim 1. \tag{35}$$

Warping of the cross-section is solved by finite-element analysis, with homogenization of the spatial variables only, rather than both time and space. This quasi-static formulation solves arbitrary cross-sectional deformations, but neglects inertia of the cross-sectional warping deformations. In order to include inertial terms for more accurate solutions of a dynamic system, finite-section modes may be included. This method was implemented by Palacios and Cesnik in UM/VABS.

2.1.2 Aerodynamic Model

In the NLABS aerodynamic model, airloads are computed using Peters' flexible airfoil aerodynamics [64] and finite-state inflow model [124] in combination with empirical data for profile drag and stall loads. Peters' finite-state model [64] approximates arbitrary camber deflections using Chebyshev polynomials. This model also accounts for variable freestream velocity and induced flow due to the wake as well as other sources. The assumptions of Peters' theory are that of a thin, inviscid airfoil, and that the airfoil is operating in the linear aerodynamic regime. The matrix form of the lift and drag equations are as follows

[64]:

$$\begin{aligned}
\frac{1}{2\pi\rho}\{L_n\} &= -b^2[M]\{\ddot{h}_n + \dot{v}_n\} - bu_0[C]\{\dot{h}_n + v_n - \lambda_0\} - u_0^2[K]\{h_n\} \\
&\quad -b[G]\{\dot{u}_0 h_n + \bar{u}_0\zeta_n - u_0 v_n + u_0\lambda_0\} \\
\frac{1}{2\pi\rho}\{D\} &= -b\{\dot{h}_n + v_n - \lambda_0\}^T[S]\{\dot{h}_n + v_n - \lambda_0\} + \{\ddot{h}_n + \dot{v}_n\}^T[K-H]\{h_n\} \\
&\quad +\{\dot{u}_0 h_n + \bar{u}_0\zeta_n - u_0 v_n + u_0\lambda_0\}^T[H]\{h_n\}, \qquad (36)
\end{aligned}$$

where

$$\begin{aligned}
\{v_n\} &= \begin{bmatrix} v_0 & v_1 & 0 & 0 & \dots \end{bmatrix}^T \\
\{\lambda_0\} &= \begin{bmatrix} \lambda_0 & 0 & 0 & 0 & \dots \end{bmatrix}^T \\
\{\lambda_1\} &= \begin{bmatrix} \lambda_0 & \lambda_1 & 0 & 0 & \dots \end{bmatrix}^T \\
\{1\} &= \begin{bmatrix} 1 & 0 & 0 & 0 & \dots \end{bmatrix}^T, \qquad (37)
\end{aligned}$$

in which v_i terms are the generalized inflow velocities and λ_i terms are the generalized induced velocities. The matrix for the aerodynamic stiffness, $[K]$, is defined as

$$\begin{aligned}
K_{1,n} &= (n-1) \text{ for odd } n \\
K_{2,n} &= (n-1)f \text{ for even } n \\
K_{n,n} &= -(n-1)/2 \\
K_{m,n} &= 0 \text{ for all other } K_{m,n}, \qquad (38)
\end{aligned}$$

matrices for the aerodynamic damping, $[C]$ and $[S]$, are defined as

$$\begin{aligned}
C_{1,1} &= f \\
C_{1,2} &= 1 \\
C_{n,(n-1)} &= -1/2 \\
C_{n,(n+1)} &= 1/2 \\
C_{m,n} &= 0 \text{ for all other } C_{m,n}, \qquad (39)
\end{aligned}$$

and

$$\begin{aligned} S_{1,1} &= f \\ S_{m,n} &= 0 \text{ for all other } S_{m,n}. \end{aligned} \tag{40}$$

The matrix for inertia $[M]$ is defined as

$$\begin{aligned} M_{0,0} &= 1/2 \\ M_{1,1} &= 1/16 \\ M_{0,2} &= M_{2,0} = -1/4 \\ M_{n,n} &= \frac{n}{4(n^2-1)} \text{ for } n \geq 2 \\ M_{n-1,n+1} &= M_{n+1,n-1} = -1/8n \text{ for } n \geq 2 \\ M_{m,n} &= 0 \text{ for all other } M_{m,n}, \end{aligned} \tag{41}$$

and matrices for the inflow, $[G]$ and $[H]$, are defined as

$$\begin{aligned} G_{1,2} &= 1/2 \\ G_{2,3} &= 1/4 \\ G_{n,(n-1)} &= -1/4 \\ G_{n,(n+1)} &= 1/4 \text{ for } n \geq 3 \\ G_{m,n} &= 0 \text{ for all other } G_{m,n} \end{aligned} \tag{42}$$

and

$$\begin{aligned} H_{n,n} &= (n-1)/2 \\ H_{m,n} &= 0 \text{ for all other } H_{m,n}. \end{aligned} \tag{43}$$

Although Peters' theory does not implicitly include compressibility effects, the Prandtl-Glauert correction factor $\frac{1}{1-M_\infty^2}$ is applied to the aerodynamic stiffness matrix $[K]$ [64].

In NLABS the implementation of this model applies a dynamic inflow model based on the Peters and He model [124] for solution of the wake-induced velocity λ_0. This model makes the assumption that w, the velocity normal to the rotor plane, can be expressed as

a function of radial and azimuthal terms:

$$w(r,\psi,t) = \sum_{s=0}^{\infty} \sum_{j=s+1,s+\psi,\ldots}^{\infty} \phi_j^s(r)\big[\alpha_j^s(t)cos(s\psi) + \beta_j^s(t)sin(s\psi)\big], \tag{44}$$

where r and ψ are radius and azimuth, respectively, and ϕ is the set of radial expansion functions. The α and β coefficients are inflow states, which are dependent on circulatory lift, and defined in [124]. The zeroth-order inflow λ_0 is determined as:

$$\lambda_0 = \sum_{s=0}^{\infty} \sum_{j=s+1,s+3,\ldots}^{\infty} J_0\Big(\frac{sb}{r}\Big)\phi_j^s(r)\big[\alpha_j^s(t)cos(s\psi) + \beta_j^s(t)sin(s\psi)\big], \tag{45}$$

where b is the semi-chord and J_0 is the Bessel function of the first kind.

Induced drag is defined in Peters' theory, but the profile drag must also be included to obtain an accurate drag calculation. NLABS corrects the airloads with a quasi-static profile drag term, as well as a dynamic stall term based on the ONERA model [125], taking the approach outlined by Stumpf and Peters [126]. The derivation used in NLABS can be found in Thepvongs et al. [127], and the corrected airloads can be written as:

$$\begin{aligned} L_{0,tot} &= L_{0,fs} - \rho b c_{d0}(u_0^2 + v^T S v)^{\frac{1}{2}} S v + \rho u_0 \Gamma_0 \\ L_{1,tot} &= L_{1,fs} + \rho u_0 \Gamma_1 \\ D_{0,tot} &= D_{0,fs} + \rho b c_{d0}(u_0^2 + v^T S v)^{\frac{1}{2}} u_0, \end{aligned} \tag{46}$$

where c_{d0} is the profile drag, $\Gamma_{s,0}$ and $\Gamma_{s,1}$ are dynamic stall states, and subscripts tot and fs refer to the total airloads and finite-state airloads, respectively. Profile drag and dynamic stall states are determined near stall by XFOIL [128], a panel code with boundary layer and compressibility corrections for two-dimensional airfoils, and in deep stall they are determined by an empirically-derived approximation. The drag and stall states are formulated as functions of Reynolds number, angle of attack, and camber deformation.

2.1.3 CSD/Finite-State Aerodynamics Coupling

The set of aeroelastic equations are defined by the structural, finite-state, wake, and dynamic stall equations previously described. The aerodynamic motion and forces are related with

those of the structural dynamics through the expression derived in Thepvongs et al. [127]:

$$\begin{aligned} A(X)\dot{X} + S(X,\hat{X}) &= L_{fs}(X,\dot{X},\hat{X},\alpha,\beta,\Gamma_s) \\ BC(\hat{X}) &= 0, \end{aligned} \tag{47}$$

where A is the inertia matrix operator, S is the structural matrix operator, X, $\dot{X}$, and $\hat{X}$ are the structural state vector, its time derivative, and its boundary conditions. The aerodynamic loading operator L_{fs} is a function of the structural, inflow, and dynamic stall states. A three-point backwards Euler scheme is carried out for time integration of the first-order equations, and a four-point backwards Euler scheme is used for integration of the second-order dynamic stall equations. This formulation allows for a simultaneous solution of the structural and aerodynamic equations, which is solved via Newton-Raphson iterations.

2.1.4 Trim

In this research rotor simulations are trimmed for steady level flight through adjustment of the collective, lateral cyclic, and longitudinal cyclic controls. The state of current flight conditions is defined as the time-averaged thrust, pitching moment, and roll moment, which are driven to specified trim values. An auto-pilot method described by Peters et al. [129] is applied, in which control settings are updated every time step. The governing equations for these control settings are

$$\begin{aligned} \tau\ddot{\theta} + \dot{\theta} &= J^{-1}\{a(G-g) - b\dot{g} - d\ddot{g}\} \\ J_{kl} &\approx \frac{1}{T}\int_0^T \frac{\partial g_k}{\partial \theta_1} dt, \end{aligned} \tag{48}$$

where $\theta = [\theta_0\ \theta_{1c}\ \theta_{1s}]^T$ is the set of collective, lateral, and longitudinal control settings, T is the period, and G and g are the target and current values of the trim settings, respectively. In the simulations performed in this research the coefficients b, d, and τ are set to 0, and $a = 1/T$. The Jacobian J is numerically approximated by applying a step change in control settings and recording the response after one revolution. This trim method is independent of the structural and aerodynamic equations; therefore, the aerodynamic model can be

interchanged without affecting the trimming process, and for convenience it is used in both the finite-state and CFD-based simulations.

2.2 CFD Model – FUN3D

The CFD solver chosen for this analysis is Fully Unstructured Navier-Stokes Three-Dimensional flow solver (FUN3D) developed by NASA Langley Research Center [130, 131]. FUN3D is a flow solver for unstructured grids, which has been demonstrated by O'Brien [132] and Renaud et al. [133] to give comparable results with structured mesh methods for compressible and incompressible equation sets.

An overset rotor application was developed by O'Brien [132] to facilitate common blade motions for overset meshes, and full rotor articulation was added by Abras [134]. FUN3D has the capability to make calls to the Donor interpolation Receptor Transaction Library (DiRTLib) [135] and the Structured, Unstructured, Generalized overset Grid Assembler (SUGGAR) [136] library developed by Ralph Noack to perform "on-the-fly" hole cutting and generation of domain connectivity information. This feature is essential for the coupling process, as it allows arbitrary deflections to be applied to the CFD grid at every time step. Body motion can be applied through rigid grid rotation, grid deformation, or both. Rigid rotations are applied through a simpled coordinate transformation of all grid nodes. For deforming grids, a boundary surface can be transformed or specified. Cells off the surface of the blade are deformed by applying static elasticity equations to edges of the cell and solving the system iteratively. Biedron and Lee-Rausch [48, 137, 138] loosely coupled FUN3D with CSD solver CAMRAD II with elastic bending and twisting degrees of freedom to include aeroelastic influences in forward flight airload predictions and perform a blade-vortex interaction analysis.

2.2.1 Governing Equations

FUN3D uses a finite-volume scheme to solve the instantaneous Navier-Stokes equations, which are expressed in tensor form as

$$\begin{aligned} \frac{\partial \rho}{\partial t} + \frac{\partial}{\partial x_j}\left(\rho u_j\right) &= 0 \\ \frac{\partial}{\partial t}\left(\rho u_i\right) + \frac{\partial}{\partial x_j}\left(\rho u_j u_i\right) &= -\frac{\partial p}{\partial x_i} + \frac{\partial t_{ji}}{\partial x_j} \\ \frac{\partial}{\partial t}\left[\rho\left(e + \frac{1}{2}u_i u_i\right)\right] + \frac{\partial}{\partial x_j}\left[\rho u_j\left(h + \frac{1}{2}u_i u_i\right)\right] &= \frac{\partial}{\partial x_j}\left(u_i t_{ij}\right) - \frac{\partial q_j}{\partial x_j}, \end{aligned} \tag{49}$$

where e is internal energy and $h = e + p/\rho$ is the specific enthalpy. The formulation for the viscous stress tensor t_{ij} assumes a Newtonian fluid:

$$t_{ij} = 2\mu\left(s_{ij} - \frac{1}{3}s_{kk}\delta_{ij}\right), \tag{50}$$

where μ is molecular viscosity, s_{ij} is the strain-rate tensor equal to $\frac{1}{2}\left(\frac{\partial u_i}{\partial x_j} + \frac{\partial u_j}{\partial x_i}\right)$, and δ_{ij} is the Kronecker delta.

The heat flux vector q_j is

$$q_j = -\kappa\frac{\partial T}{\partial x_j}, \tag{51}$$

where κ is the thermal conductivity and T is the temperature. Constant specific heat coefficients are assumed, allowing the following relation to be made:

$$q_j = -\frac{\mu}{\mathrm{Pr}}\frac{\partial h}{\partial x_j}, \tag{52}$$

where Pr is the Prandtl number.

The static pressure term p is determined through the equation of state for a perfect gas,

$$p = (\gamma - 1)\left(E - \rho\frac{u^2 + v^2 + w^2}{2}\right), \tag{53}$$

and the laminar viscosity μ is determined by Sutherland's law:

$$\mu = \frac{1 + C^*}{T + C^*}T^{3/2}, \tag{54}$$

where $C^* = 198.6/T_\infty$.

CHAPTER III

THREE-DIMENSIONAL COUPLING INTERFACE

The fluid-structure interface of many CFD/CSD rotor coupling methods apply blade deflections via coordinate transformations at the elastic axis. Local deflections and rotations of the airfoil about the three coordinate axes are applied to each node on the blade surface (Fig. 7(a)). Aerodynamic forces and moments are then sampled or integrated on sections along the span of the blade, and the three forces and three moments are communicated to the CSD solver (Fig. 7(b)). This method has been demonstrated to be effective in many computational efforts [45, 46, 48, 49].

For three-dimensionally morphing structures a one-dimensional FSI is not sufficient. Information about the chordwise distribution of pressure is necessary for the CSD solver to solve airfoil deflections. To provide sufficient information for arbitrary camber modes, forces are calculated for each cell on the CFD surface mesh (Fig. 7(d)), and these forces are applied to an interface mesh generated by the CSD solver. The interface mesh consists of a triangulation of the nodes that define blade cross sections at several stations along the span of the blade. These forces are used to solve for spanwise deflections as well as deformations of the airfoil. Coordinates of the CFD surface mesh are then interpolated from the deformed CSD interface mesh and transferred back to the CFD solver (Fig. 7(c)) using an inverse isoparametric scheme [139, 140]. This method allows for arbitrary deformations of the blade, limited only by the resolution of the grids, and the assumption that the rotor radius is large compared to the chord.

3.1 Data Interpolation Across the Coupling Interface

The interpolation scheme employed by NLABS is an inverse isoparametric mapping method [139, 141] implemented by Lee [140]. In this scheme a search is performed to determine the CSD element in which each CFD node is located. A node is considered to be contained by an element if there exists a vector normal to the blade surface that intersects both the

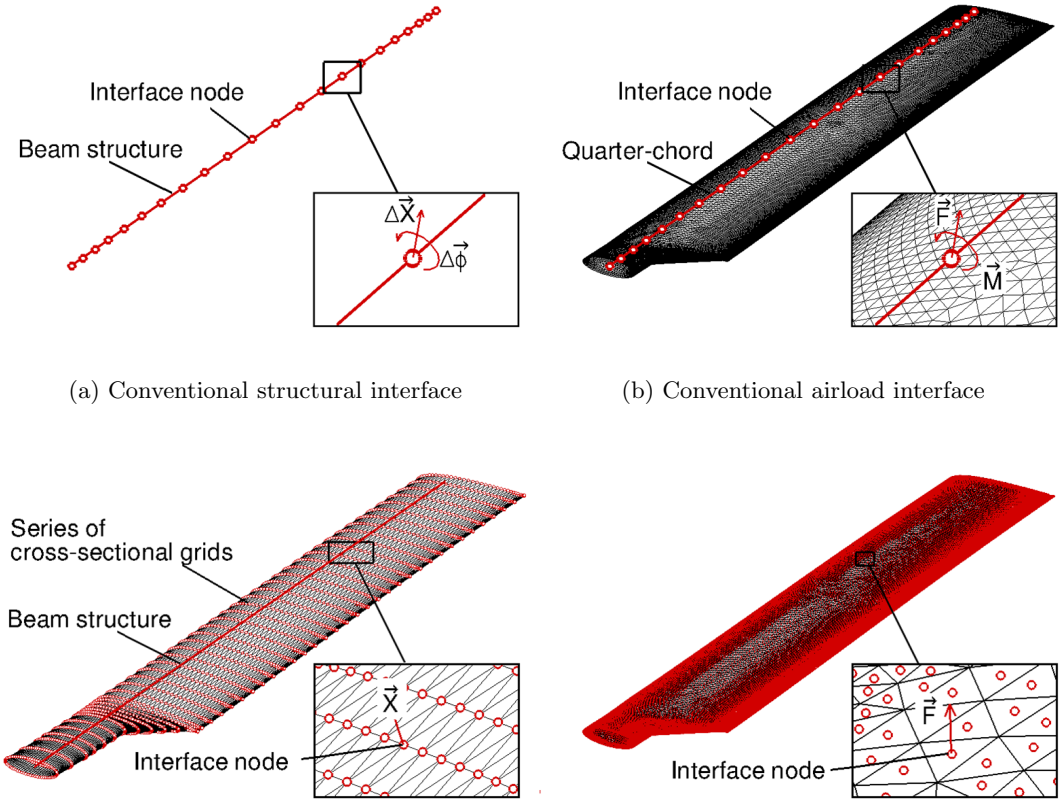

(a) Conventional structural interface

(b) Conventional airload interface

(c) New structural interface

(d) New airload interface

Figure 7: Conventional FSI method and new FSI method.

CFD node and CSD element. If the CFD node is contained by more than one element then the element closest in distance to the node is used for interpolation. The displacement of a CFD node j is defined as [123]

$$u_j^{CFD} = N_j u_i^{CSD}, \tag{55}$$

where N_j is a row matrix of the element shape functions for node j, and u_i^{CSD} is a column matrix of the displacements of the nodes defining CSD element i.

The assumption in Eq. 55 is that the distance from the CFD node to the CSD element is small. However, this distance can become large at places where there is a discontinuity in cross-section geometry. In a test case of the CFD/CSD interface, a "wrinkling" of the blade surface appeared at some locations, as observed just inboard of the trailing edge tab when a 20° rigid pitch rotation is applied (Fig. 8(a), 8(b)). This is a combined effect of the rotation of the grid surface and the separation distance of the CFD node from the CSD element. Equation 55 has been modified with an additional term to include deflections due to rotation of the element. This term improves the smoothness of the surface even when very large deflections are applied:

$$u_j^{CFD} = N_j u_i^{CSD} + C d_j, \tag{56}$$

where d_j is the distance of CFD node j to the corresponding structural element, and C is the rotation matrix that transforms the element normal vector from its undeformed to deformed orientation. When the rotation term Cd_j is included, the smoothness of the airfoil geometry is preserved (Fig. 8(c)). Although the CFD and CSD surface meshes both represent the same geometry, there may be CFD nodes that are not within the any of the CSD elements due to the different surface discretizations. In this case the deflections are extrapolated as:

$$u_j^{CFD} = \sum_{i=1}^{P} \left[\gamma_{ij}(x_i^{CSD} - x_j^{CFD})^2 + r^2\right]^{1/2} \tag{57}$$

where x_i^{CSD} and x_j^{CFD} are the positions of CSD and CFD surface nodes, respectively. P is the number of structural nodes used for the extrapolation, r is the shape parameter [141], and γ_{ij} are the weighting coefficients. Displacements of extrapolated nodes are averaged with surrounding interpolated nodes to improve the smoothness of the surface near

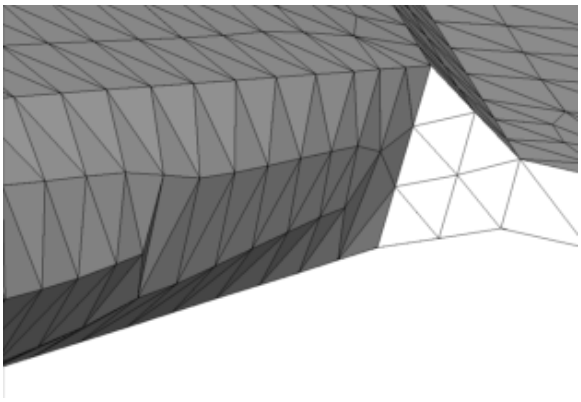

(a) Original mesh

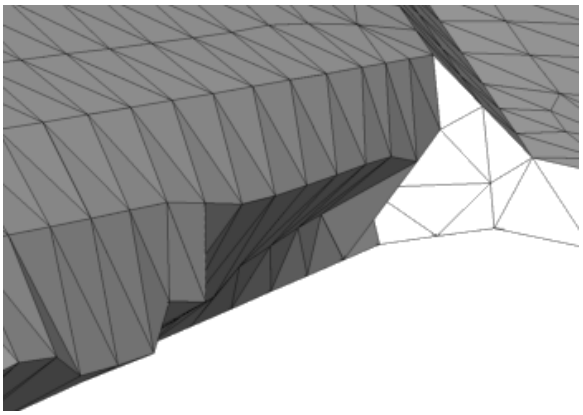

(b) Deformed mesh without rotation term

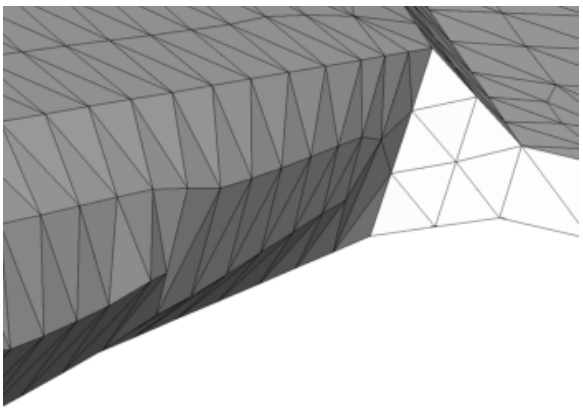

(c) Deformed mesh with rotation term

Figure 8: CFD surface mesh with and without rotational term in the interpolation equation.

extrapolated regions.

Interface routines in NLABS allow external (e.g. aerodynamic) forces to be applied to structural nodes. The transfer of forces from the CFD cell faces to the CSD nodes applies the same finite-element shape functions that were used for blade deformations. Aerodynamic forces are distributed to CSD nodes of element j in the following manner [123]:

$$F_i^{CSD} = N_k F_k^{CFD} \tag{58}$$

where F_i^{CSD} is the portion of the force at CFD face center k distributed to CSD node i, and N_k is the row matrix of shape functions evaluated at the center of CFD cell k. If a cell center is not enclosed by any structural element, then its corresponding force and moment contribution are applied to the nearest structural node.

Unnecessary computational effort can be spent searching for the CSD element used for interpolation if the search is performed over all CSD elements. For computational efficiency, each blade surface is divided into the following surface patches: top, bottom, root and tip. The interpolation and extrapolation routines are performed separately for each of these smaller domains on each blade.

3.2 Modifications to FUN3D

The primary contribution of this research is the formulation, implementation, and testing of a CFD interface methodology for coupling the CFD solver with the CSD solver. Modifications for implementation of the methodology in NLABS were contributed by Thepvongs [123], while the contribution of the author was in implementing the coupling interface in FUN3D. While routines were previously available in FUN3D for coupling with CSD codes CAMRAD II [48] and DYMORE [49], these methodologies did not provide capabilities for a three-dimensional fluid-structure interface. The approach taken in this research updates three-dimensional deformations in the CFD blade surface mesh and communicates a three-dimensional distribution of forces on the blade surface to the structural solver.

The CFD portion of the interface begins by collecting all nodes on the blade surface. These nodes are sorted by blade and surface patch and transferred to NLABS for initialization of the inverse isoparametric mapping. Similarly, the cell face centers on the blade

surface are calculated and sorted. The coordinates of nodes and face centers are communicated to NLABS, which performs the searches for corresponding structural elements used for interpolation. This procedure is performed only on the first iteration; the mapping information is stored and accessed in future iterations. Subsequently, a call is made to the structural solver in the NLABS library each time step to transfer blade loads and to receive updated node coordinates from the CSD solver (Fig. 9).

Forces are computed at the center of each triangular cell face that lies on the surface of the blade. From the pressure coefficients at face vertices, a linear interpolation is performed to define the pressure at the face center. The area and normal vector of the triangular faces are calculated from the cross product of two cell edges:

$$\begin{aligned} A_{cell} &= \frac{|\vec{a} \times \vec{b}|}{2} \\ \vec{n} &= \frac{\vec{a} \times \vec{b}}{2A_{cell}}, \end{aligned} \tag{59}$$

where A_{cell} is the area of the face, $\vec{n}$ is the normal unit vector, and $\vec{a}$ and $\vec{b}$ are vectors from the first to second node and from the first to third node defining the cell face, respectively. The force vector $\vec{F}$ is then calculated for each cell on the blade surface:

$$\vec{F} = c_p q_\infty A_{cell} \vec{n}, \tag{60}$$

where q_∞ is the freestream dynamic pressure. The skin friction is expected to have negligible influence on normal blade loading and is not currently included in these forces, but can be added.

These forces are communicated to NLABS and applied as external loads during the next structural time step. After the structural solution is computed, updated CFD nodes, as well as Euler angles describing blade root orientation and root-to-tip orientation of the blade, are returned to FUN3D. Root-to-tip angles (subscript r-t) include both the rigid and elastic deflections from the root and tip, and are defined as

$$\begin{aligned} \theta_{r-t} &= \frac{1}{2}(\theta_{root} + \theta_{tip}) \\ \beta_{r-t} &= \tan^{-1}\left(\frac{z_{tip} - z_{root}}{x_{tip} - x_{root}}\right) \\ \zeta_{r-t} &= \tan^{-1}\left(\frac{y_{tip} - y_{root}}{x_{tip} - x_{root}}\right), \end{aligned} \tag{61}$$

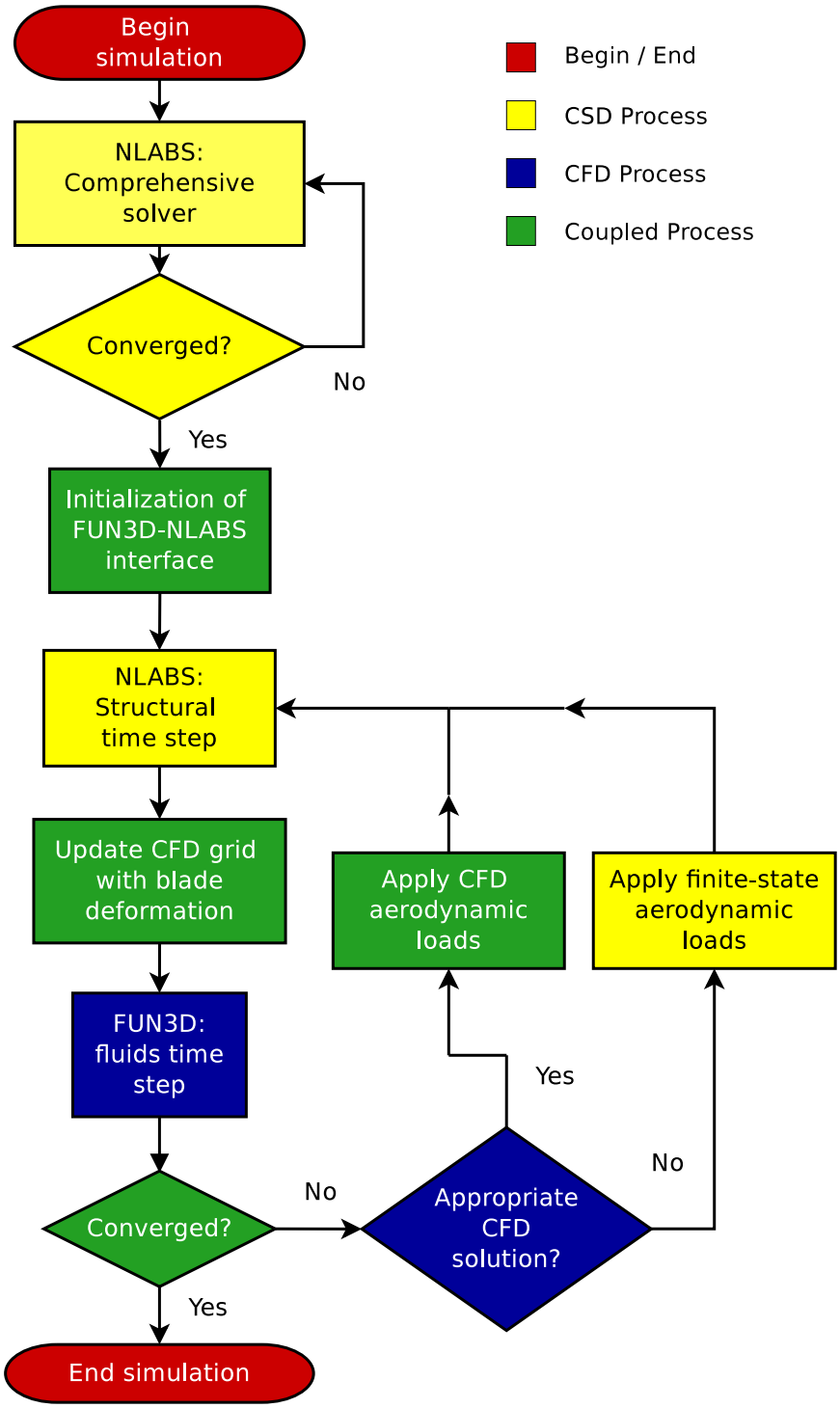

Figure 9: Flowchart of FUN3D/NLABS coupling process.

where θ_{r-t} is the pitch angle, β_{r-t} is flap angle, and ζ_{r-t} is lead/lag angle. An inverse transformation is next applied to the CFD node coordinates using the root-to-tip Euler angles of the blade. These deflections are reapplied later as rigid rotations of the entire blade grid. The purpose of this procedure is to minimize the deformation of grid cells, and thus retain grid quality and prevent deformation of cells to the extent that their volumes become negative. The transformations are defined as

$$C_\theta = \begin{bmatrix} 0 & 0 & 0 \\ 0 & \cos\theta_{r-t} & \sin\theta_{r-t} \\ 0 & -\sin\theta_{r-t} & \cos\theta_{r-t} \end{bmatrix}$$

$$C_\zeta = \begin{bmatrix} \cos\zeta_{r-t} & \sin\zeta_{r-t} & 0 \\ -\sin\zeta_{r-t} & \cos\zeta_{r-t} & 0 \\ 0 & 0 & 0 \end{bmatrix}$$

$$C_\beta = \begin{bmatrix} \cos\beta_{r-t} & 0 & \sin\beta_{r-t} \\ 0 & 0 & 0 \\ -\sin\beta_{r-t} & 0 & \cos\beta_{r-t} \end{bmatrix} \tag{62}$$

and are applied in the following order:

$$X_i^* = C_\theta^{-1} C_\zeta^{-1} C_\beta^{-1} X_i. \tag{63}$$

X_i is a column matrix of the original coordinates of surface mesh node i in the rotating frame, and X_i^* is a column matrix of the deformed mesh coordinates in the blade frame. Nodes on the CFD blade surface mesh are updated with the values of X_i^*. An existing volume grid deformation routine in FUN3D is called to deform the blade volume grid to conform to the new boundary surfaces. The grid deformation routine utilizes a static elastic model that applies strains to cell edges until an equilibrium position is reached. The root-to-tip angles are then applied as a rigid rotation to the volume grid of the blade:

$$X_j^n = C_\beta C_\zeta C_\theta X_j^*, \tag{64}$$

where j is the index of volume grid nodes. A "dci-on-the-fly" feature in FUN3D utilizes the SUGGAR [136] library for hole-cutting and computation of domain connectivity interpolation between the overset grids.

To prevent possible aeroelastic instabilities or large excursions in trim and elastic motion from the converged solution, the trimmed solution from a comprehensive NLABS simulation is used for the initial rigid and elastic motion of the blade. Initially finite-state aerodynamic loads are applied, after which a transition to CFD loads is made, using a weighting term. In the current implementation f is piecewise linearly dependent on time, such that

$$\begin{aligned} f = & \quad 0, & \psi \leq \psi_1 \\ f = & \quad \frac{\psi - \psi_1}{\psi_2 - \psi_1}, & \psi_1 < \psi < \psi_2 \\ f = & \quad 1, & \psi \geq = \psi_2, \end{aligned} \tag{65}$$

where ψ is the current azimuth and ψ_1 and ψ_2 are user-defined. This method is intended to avoid large blade deflections that might result from the initial CFD solution, and aid in the convergence of the flow solution and trim solution.

3.2.1 Conservation of Work

The aerodynamic and structural components should ideally form a closed system, as discussed by Smith [142]. Since the method of extrapolating and integrating forces does not automatically enforce conservation of work in the present method, work is compared on the CFD and CSD surface meshes to determine the magnitude of error in work across the interface.

Comparison of the integrated work on each side of the interface over one time step can provide insight into the magnitude of error introduced by data interpolation. Aerodynamic work is calculated and integrated over the entire blade surface, for a single time step [142]:

$$W^n_{AERO} = \sum_{i=1}^{N} (\mathbf{F}^n_i \cdot \mathbf{r}^n_{d,i}), \tag{66}$$

where n is the time step index, i is the face index, $\mathbf{F}$ is the force vector, and $\mathbf{r}$ is the displacement vector in the rotating frame over one time step. When quarter-chord forces are communicated across the interface the contributions of work from moments are also included. Work was integrated over each cell, over the entire blade surface; thus moment contributions were included implicitly. Work was integrated separately over the set of CFD

nodes and the set of CSD grid nodes. Work is conserved across the interface if

$$W^n_{CFD} = W^n_{CSD}. \tag{67}$$

Otherwise the error is defined as the difference between the spatially-integrated work on the CFD and CSD grids:

$$\epsilon = W^n_{CFD} - W^n_{CSD}. \tag{68}$$

Two test cases were explored to determine the magnitude of error in work. In the first case work was evaluated on CFD and CSD surface meshes in compliant-airfoil simulations at $M_\infty = 0.64$. Camber stiffness was varied in two different cases, such that $\omega_\delta/\omega_\alpha = 12.1$ and $\omega_\delta/\omega_\alpha = 60.5$, where ω_δ is the natural frequency of the camber mode, and ω_α is the natural frequency of the pitch mode. Pitch and plunge values were set such that the natural frequencies were equivalent to the first natural frequencies of the HART [119] rotor at 109 rad/s. In the lower-stiffness case, even when large high-frequency camber oscillations were present, the normalized error, $\epsilon^n = (W^n_{CFD} - W^n_{CSD})/(W^n_{CSD,max} - W^n_{CSD,min})$, remained under 1.5% at all time steps. In the higher-stiffness case the normalized error was less than 0.5% throughout the simulation. The error is largest during the periods when high-frequency oscillations (Fig. 10) were generated due to the high-frequency excitation of the camber mode.

Error in conservation of work was also evaluated in a three-dimensional rotor configuration. In the baseline case the normalized error is within 0.08%, and in a zero-phase, 0.5%c magnitude camber (C0) actuation case, it is less than 0.05% (Fig. 11). During several revolutions error in aerodynamic work may become cumulatively large. To ensure that the cumulative error was small and bounded the work was integrated in both time and space [142]:

$$W_{AERO} = \sum_{n=1}^{N_n} W^n_{AERO} = \sum_{n=1}^{N_n} \sum_{i=1}^{N} \mathbf{F}^n_i \cdot \mathbf{r}^n_{d,i}, \tag{69}$$

where N is the number of surface points and N_n is the number of time steps. In each blade section case work was integrated over a time interval beginning and ending at peaks of pitch oscillations. The integrated work in each case is very small: 0.21% in the $\omega_\delta/\omega_\alpha = 12.1$ case and 0.57% in the $\omega_\delta/\omega_\alpha = 60.3$ case. In the baseline case aerodynamic there is

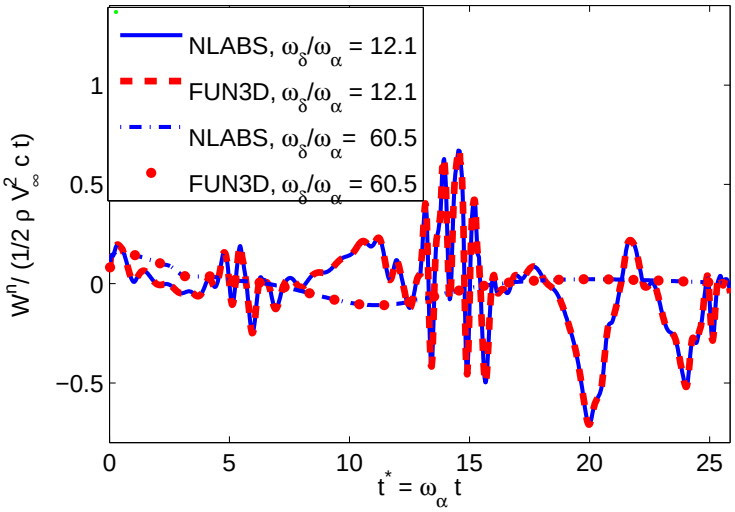

(a) Rate of work vs. time

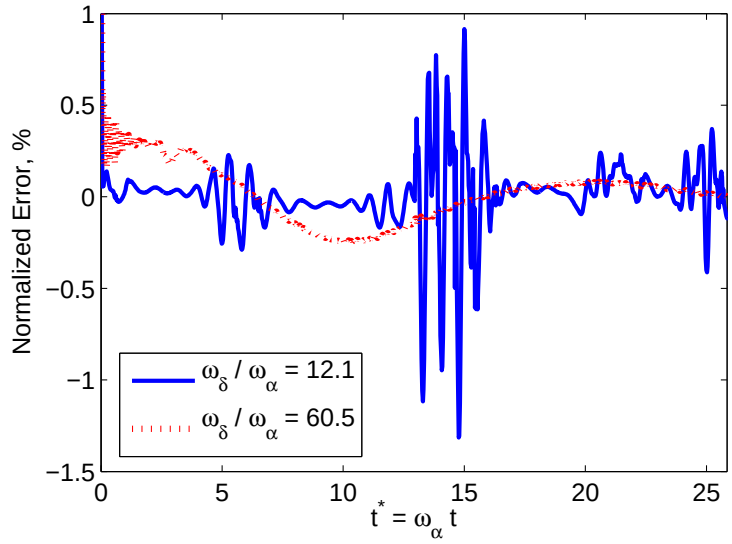

(b) Relative error across the interface

Figure 10: Comparison of work calculated on each side of fluid-structural interface

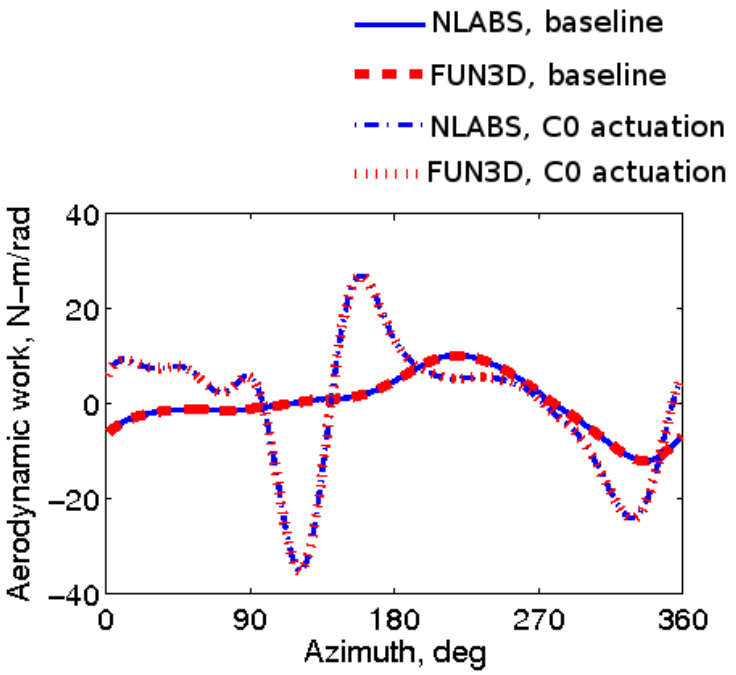

(a) Work per radian vs. azimuth

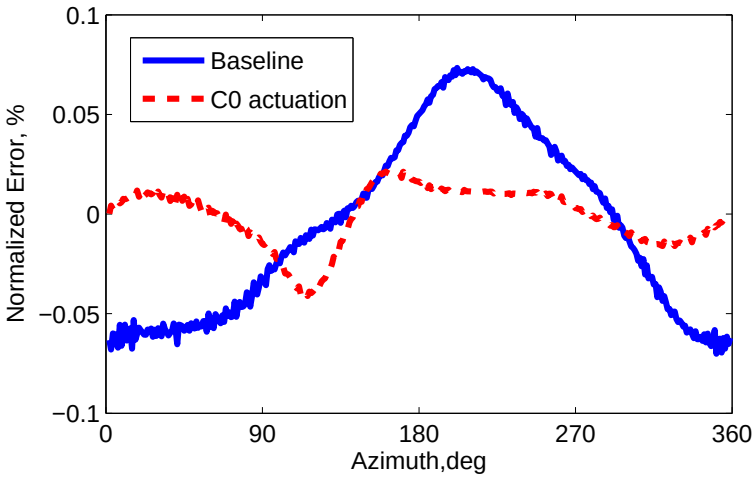

(b) Relative error across the interface

Figure 11: Comparison of work calculated on each side of fluid-structural interface for baseline and 0-phase camber actuation case

a 0.010 N-m/rev difference in the work integrated on the CSD grid (Table 1), while in the camber actuation case there is a 0.004 N-m/rev difference. The error is normalized by the integrated aerodynamic work done by the active rotor in one revolution, $E^* = (W_{CFD} - W_{CSD})/W_{CSD,C0}$, which results in an error of 1.02% and 0.42% for the baseline and actuated cases, respectively. Thus, it is concluded that the relative error is small for both the instantaneous and time-integrated work.

Table 1: Integrated aeroelastic work (N-m) over one rotor revolution.

	Baseline	Camber actuation ($0°$phase, $0.25\%c$)
Maximum rate of work, N·m/rad	10.2	26.9
Minimum rate of work, N·m/rad	-12.0	-35.2
NLABS time-integrated work, N·m/rev	0.036	0.953
FUN3D time-integrated work, N·m/rev	0.046	0.957
Error in integrated work, N·m/rev	0.010	0.004

CHAPTER IV

VERIFICATION OF THE METHODOLOGY

Experimental data for full rotor configurations with variable-camber blades are not yet available; therefore, verification of the methodology has been performed for one-dimensional beam deflections and for two-dimensional cross sectional deflections. Together, these configurations map the three-dimensional effects.

4.1 One-Dimensional Beam Model

A one-dimensional beam model is verified with experimental results for performance characteristics of a rotor in hover and in forward flight. The experimental data are obtained from two sources: 1) the Higher Harmonic Control Aeroacoustic Rotor Test (HART) test [119] performed in the large low-speed wind tunnel Deutsches Zentrum für Luft- und Raumfahrt (DLR), or German Aerospace Center, in 1995; and 2) the Hover Tip Vortex Structure (HOTIS) [120, 143] test performed in the rotor preparation hall of the DLR Institute of Flight Systems in Braunschweig, Germany in 2006. In these experiments the thrust, figure of merit, blade loading, and flow properties of a 40% scaled model of the four-bladed BO-105 rotor were evaluated.

Performance results for a rotor in forward flight and in hover were obtained from the HART II [144] and HOTIS experiments [120, 143], respectively. In the HOTIS experiment the rotor was nearly centered in a $6R \times 6R \times 4R$ (width $\times$ length $\times$ height) room, and the rotor plane was $1.43R$ above the ground. Forward flight results were taken from the HART II experiment [144], in which the rotor was placed $5R$ above the ground in the large wind tunnel at the DLR. In both experiments the rotor was constructed with a NACA 23012 airfoil and had a radius 2m, chord length 0.121m, solidity 0.077, and a linear twist $-8°$ per radius length. In the HOTIS test there was a pre-cone angle of 2.5°. Structural dimensions and properties are available from the HART II experiment and are listed in Table 2.

Table 2: HART/HOTIS Rotor Properties

Geometry	
Radius, m	2.00
Root cutout, m	0.44
Chord, m	0.121
Geometric twist, deg/m	-4.0
Solidity	0.077
Stiffness properties	
Elastic axis, chords	0.275
EA, N·m	1.17×10^7
GJ, N·m^2	160
EI_2, N·m^2	250
EI_3, N·m^2	5200
Mass and inertia properties	
m, kg/m	0.95
$m_{\theta 1}$, kg·m	7.47×10^{-4}
$m_{\theta 2}$, kg·m	1.70×10^{-5}
$m_{\theta 3}$, kg·m	7.30×10^{-4}

4.1.1 CSD Grid

As described in Section 2.1, the CSD model consists of a nonlinear one-dimensional beam model along the span of the blade and a two-dimensional model of the airfoil section at each radial station. At the fluid-structure interface, 80 nodes define the airfoil cross section of the blade at each of 44 radial stations. These nodes are connected to form a structured mesh which serves as an interface surface for communication of forces and displacements between the CFD and CSD solvers. Inverse isoparametric mapping (IIM) is performed to interpolate data from the CFD grid to the CSD grid and vice-versa.

4.1.2 CFD Grid Independence

A HART II blade grid was obtained from NASA. The grid extends two chord lengths in all directions from the blade, except at the blade root where it extends only one chord length inboard. There are 20,400 nodes on the blade surface and a total of 0.896 million total nodes in the blade grid, and the grid spacing at the outer boundaries of the coarse blade grid is $0.17c$. After initial simulations it was verified that the initial spacing normal to the blade surface provides a $y+ < 1$.

Grid quality was verified by Biedron and Lee-Rausch [48] in an analysis of vertical vibratory loads. In the present research rotor performance was a key metric, and accuracy was also required for in-plane loading. Therefore additional analysis was performed to verify the required resolution for computing shaft torque.

4.1.2.1 Grid Analysis of a Blade Section

To determine the chordwise spacing necessary for accurate drag predictions, a grid study was performed, comparing simulation results for blade sections to experimental data for the NACA 23012 airfoil [145].

The circumferential grid spacing was refined as outlined in Table 3. Static simulations were performed at $M_\infty = 0.5$, $Re = 1.7$ million, and 0° angle of attack, and results were compared to experimental data for the NACA 23012 airfoil obtained by Jacobs and Clay [145]. The airfoil model in the experiment has a sharp trailing edge, while the HART rotor has a 4.5%c, 0° tab with a blunt trailing edge. An airfoil grid with a sharp trailing edge was generated to compare lift and drag with experimental data. Another grid with the trailing edge tab was also generated to verify that grid independence was reached near the trailing edge. Through computational analysis it was determined that 0° the trailing edge tab increases lift by 8% and increases drag coefficient by 5% compared to the sharp trailing edge. Computational lift and drag coefficients were corrected for this difference. The Prandtl-Glauert correction factor $\sqrt{\frac{1}{1-M_\infty^2}}$ can be applied to the experimental lift data, which was measured at incompressible freestream Mach numbers.

The characteristic spacing of the coarse grid in Table 3 is the same as the spacing of the initial HART II blade grid. A fine grid ("Fine a") with reduced leading edge and trailing edge spacing was generated, as well as grids with further reduction of the leading edge spacing ("Fine b") and trailing edge spacing ("Fine c").

The coarse grid over predicts drag by 124%. While grid refinement altered lift predictions by less than 2%, drag predictions decreased up to 41% through grid refinement. Though grid refinement greatly improves drag predictions, it still over predicts the experimental value by 32-38%. This is expected to some extent, since the boundary layer is assumed to

Table 3: Influence of grid spacing on lift and drag

	Experiment	Coarse	Fine a	Fine b	Fine c
Chordwise l. e. spacing	–	0.826%c	0.165%c	0.083%c	0.165%c
Chordwise t. e. spacing	–	0.826%c	0.083%c	0.083%c	0.042%c
Lift coefficient	0.115 ± 0.01	0.131	0.129	0.130	0.129
Drag coefficient	0.0082 ± 0.0005	0.0184	0.0113	0.0108	0.0113

be fully turbulent, and this is reflected in the viscous drag, which constitutes 62% of the total profile drag. The wing section in the experiment was covered with a smooth sheet of aluminum, and Jacobs and Clay [145] state that some effects of turbulent transition were observed, causing increases in lift and drag. Because there was little change in lift and drag predictions through further refinement of the leading edge or trailing edge, the characteristic spacing of the "Fine a" grid was used in generating refined three-dimensional HART II blade grids with tetrahedral elements. Finer leading edge spacing was used near the blade tip, since the area near the tip has a large influence on torque predictions because of the high dynamic pressure and large moment arm associated with this region.

4.1.2.2 Grid Analysis of a Static Blade

A static simulation of the three-dimensional finite rotor blade with $M_\infty = 0.5$ was first performed to confirm that the changes in lift and drag for the refined blade grid were similar to those observed in the blade section simulations. An intermediate blade grid was also generated to verify that grid convergence was reached. Details are of the grids are outlined in Table 4 and can be observed in Figures 12 and 13.

In the static blade simulation, the fine grid increased the lift prediction by 2% and decreases the drag prediction 28%. The influence of grid resolution on drag prediction is qualitatively observed upon examination of the pressure distribution (Fig. 14) on a cross-section of the blade. At the leading edge the refined grid more accurately resolved the pressure distribution, improving the drag prediction. Overall, the pressure was reduced in the region near the stagnation point. Pressure distribution was also more accurately resolved across the trailing edge due to the additional points across this surface. This resulted in a pressure recovery across the trailing edge and therefore a decrease in drag

Table 4: Blade discretization summary (per blade).

Structural model			
Structural interface nodes			3680
Structural 1-D elements			43
CFD blade grid	Coarse	Medium	Fine
Total number of nodes	896,241	2,298,435	3,479,399
Number of surface nodes	20,398	53,211	77,106
Circumferential leading edge spacing	0.826%c	0.248%c	0.165%c
Circumferential trailing edge spacing	0.826%c	0.124%c	0.083%c
CFD background grid		Coarse	Fine
Total number of nodes		1,046,807	4,219,631
Grid spacing near rotor plane		25%c	10%c

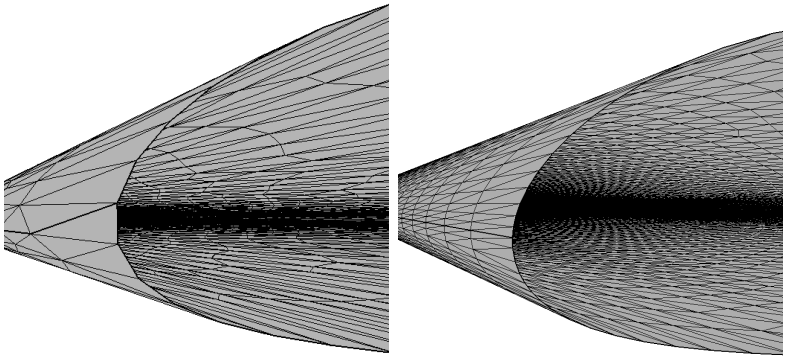

(a) Coarse (b) Fine

Figure 12: Leading edge of coarse and fine HART blade grids.

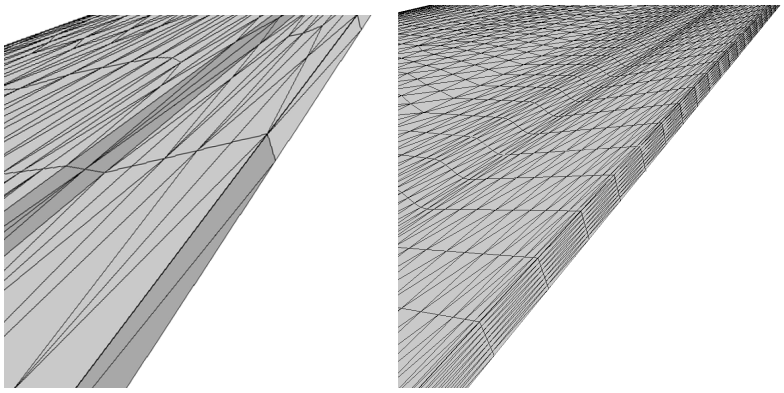

(a) Coarse (b) Fine

Figure 13: Trailing edge of coarse and fine HART blade grids.

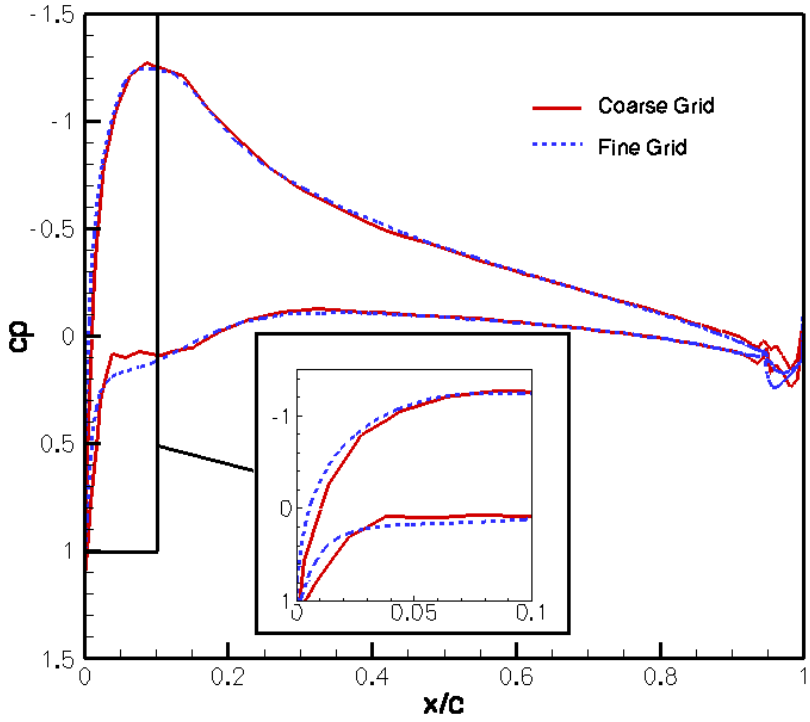

Figure 14: Pressure distribution comparison of medium and fine grid.

prediction. There was little effect on the lift, since pressure was primarily affected at the leading edge and trailing edge.

4.1.2.3 Rotor in Hover

Finally, hover simulations were performed with the rotating four-bladed rotor configuration. The coarse, medium, and fine grids described in Table 4 were applied in a steady simulation of a rotor hovering in free air. The tip Mach number was 0.633 with collective pitch of 8°, which is near the maximum collective angle in the HOTIS experiments at the same Mach number. In these CFD simulations airfoil deformations were prevented by setting a very high cross-sectional stiffness. The pressure coefficient of the medium and fine grids were nearly identical at 75%R, 85%R, and 95%R.

For further confirmation of grid convergence, the rotor performance characteristics were compared among the three grids. The thrust coefficient of the medium and coarse grids

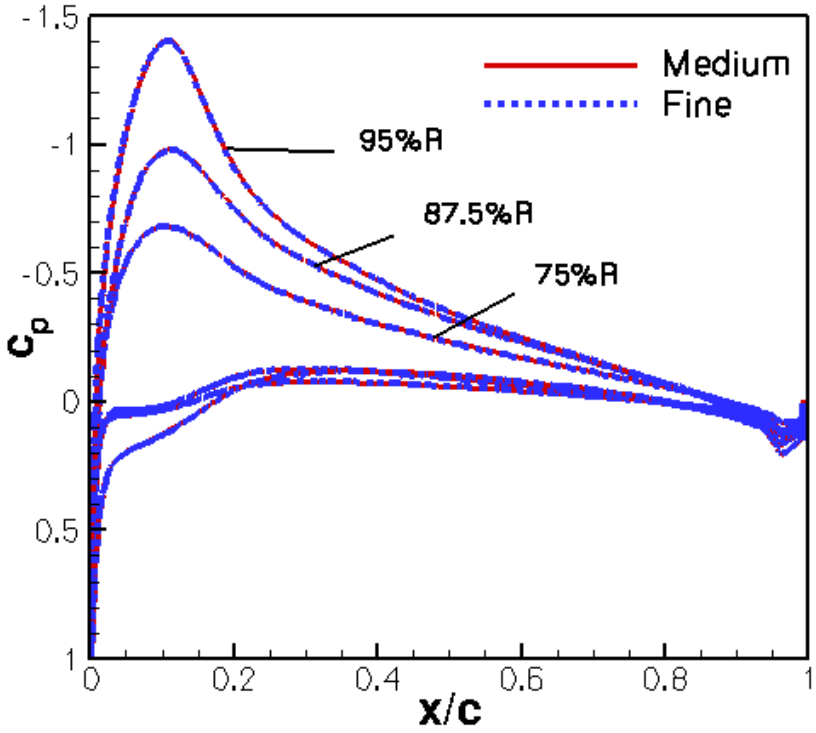

Figure 15: Pressure distribution comparison of coarse and fine grid.

varied from that of the fine grid by only 2-2.4% (Fig. 16). However, the coarse grid resulted in a figure of merit (FM) prediction 14% lower than that of the fine grid, while the FM predicted on the medium grid differed from the fine grid results by only 1.7% (Fig. 16(b)). Therefore, the medium grid was used in subsequent simulations.

4.1.3 Validation of Rotor Performance in Hover

A rotor simulation with the medium grid in free air verified the behavior of the experimental model. There was a 7% difference in thrust coefficient measured in the HOTIS and HART II experiments, and there are at least three possible causes for the discrepancy. First, there were slight differences in rotor configurations such as the geometry of the HART versus HOTIS test rig. The fuselage in the HART experiment was larger in size than the test rig used in the HOTIS experiment, and this can affect blade loading. Second, in the HOTIS experiment, recirculation and test components had some effect on the rotor performance [120, 143]; these issues are addressed in subsequent chapters. The HART II experiment [119, 144] was conducted in a large wind tunnel with anechoic walls, and therefore recirculation was assumed to be very small. Finally, the rotor is in ground effect in the HOTIS experiment ($1.43R$ above ground), while in the HART II experiment it is over $5R$ above the ground.

Thrust was over predicted by 17% in FUN3D simulations when the rotor blades were assumed to be rigid. In FUN3D/NLABS simulations a reduction in thrust was observed due to elastic twist of the blade, caused by the nose-down pitching moment of the airfoil at quarter-chord. The thrust coefficient prediction was greatly improved after aeroelastic effects were applied, with a thrust 4.7% lower than a curve fit of the HOTIS data, and 2.1% higher than the C_T measured in the HART experiment (Fig. 17).

A curve fit was applied to the HOTIS data with the equation FM $\approx -4.503\times10^{-4}C_T^{-1.89}+$ 0.6862. The rigid and elastic rotor simulations under predict the experimental fit by 6.7% and 4.3%, respectively, indicating that aeroelastic effects were primarily important in determining thrust in this case, with small improvements of less than 1% in figure of merit prediction.

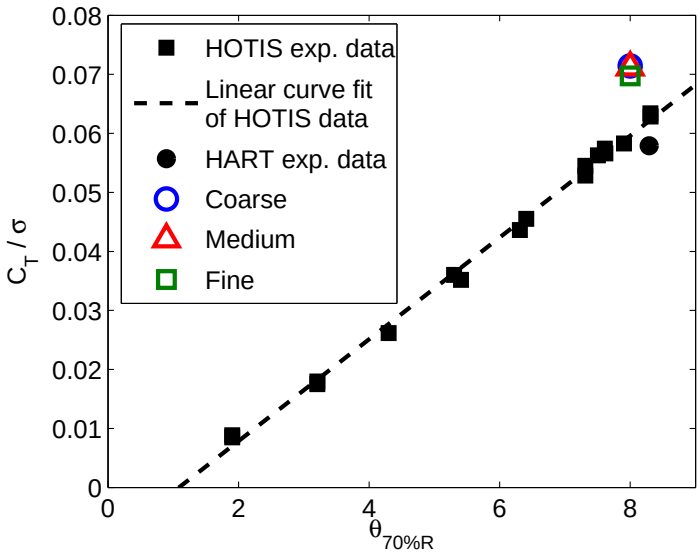

(a) Thrust vs. collective pitch

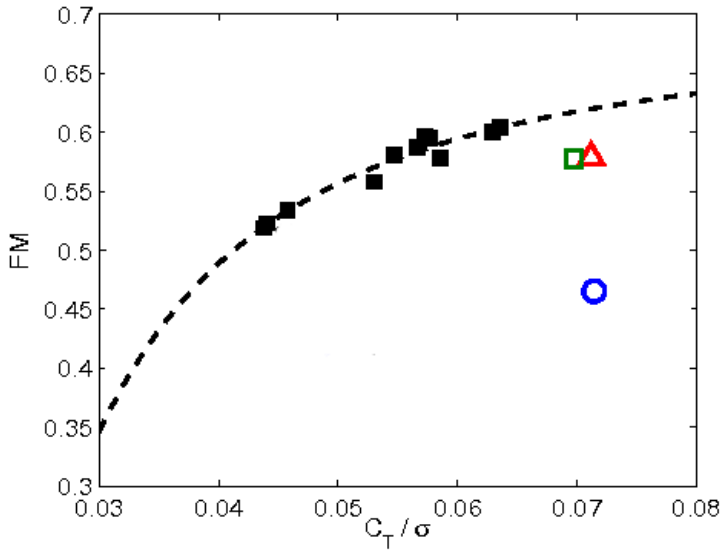

(b) Figure of merit vs. thrust

Figure 16: Performance characteristics for various grid resolutions for the rigid HOTIS rotor in hover.

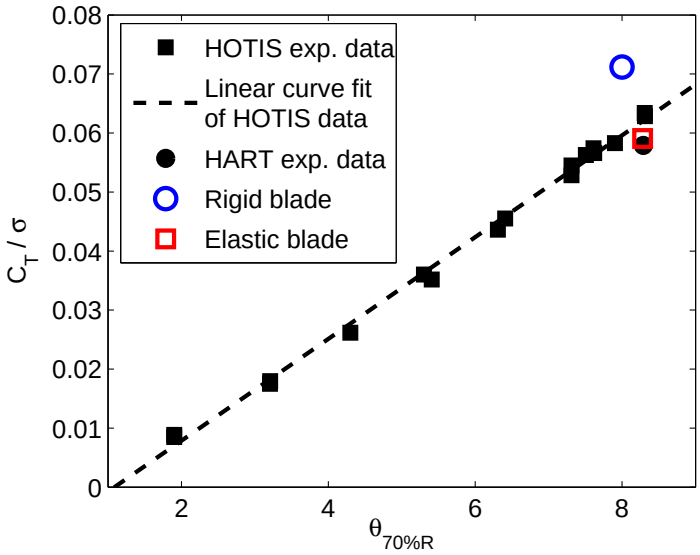

(a) Thrust vs. collective pitch

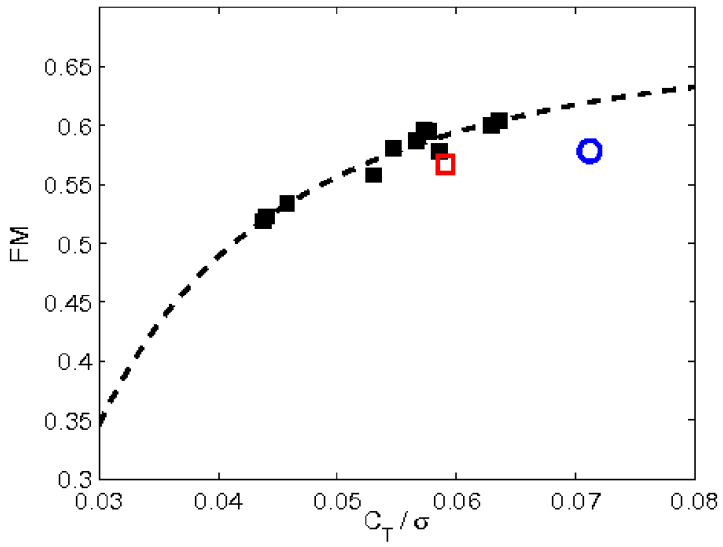

(b) Figure of merit vs. thrust

Figure 17: Performance characteristics for various grid resolutions for a HART II rotor with rigid versus elastic blades

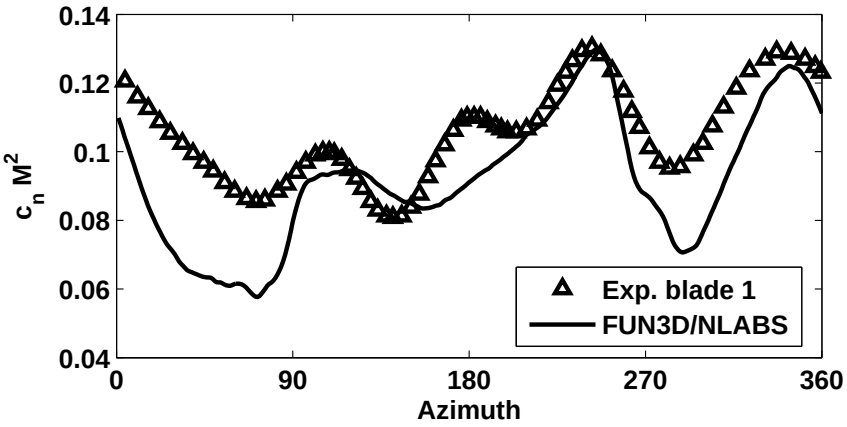

Figure 18: Normal force of HART II rotor at $\mu = 0.15$

4.1.4 Validation of Rotor Airloads in Forward Flight

The FUN3D/NLABS coupling methodology was next applied in forward flight, following the specifications in the HART II documentation [119]. Experimental data are not available at the same flight conditions as the HART II baseline case, in which $\mu = 0.25$ and $\alpha_s = -5.0$, the flight conditions are similar. However, experimental data at similar flight conditions was examined. The rotor was simulated at an advance ratio of 0.15 with a shaft angle of $-3.7°$. Thrust was trimmed to 3300 N, and both the lateral and longitudinal hub moments were trimmed to 0 N-m. The unsteady sectional normal force coefficient and the vertical tip deflection predicted by FUN3D were compared with experimental measurements [144].

4.1.4.1 Sectional Aerodynamic Loads

The FUN3D/NLABS analysis accurately predicts the azimuthal location of most of the normal force coefficient peaks (Fig. 4.1.4.1). The phase error of predicted peak normal forces at 71°, 109°, 243°, and 282° azimuth is 1°–8°, and magnitude error of most of the peaks is within 1–7% of the experimental value. However, at 141° azimuth the predicted normal force peak lags the experimental data by 16°, and the peak at 183° azimuth is not captured. At 71° and 282° azimuth the normal force is under predicted by 26–33%.

When the mean is removed, then normal force peaks vary from experimental data by 10–24%. These results are comparable to results presented by van der Wall et al. [146], in which loads and deflections from comprehensive analyses performed at German Aerospace

Center, US Army AFDD and NASA Langley, Konkuk University of South Korea, ONERA, University of Maryland, and Georgia Institute of Technology. Comprehensive analyses by van der Wall et al. were performed for the HART II rotor at $\mu = 0.15$, with a nose-up shaft angle of 5.3°. In the baseline case normal forces (with mean removed) at 155° azimuth differed by 13–30% from exerimental measurements, and the peak normal forces at 253° differed by 1–18%. In CFD/CSD simulations performed by Smith et al. [147] at the same institutions, peak normal force predictions at 155° were improved significantly, with errors of less than 0.3–6%, except for a hybrid CFD/free wake simulation, in which the error was 30%. At 253° results were varied, with errors of 1–21%. While the normal force in under predicted in the present case in some regions, errors in normal force are comparable to most CFD/CSD and comprehensive results.

4.1.4.2 Vertical Tip Deflection

The vertical tip deflections are compared to verify the structural deflections are accurately modeled (Fig. 4.1.4.2). Peak-to-peak vertical deflections are under predicted by the computational simulation by 43%. The phase of the experimental measurements predicted by FUN3D/NLABS simulations agreed with experimental measurements within the margin of experimental error. Part of the error in deflection magnitude may be due to the uncertainty in the HART II [146] experimental hub moment, in which the margin of accuracy was $\pm 15 - 20$ N-m. In the results presented by van der Wall et al. [146] similar under predictions (23–50%) in peak-to-peak vertical tip deflections were observed in all six comprehensive analyses, relative to the averaged peak-to-peak deflections of the four rotor blades. CFD/CSD analyses by Smith et al. [147] elastic flap predictions were comparable to comprehensive results, under predicting peak-to-peak flap predictions by 23–63% in all cases except in the analysis performed using the hybrid CFD/free wake code GENCAS, in which elastic deflections were over predicted by 3%. In all cases except when GENCAS is applied, vertical tip deflections are greatly under predicted. Predictions for vertical tip deflections in the present case are typical of several other published CFD/CSD solutions.

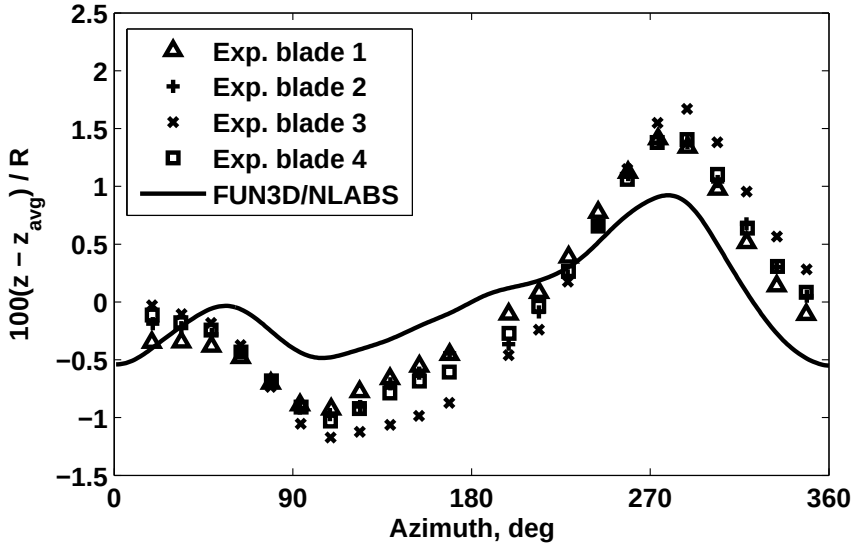

Figure 19: Tip deflections of HART II rotor at $\mu = 0.15$

4.2 Two-Dimensional Cross Section Model

The primary advancement in CFD/CSD coupling capabilities contributed by this work is the ability to analyze the influence of cross-sectional blade deformations. To verify that aeroelastic cross-sectional deformations are modeled correctly, computational results were compared to those of analytical models developed by Theodorsen [148] and Murua et al. [63].

Modifications to the NLABS code were necessary to simulate the aeroelastic behavior of the two-dimensional cross section. New translational and torsional boundary conditions (Fig. 20) have been added to model the pitch and plunge degrees of freedom:

$$M_{bc} = -k_\alpha \alpha \tag{70}$$

$$F_{bc} = k_\zeta \zeta \tag{71}$$

Beam deflections were eliminated by increasing the bending and torsional stiffnesses to 10^{20} N-m^2, which eliminated deflections to less than $10^{-6}c$, so that the beam could be assumed to be rigid.

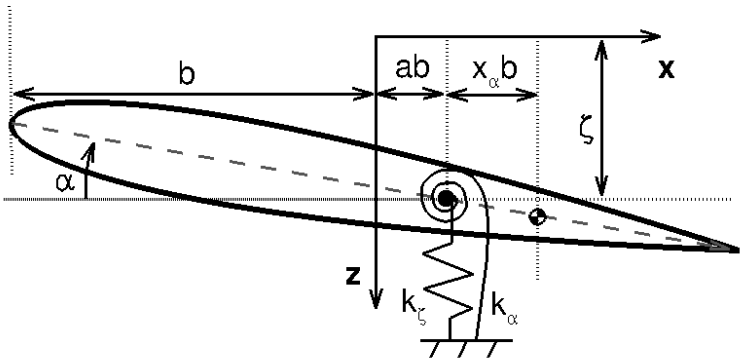

Figure 20: Diagram for airfoil with pitch and plunge degrees of freedom.

4.2.1 Theodorsen's Model for Pitch and Plunge Modes

A classical flutter solution for slender wings with rigid airfoil sections was developed by Theodorsen [148] in 1935. He derived a formula for frequency-based response of the pitch and plunge modes of an airfoil in uniform freestream. Theodorsen's method incorporates a lift-deficiency function,

$$C(k) = F(k) + iG(k) = \frac{H_1^{(2)}(k)}{H_1^{(2)}(k) i H_0^{(2)}(k)}, \tag{72}$$

where k is the reduced frequency ω/bV_∞, and $H_0^{(2)}(k)$ and $H_1^{(2)}(k)$ are Hankel functions of the zeroth and first kinds, respectively. The real value of this function is near 1 at low frequencies, indicating a similar lift response to that of a steady airfoil; and it approaches 0.5 as the frequency increases to infinity, indicating a 50% decrease in lift response, due to induced downwash of the shed wake.

The vertical displacement (positive down) of the airfoil for small deflections is approximated as:

$$h(x,t) = \zeta(t) + (x - ab)\alpha(t), \tag{73}$$

where ζ and α are the plunge and pitch deflections, respectively. The generalized forces L_n are defined as

$$L_n = -b \int_{-1}^{1} T_n(\xi) \Delta p d\xi, \tag{74}$$

where $T_n(\xi)$ are the Chebyshev polynomials, Δp is the pressure difference across the airfoil, and ξ is the nondimensional distance from the midchord, x/b. The equation for lift $(-L_0)$

is formulated to include the lift deficiency function:

$$\frac{L_0}{\pi\rho b} = -b\big(\ddot{\zeta} - ab\ddot{\alpha} + V_\infty\dot{\alpha}\big) - 2V_\infty C(k)\alpha_{qs}, \tag{75}$$

where the left three terms are apparent mass terms, caused by acceleration of the fluid, and the quasi-steady angle of attack α_{qs} is defined as

$$\alpha_{qs} = \dot{\zeta} + \Big(\frac{1}{2} - a\Big)b\dot{\alpha} + V_\infty\alpha. \tag{76}$$

The generalized aerodynamic force L_1 is the pitching moment of the airfoil at midchord, and is equal to

$$\frac{L_1}{\pi\rho b} = -\frac{b^2}{8}\ddot{\alpha} - \frac{V_\infty b}{2}\dot{\alpha} + V_\infty C(k)\alpha_{qs}. \tag{77}$$

The generalized aerodynamic forces, along with the generalized structural forces and inertia, can be applied in the equations of motion to analytically determine flutter speed of an airfoil or wing.

4.2.2 Analytical Flutter Model for Parabolic Camber

Peters [64] extended flexible thin airfoil theory for small arbitrary airfoil deformations with variable freestream velocity. Peters' thin airfoil theory has been applied by Murua et al. [63] to derive flutter and divergence properties of a thin airfoil with three degrees of freedom: pitch, plunge, and parabolic camber.

When the parabolic camber mode is included, the vertical displacement of the airfoil for small deflections is approximated as

$$h(x,t) = \zeta(t) + (x - ab)\alpha(t) + \Psi(x)\delta(t), \tag{78}$$

where δ is the generalized camber deflection, and Ψ is the assumed camber shape. In this case the camber shape is assumed to be parabolic, with a constant vertical offset to impose orthogonality of the mode shapes:

$$\Psi(x) = \Big(\frac{x}{b}\Big)^2 - \frac{1}{3}, \tag{79}$$

where b is the airfoil semichord. The equations of motion per Murua et al. [63] are then

$$\begin{aligned}
\frac{\ddot{\zeta}}{b} + x_\alpha \ddot{\alpha} + \omega_\zeta^2 \frac{\zeta}{b} + \Psi(ab)\omega_\delta^2 \frac{\delta}{b} &= \frac{\kappa}{\pi}\Big(\frac{V_\infty}{b}\Big)^2 c_l \\
x_\alpha \frac{\ddot{\zeta}}{b} + r_\alpha^2 \ddot{\alpha} + (r_\alpha \omega_\alpha)^2 \alpha &= 2\frac{\kappa}{\pi}\Big(\frac{V_\infty}{b}\Big)^2 c_{m,ab} \\
r_\delta^2 \frac{\ddot{\delta}}{b} + \Psi(ab)\omega_\zeta^2 \frac{\zeta}{b} + ([r_\delta \omega_\delta]^2 + [\Psi(ab)\omega_\zeta]^2)\frac{\delta}{b} &= \frac{\kappa}{\pi}\Big(\frac{V_\infty}{b}\Big)^2 c_\Lambda,
\end{aligned} \tag{80}$$

where x_α is the distance of the center of mass aft the elastic axis in airfoil semichords, a is the location of the elastic axis relative to the midchord, κ is the inverse mass ratio, ω is the natural frequency of the mode indicated by its subscript, r_α is the radius of gyration, and r_δ is the nondimensional moment of inertia of the camber mode, defined as $r_\delta = \sqrt{I_\delta/m}$. For a flat plate with uniformly distributed mass, these quantities are $r_\delta^2 = 4/45$, $r_\alpha^2 = 1/3 + a^2$, and $x_\alpha = -a$. The generalized camber force Λ is given by Murua et al. [63] as a function of distributed pressure $p(x)$ and the camber shape $\Psi(x)$:

$$\Lambda = \int_{-b}^{b} \Delta p(x)\Psi(x)dx. \tag{81}$$

If harmonic oscillations are assumed then the generalized forces [149] are

$$\begin{aligned}
\frac{L_0}{\pi\rho b} &= -b\Big(\ddot{\zeta} - ab\ddot{\alpha} - \frac{1}{12}\ddot{\delta} + V_\infty \dot{\alpha}\Big) - 2V_\infty C(k)(\alpha_{qs} + \delta_{qs}) \\
\frac{L_1}{\pi\rho b} &= -\frac{b^2}{8}\ddot{\alpha} - \frac{V_\infty b}{2}\dot{\alpha} - \frac{V_\infty}{2}\dot{\delta} - \frac{V_\infty^2}{2}\delta + V_\infty C(k)(\alpha_{qs} + \delta_{qs}) \\
\frac{L_2}{\pi\rho b} &= \frac{b}{2}\ddot{\zeta} - \frac{ab^2}{2}\ddot{\alpha} - \frac{b}{12}\ddot{\delta} + V_\infty b\dot{\alpha} + \frac{V_\infty^2}{b}\delta,
\end{aligned} \tag{82}$$

where the quasi-steady angle of attack and camber deformations are defined as

$$\begin{aligned}
\alpha_{qs} &= \dot{\zeta} + \Big(\frac{1}{2} - a\Big)b\dot{\alpha} + V_\infty \alpha \\
\delta_{qs} &= \frac{1}{6}\dot{\delta} + \frac{V_\infty}{b}\delta.
\end{aligned} \tag{83}$$

If there are no camber deflections this reduces to Theodorsen's unsteady airfoil theory.

The generalized aerodynamic loads can then be written as

$$\begin{aligned}
L = & \quad \int_{-b}^{b} \Delta p(x)dx & = -L_0 \\
M_{ab} = & \quad -\int_{-b}^{b} \Delta p(x)(x - ab)dx & = bL_1 - abL_0 \\
\Lambda = & \quad -\int_{-b}^{b} \Delta p(x)\Big[\Big(\tfrac{x}{b}\Big)^2 - \tfrac{1}{3}\Big]dx & = \frac{1}{2}L_2 + \frac{1}{6}L_0.
\end{aligned} \tag{84}$$

From Eqs. 82 and 84 it is apparent that both lift and pitching moment are influenced by the camber mode. Since pitch and plunge modes are dependent on the pitching moment and lift, respectively (Eq. 80), the motion of these modes is coupled with parabolic camber.

For an airfoil with only the camber degree of freedom, flutter occurs at a nearly constant reduced frequency per Murua et al. [63]:

$$k_F = -6\frac{G(k_F)}{F(k_F)} \approx 1.07, \tag{85}$$

which gives an approximate solution for nondimensional flutter speed that depends only on inverse mass ratio:

$$\frac{V_F}{b\omega_\delta} = \frac{1}{\sqrt{k_F^2 + C(k_F)\kappa}} \approx (1.14 + 3.91\kappa)^{-1/2}. \tag{86}$$

4.2.3 Verification of Aeroelastic Airfoil Model

The CFD/CSD coupling methodology presented in this thesis thus far has been verified for cross-sectional motions and deflections by comparing results with the analytical solutions for the flutter speed derived by Murua et al. [63]. First, the NLABS parabolic camber mode was examined for NLABS with its F-S aerodynamic model, and then the FUN3D/NLABS solution was compared to these results.

4.2.3.1 Grid Analysis

The NACA 0012 airfoil was chosen for this validation case, as it is in accordance with thin airfoil theory. A grid study was performed in which the damping ratios computed on four grids of various size (Table 5) were compared at $\kappa = 0.1$ with a nondimensional freestream velocity of $V^* = 0.8$. Grids were generated by extruding a two-dimensional unstructured grid onto three planes. Grid cells were hexahedral in the boundary layer and pentahedral in the farfield. In each level of refinement the circumferential resolution was doubled, and the normal grid spacing is defined in Table 5. Grid C predictions resulted in an error in the damping ratio of 2% (Fig. 21) compared to Grid D; this resolution limited the error in flutter speed to less than 0.2%. The remainder of the simulations in the camber and pitch/plunge stability analyses were performed on Grid C.

Table 5: Two-Dimensional NACA 0012 Grids.

Grid	Number of nodes	Initial normal spacing	Normal growth rate	Leading edge spacing	Trailing edge spacing	Maximum circumferential spacing	Damping ratio
A	13,476	1.7×10^{-5} c	1.2	$0.002c$	$0.002c$	$0.02c$	0.1049
B	40,937	8.5×10^{-6} c	1.15	$0.001c$	$0.001c$	$0.01c$	0.0338
C	141,068	4.2×10^{-6} c	1.1	$0.0005c$	$0.0005c$	$0.005c$	0.0304
D	403,226	2.1×10^{-6} c	1.1	$0.00025c$	$0.00025c$	$0.0025c$	0.0312

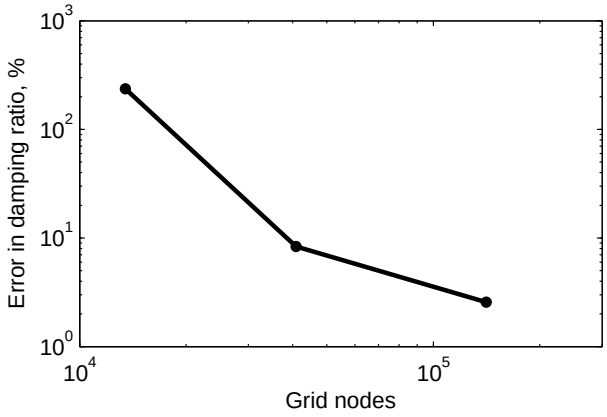

Figure 21: Error in damping ratio versus number of grid nodes, relative to the finest grid of 403k nodes.

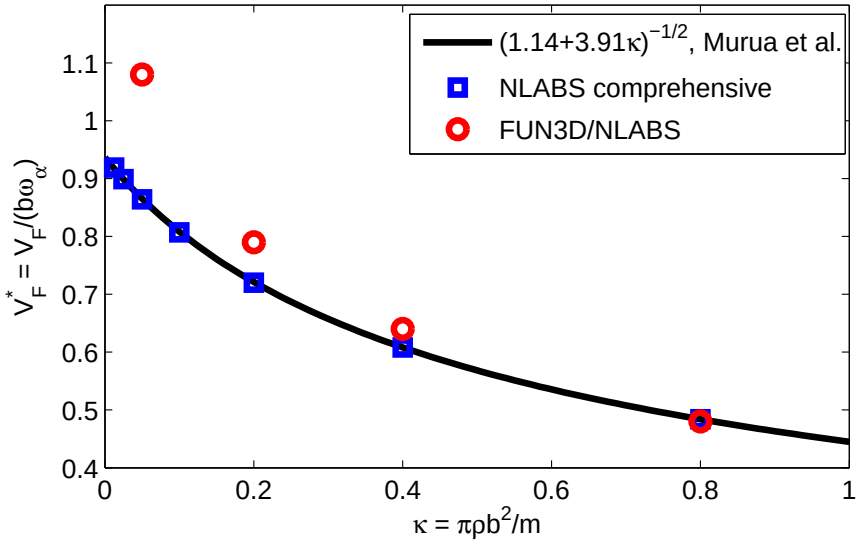

Figure 22: Flutter speed for camber mode.

4.2.3.2 Camber Mode

The stability of a wing section with a single parabolic camber degree of freedom was first evaluated and compared with the approximation (Eq. 86) by Murua [63] using Peters' [64] thin flexible airfoil equations. The approximation of Murua depends only on the inverse mass ratio, $\kappa = \dfrac{\pi \rho_\infty b}{m}$.

Predictions were computed using the finite-state/NLABS (F-S/NLABS) and FUN3D/NLABS solvers. The predictions were computed in the incompressible Mach region, with $m = 112$ kg/m, $I_\delta = 10$ kg/m, $b = 2$ m, and $\omega_\delta = 1$. The freestream density was varied so that values of κ ranged from 0.0125 to 0.8. The flutter speed was determined by performing an iterative analysis of the damping ratio, which were first sampled at various V_∞ values. The flutter speed was determined from the results via linear interpolation at $\zeta_d = 0$. Simulations were performed near the interpolated value for flutter speed in order to ensure that the margin of error was within 1%. Solutions of the flutter speed obtained with the F-S/NLABS code were within 1% of the analytical results of Murua (Fig. 22). Close agreement between Murua's results and F-S/NLABS solutions are expected, since both methods apply Peters' finite-state aerodynamics.

FUN3D/NLABS simulations were performed with nondimensional time steps of 0.016,

which yielded about 500 steps per period of a camber oscillation. These results changed less than 1% when doubling the number of time steps per period. Less than 1% difference between F-S/NLABS and FUN3D/NLABS at $\kappa = 0.8$ (Fig. 22); however, as much as 25% deviation is observed at much lower inverse mass ratios. The larger flutter speeds predicted in the FUN3D/NLABS analysis indicates larger damping when CFD is applied. For all values of κ, the finite-state aerodynamic load predictions lead those of the CFD analysis by 2.5° to 4.9°. However, the derivative of damping ratio with respect to nondimensional velocity $V^* = \dfrac{V}{\omega_\delta b}$ (numerically-computed at the flutter point) varies by two orders of magnitude in the cases evaluated: $\dfrac{\partial \zeta_d}{\partial V^*} \approx -0.09$ for $\kappa = 0.05$ and $\dfrac{\partial \zeta_d}{\partial V^*} \approx -7.4$ for $\kappa = 0.8$. Due to the sensitivity of flutter speed to damping ratio at low inverse mass ratios, the change in flutter speed due to a phase shift in camber loads will be one to two order of magnitude larger at κ =0.05 than at κ =0.8.

There are various assumptions that are made in the Peters' finite-state aerodynamic analysis which are generally assumed to be negligible, but may in fact affect aeroelastic characteristics. First, it is assumed that viscous forces have little influence on lift and moment. The validity of this assumption is investigated by performing an inviscid simulation at $\kappa = 0.05$ and comparing the results to those of the viscous analysis. The grid on which the inviscid simulation was performed had identical circumferential resolution as the grid in the viscous analysis, and contained 86k nodes. Results indicated that including viscosity in the analysis lowered the predicted flutter speed by only 1.4%.

Another assumption of the finite-state aerodynamic formulation is that airfoil deflections are small compared to freestream velocity. In order to determine the influence of the magnitude of deflection on camber stability, the analysis was performed with initial camber deflections of 0.001c to 0.05c. Less than 1% difference in damping ratio was observed as a result of the magnitude of deflections.

Finally, in the inflow model, the wake is constrained to the x axis, with no movement in the vertical direction. Jones and Platzer[150] evaluated the unsteady thrust and drag on a pitching and plunging airfoil at frequency ratios of 0.1 to 4. They performed a panel method analysis with wake elements that were allowed to move freely in the downstream

and vertical directions. Flutter speed predictions were compared to predictions in which a linear wake model was employed. Results indicated that at reduced frequencies higher than 0.5, wake deformation can have significant influence on aerodynamic loads, and that roll-up of the wake vortices was the primary source in variation of the nonlinear and linear wake results. At flutter speed for isolated camber deflections flutter occurs at approximately $k = 1.07$, indicating that nonlinear wake effects may have a significant effect on flutter speeds.

4.2.3.3 Pitching and Plunging Modes

Theodorsen and Garrick [148] computed flutter velocities as a function of elastic axis location, center of mass, and inverse mass ratio. Zeiler [151] re-evaluated these results and presented corrected solutions, three of which are selected for analysis here. The nondimensional structural and fluid properties for these cases evaluated were: $a = -0.3$, $\kappa = 0.05$, and $r_\alpha^2 = 0.25$. In the three respective cases, values of $x_\alpha = 0.0, 0.1$, and 0.2 are assigned for center of mass, which is measured in semichords aft of the aeroelastic axis.

For all three cases the F-S/NLABS flutter speed predictions were within 3% of those presented by Zeiler [151] (Fig. 23), as expected, since both analyses apply Peters' flexible thin airfoil theory.

Computations for the case where $x_\alpha = 0.1$ were next performed with the FUN3D/NLABS aeroelastic solver. There was less than 5% difference between CFD and finite-state aerodynamics in flutter speed predictions for values of $\omega_\zeta/\omega_\alpha$ less or equal to 0.9, while the CFD solution deviated from the finite-state predictions by 47% at $\omega_\zeta/\omega_\alpha$ =1.4 (Fig. 23). At frequency ratios larger than 0.9, the pitch mode begins to dominate the flutter motion. Linear theory predicts that the aerodynamic center and center of pressure are located at the quarter-chord. In an analysis of pitching moment at various angles of attack the aerodynamic center deviated by $0.004c$ from the quarter-chord. These results are consistent with experimental measurements of Pope [152] and Critzos et al. [153], as well as computational results of Smith et al. [154].

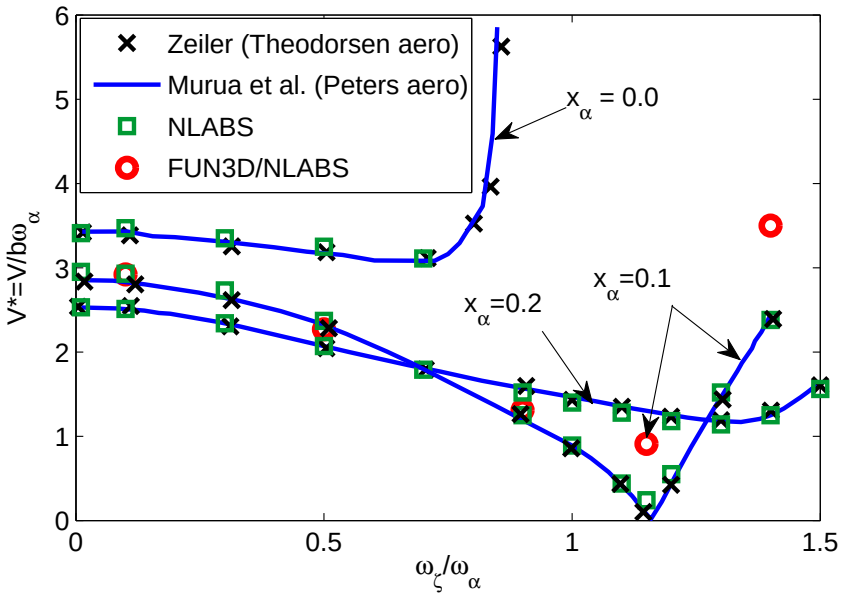

Figure 23: Flutter speed for pitch-plunge modes.

4.3 Summary of Verification Cases

The one-dimensional elastic beam model implemented in NLABS has been validated through comparison of performance characteristics in hover at 7.6° collective pitch. The influence of elastic deformation is observed in the elastic twist caused by the nose-down pitching moment of the NACA 23012 airfoil section, which leads to lower blade loading. Sectional normal force and blade tip deflections have also been compared with measurements from the HART II test at $\mu = 0.15$. A sectional analysis has also been performed to verify the pitch and plunge modes, as well as the parabolic camber mode. These results indicate that the methodology has successfully extended computational aeroelastic evaluation capabilities to full three-dimensional blade deformation.

CHAPTER V

BLADE SECTION STABILITY IN COMPRESSIBLE FLOW

The F-S/NLABS and FUN3D/NLABS analyses have also been applied to a NACA 23012 airfoil at subsonic compressible free stream velocities to determine the minimum stiffness required for a flexible airfoil section to remain stable. The airfoil is that of the rotor used in the Hover Tip Vortex Structure (HOTIS) test [120]. The torsion and flap stiffnesses (126 N-m/rad and 15.4 kN/m, respectively) were chosen so that the natural frequencies correspond to the first natural frequencies of twist (415 rad/s) and flap (121 rad/s) of the rotor rotating at 109 rad/s. Simulations were performed at three nondimensional velocities of 6.5, 8.7, and 10.8 (M_∞=0.48, 0.64, and 0.80, respectively). These correspond to the velocity at $0.75R$ and $1.0R$ in hover, and the maximum tip velocity during forward flight at $\mu = 0.25$. The inverse mass ratio is 0.0148, and the elastic axis and center of mass are located at the quarter chord.

5.1 Finite-State/NLABS

Results with NLABS using finite-state aerodynamics indicate that static divergence due to camber-pitch coupling was encountered before the onset of flutter. The static deflections of the airfoil (Fig. 24) identify the minimum frequency ratios required for stability at $V^* =$ 6.5, 8.7, and 10.8 to be approximately $\omega_\delta/\omega_\alpha = 12$, 24 and 72, respectively.

5.2 FUN3D/NLABS

Simulations were next performed with the FUN3D/NLABS code. Time step and grid analyses were first performed to verify convergence.

5.2.1 Time Step Analysis

A time step analysis using a baseline grid of 35k nodes was performed to determine the temporal resolution required to minimize temporal errors. The test was performed at Mach

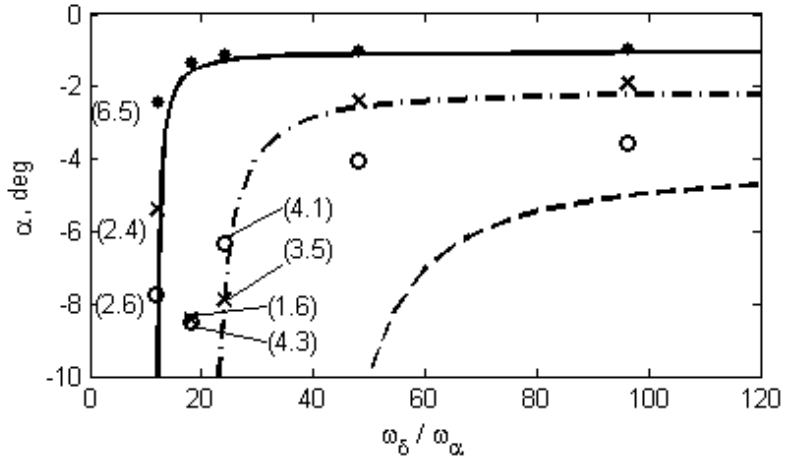

(a) Pitch

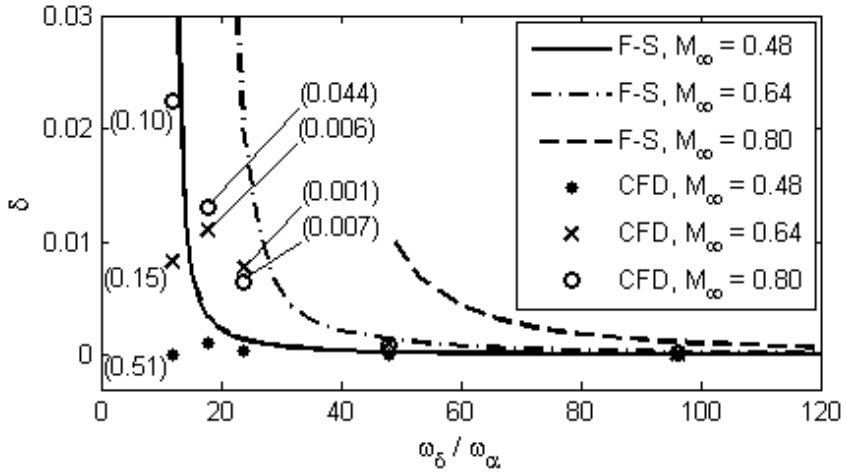

(b) Camber

Figure 24: Mean deflections for NACA 23012 airfoil. The amplitude of unsteady deflections is indicated in parentheses when present. The response was steady for all cases when finite-state aerodynamics were used.

0.64 with a camber stiffness corresponding to $\omega_\delta/\omega_\alpha = 240$, which is one order of magnitude larger than the stability point determined using lower-order aerodynamics. The analysis was performed for three different time steps, corresponding to 50, 100, and 200 time steps per camber oscillation period. Damping ratios were extracted from the camber response, and the error associated with 50 and 100 steps per period is within 6% and 1% with respect to the case with 200 steps, indicating that 100 steps per period are necessary to accurately determine stability.

5.2.2 Grid Analysis

Results of the prior grid analysis were applied in the development of the NACA 23012 grids. FUN3D/NLABS simulations were performed on two-dimensional grids (Table 6) to verify sufficient resolution in the circumferential direction. In the boundary layer hexahedral cells were generated with normal spacing of the first cell equal to $6.75 \times 10^{-6}c$, providing 36–44 points in the normal direction to capture the boundary layer, as recommended by Smith et al. [155]. For static computations at 5.9° pitch and an Re = 1.8 million, the predicted lift and moment coefficients of the two grids are within 0.1% of one another.

Table 6: Two-Dimensional NACA 23012 Grids.

Grid	Number of nodes	Leading edge spacing	Trailing edge spacing	Maximum circumferential spacing	c_m	c_l
A	35,455	$0.0014c$	$0.0014c$	$0.014c$	−0.0147	0.801
B	103,723	$0.0007c$	$0.0007c$	$0.007c$	−0.0147	0.802

5.2.3 Results

In cases where the flow remained subsonic over the airfoil ($M_\infty = 0.48$ and 0.64 at $0° < \alpha < -3°$), the pitch deflections of the F-S/NLABS and FUN3D/NLABS simulations agree to within 10% at $M_\infty = 0.48$ and within 12% at $M_\infty = 0.64$. As stiffness decreases, the airfoil deflections increase, and the flow becomes transonic. The behavior of the NLABS and FUN3D/NLABS simulations begins to diverge as the local flow becomes transonic. At $M_\infty = 0.80$, flow was transonic at all angles of attack, resulting in discrepancies in pitch

larger than 41%, regardless of camber stiffness. In all cases (Figs. 24(a) and 24(b)) the magnitude of steady pitch and camber deflections predicted by NLABS are larger than those predicted by FUN3D/NLABS.

FUN3D/NLABS results predict a blade with increasing unsteady pitch (Fig. 24(a)) and camber (Fig. 24(b)) as the camber stiffness approaches the flutter point. Large airfoil deflections and transonic flow produce separation vortices, which introduce unsteady pressure loads that drive the oscillatory deflections. These vortices are not modeled by the finite-state aerodynamic model in NLABS, and as a result the NLABS deflections were steady. In the following sections the influence of transonic flow and separation vortices on aeroelastic behavior are further examined.

At $M_\infty = 0.48$ flow remains subsonic until the camber stiffness approaches the divergence point, which occurs at $\omega_\delta/\omega_\alpha = 12.0$. At $\omega_\delta/\omega_\alpha = 12.0$, the camber deflection becomes very large, and shocks near the leading edge (Fig. 25) and boundary layer separation generate large pressure gradients that drive the pitch and camber oscillations.

At $M_\infty = 0.64$, when $\omega_\delta/\omega_\alpha = 24.1$ the magnitude of unsteady camber deflections is less than $1\%c$, but it produces sufficient pitching moment to significantly alter the pitch deflection (Fig. 24). As the camber stiffness continues to decrease, camber deflections begin to dominate the oscillatory deflections (Fig. 26). Transonic flow and stall occur only as the magnitude of airfoil deflection increases. At t_1 in Fig. 26(b) a discontinuity is present in which the pressure coefficient after the shock on the lower surface at $x/c = 0.45$. The slope of the c_p versus x curve suddenly changes sign, and there is a small increase and subsequent decrease in pressure due to a separation bubble that will later be examined in flowfield visualization.

At $M_\infty = 0.80$ transonic flow over the airfoil results in multiple shocks and separated flow, on both the upper and lower surface of the airfoil (Fig. 27). This alters the pitching moment, resulting in a significant difference in pitching moment between the F-S/NLABS and FUN3D/NLABS solutions. The nonlinear aerodynamic effects decrease the magnitude of pitch deflections and improve the stability compared to predictions of the finite-state

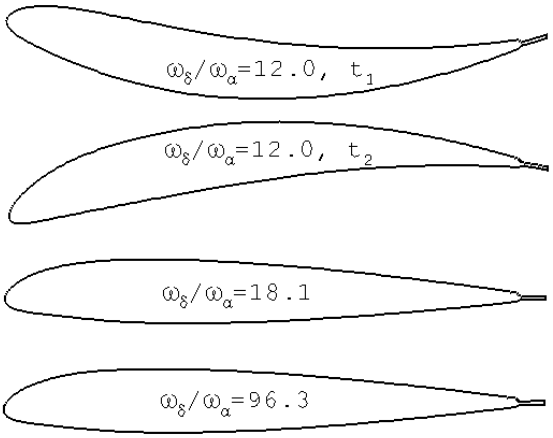

(a) Airfoil shape

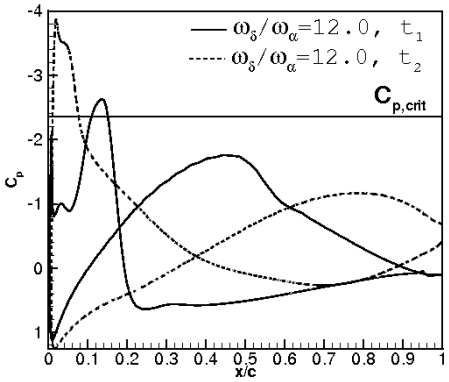

(b) $\omega_\delta/\omega_\alpha = 12.1$

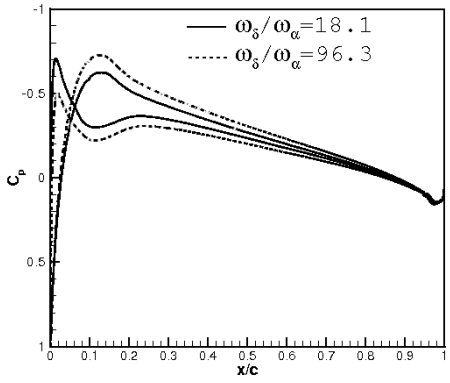

(c) $\omega_\delta/\omega_\alpha = 18.1, 96.3$

Figure 25: Airfoil surface and pressure coefficients for aeroelastic two-dimensional BO-105 blade sections with CFD/CSD coupling at Mach 0.48, $V^* = 6.5$

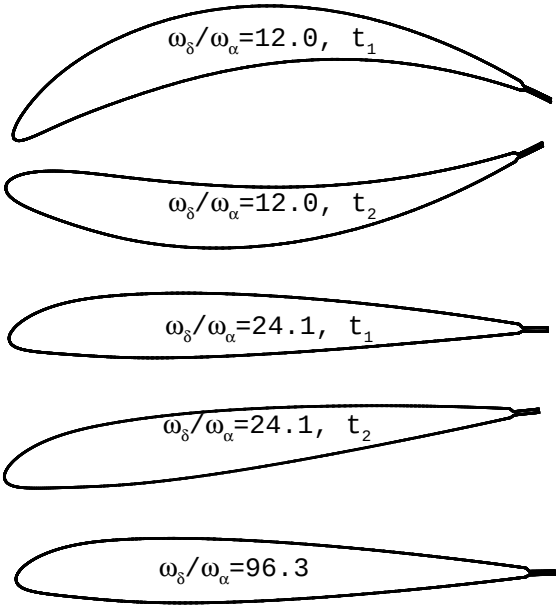

(a) Airfoil shape

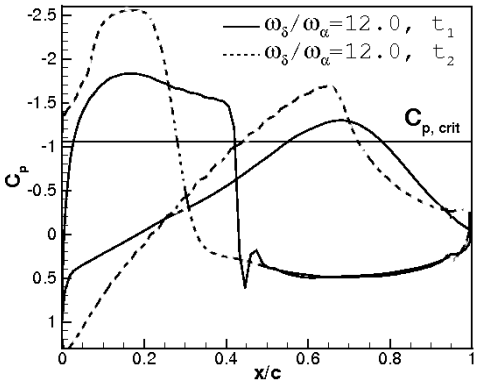

(b) $\omega_\delta/\omega_\alpha = 12.0$

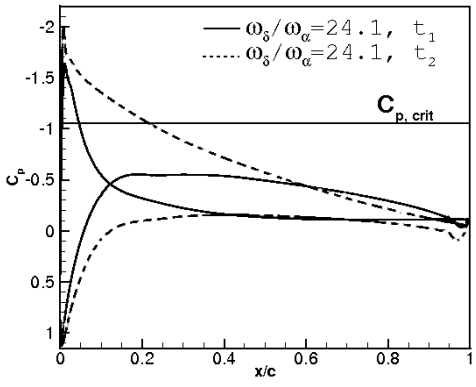

(c) $\omega_\delta/\omega_\alpha = 24.1$

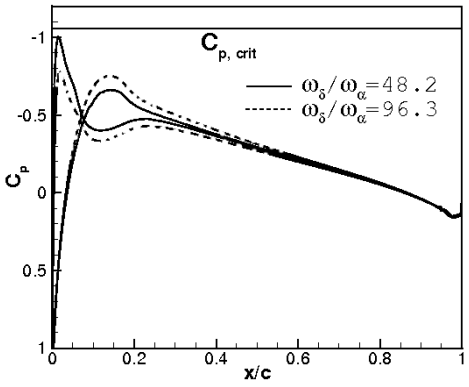

(d) $\omega_\delta/\omega_\alpha = 48.2, 96.3$

Figure 26: Airfoil surface and pressure coefficients for aeroelastic two-dimensional BO-105 blade sections with CFD/CSD coupling at Mach 0.64, $V^* = 8.7$

model. As camber stiffness decreases to the point where $\omega_\delta/\omega_\alpha = 24.1$, large pitch deflections are observed, followed by large camber deflections after further decreasing stiffness.

5.2.4 Evaluation of Nonlinear Aerodynamics

The history of loads at M_∞=0.64 are further examined to determine the nature of the unsteady nonlinear aeroelastic behavior of the airfoil. As the camber stiffness is decreased, pitch deflections become larger, and nonlinear effects cause unsteady airfoil loads resulting in limit cycle oscillations at low frequencies due to the plunge mode, and higher frequencies due to the pitch and camber modes (Fig. 28(a)) At lower camber stiffness, the camber deflections become larger and begin to dominate the physical nature of the flow. These high-frequency oscillations also drive pitch oscillations, while the plunge mode is damped (Fig. 28(b)).

A single camber oscillation period (Fig. 29) is next analyzed to examine the effects of transonic flow and separation vortices. Flow contours are examined at time intervals s =0.9, from 0.0 to 7.2.

At s =1.8 a vortex forms on the lower surface of the airfoil due to the large camber deflection (Fig. 30(c)). As the vortex travels along the lower side of the airfoil, it creates a low-pressure region near the midchord, driving a negative camber deflection (Fig. 30, s =2.7–4.5). At the same time, a shock forms at 60%c on the upper surface and moves forward until it reaches the leading edge (Fig. 30(b), s =2.7–6.3). The shock induces boundary layer separation, resulting in a new vortex on the upper surface of the airfoil ((Fig. 30(c)). As this vortex passes the midchord of the airfoil it creates a low-pressure region on the upper surface, which drives a positive camber deflection (Fig. 30(d), s =6.3–7.2, s =0.0–1.8). At s =1.8 the vortex on the upper surface reaches the trailing edge as another separation vortex forms on the lower surface at the leading edge, and the cycle repeats.

The stability limit for the case at M_∞=0.48, which corresponds to 0.75R for the HART II rotor, is $\omega_\delta/\omega_\alpha$=12. The dimensional frequency for this value is 5000 rad/s, or 800 Hz.

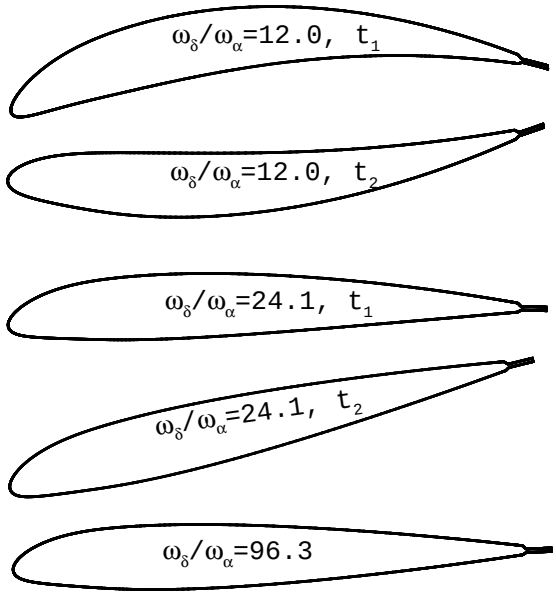

(a) Airfoil shape

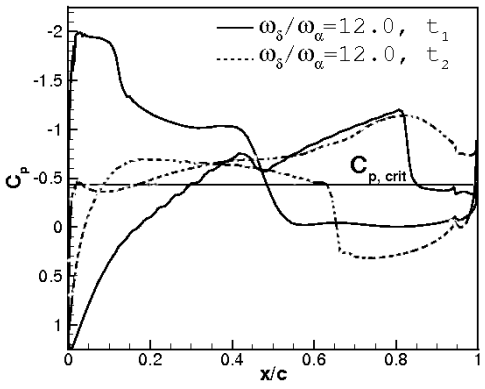

(b) $\omega_\delta/\omega_\alpha = 12.0$

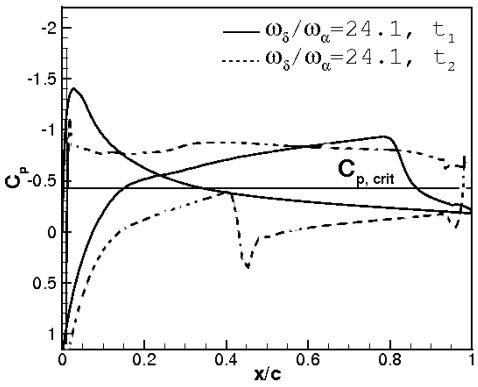

(c) $\omega_\delta/\omega_\alpha = 24.1$

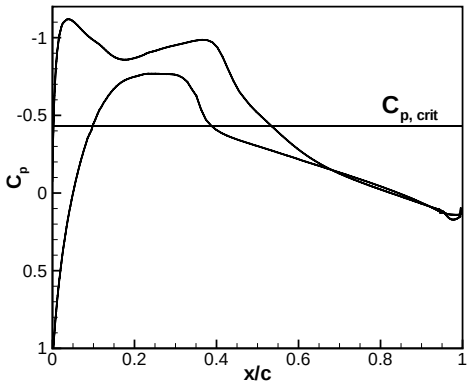

(d) $\omega_\delta/\omega_\alpha = 96.3$

Figure 27: Airfoil surface and pressure coefficients for aeroelastic two-dimensional BO-105 blade sections with CFD/CSD coupling at Mach 0.80, $V^* = 10.8$

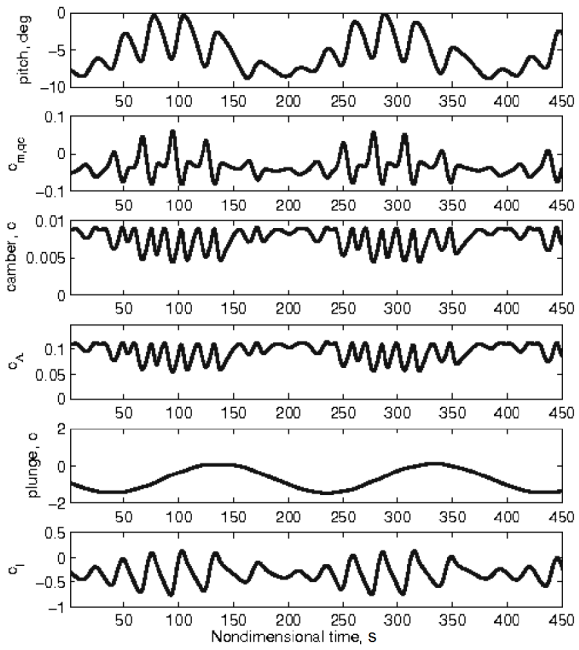

(a) $\omega_\delta/\omega_\alpha = 24.1$

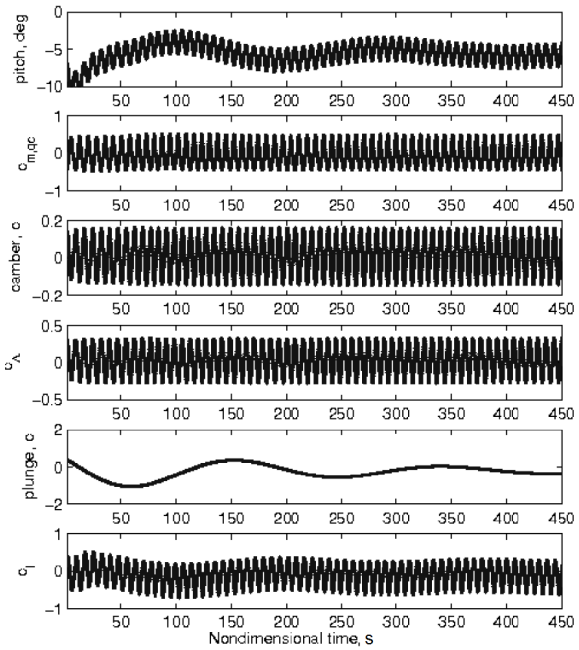

(b) $\omega_\delta/\omega_\alpha = 12.0$

Figure 28: Time history of aeroelastic response for CFD/CSD coupling at Mach 0.64

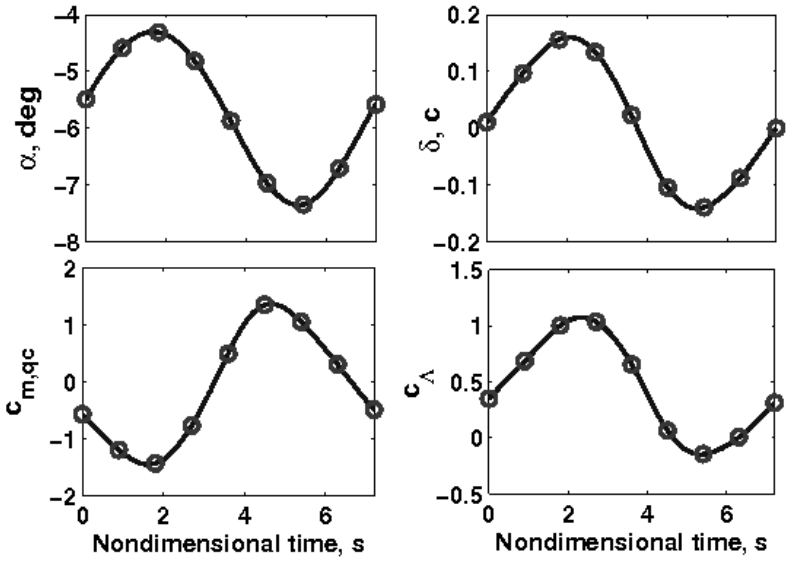

Figure 29: Aeroelastic response over one period for CFD/CSD coupling at Mach 0.64 and $\omega_\delta/\omega_\alpha = 12.0$. Circles in Fig. 30 indicate instances at which the flowfield is examined, occurring at time intervals of dt^*=0.9

The camber stiffness for the HART II rotor is not documented so that there are no data for comparison. For most rotors the airfoil stiffness is very high to ensure that camber deflections are negligible. However, for deformable airfoils the use of compliant materials reduces the stiffness, making them more susceptible to instability.

In comparable experimental studies a unimorph cambering airfoil design based on the NACA 0010 airfoil was analyzed by Bilgen et al. [35]. They measured the frequency of the first airfoil bending harmonic to be 270 Hz for a wing section of chord length 0.163 m, which is comparable to the stability limit in the present study.

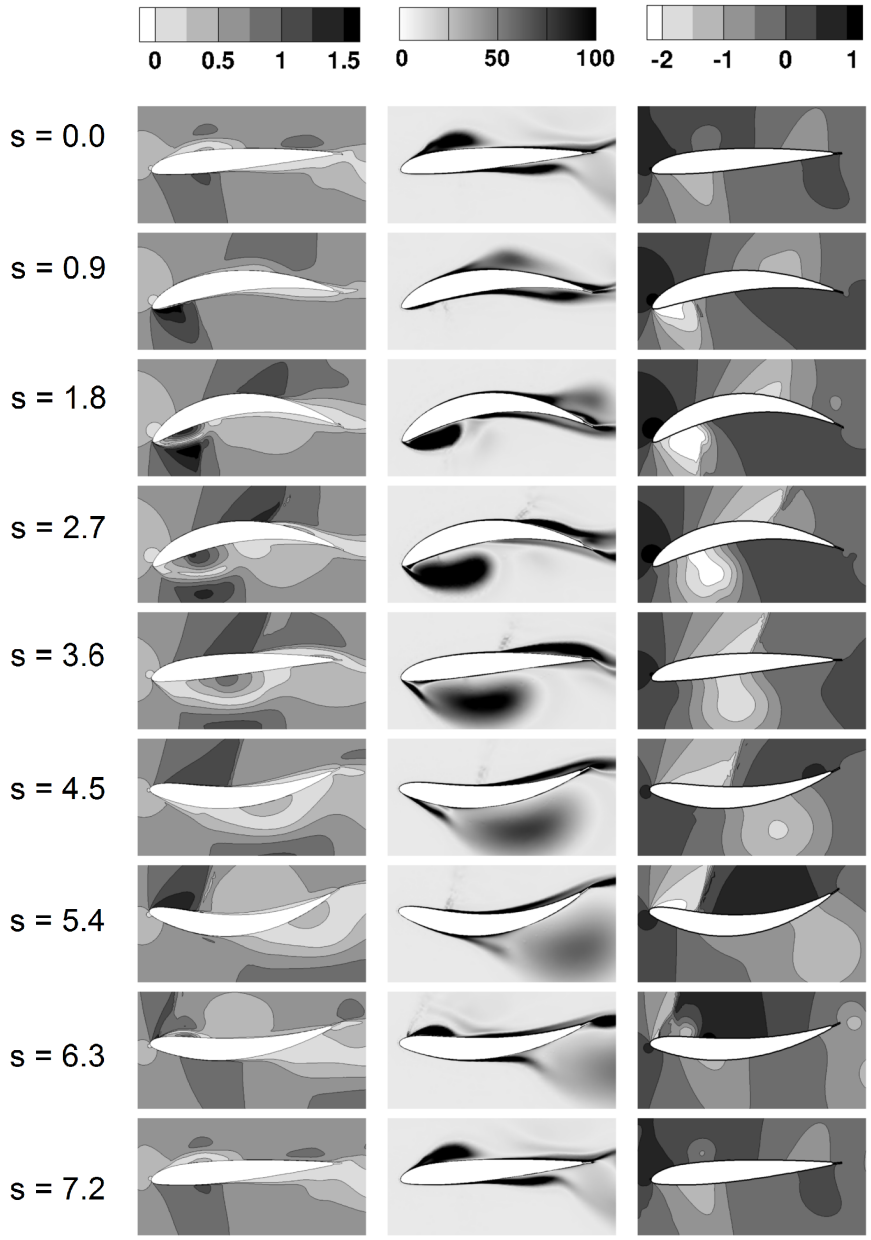

(a) Time (b) Mach number (c) Vorticity magnitude (d) Pressure coefficient

Figure 30: Mach, vorticity, and pressure contours for the NACA 23012 airfoil at $M_\infty = 0.64$, $\omega_\delta/\omega_\alpha$=12.0, corresponding to the load/deflection history in Fig. 29.

CHAPTER VI

FORWARD FLIGHT ROTOR ANALYSIS WITH ACTIVE CAMBER

The methodology is next evaluated for a three-dimensional rotor with active camber. To isolate camber response to control input, camber stiffness was increased to $\sim 10^{20}$ so that deflections were influenced only by prescribed camber loads. The influence of prescribed camber deflection on rotor performance and vibratory loading was then assessed.

6.1 Rotor Specifications and Flight Conditions

Specifications for the forward flight case were based on the Higher Harmonic Control (HHC) Aeroacoustic Rotor Test (HART) test [119] performed at DLR in 1995. In this experiment, a 40% scaled of the four-bladed BO-105 rotor was tested inside a wind tunnel at various flight conditions. Structural dimensions and properties are available from the HART II experiment, and are listed in Table 2. The flight conditions and trim conditions for the case investigated in this study are shown in Table 7.

Table 7: HART Test Case Configuration

μ	0.25
M_{tip}	0.64
Re_{tip}, million	1.80
α_s, deg	-5.0
Thrust, N	3100
Roll moment, N	0
Pitch moment, N	0

A harmonic generalized forcing function was applied to drive active parabolic camber deflections centered at the midchord, and are defined by the following the following function [127]:

$$\Psi = \begin{bmatrix} 0 \\ 0 \\ \xi^2 - \frac{1}{3} \end{bmatrix}. \tag{87}$$

6.2 CSD Model

The CSD model consists of a nonlinear one-dimensional beam along the radius of the blade as well as a two-dimensional model of the airfoil section at each radial station. At the fluid-structure interface, 80 nodes define the cross section of the blade at each of 44 spanwise stations. The mass and stiffness matrices, which include six degrees of freedom for beam section translation and rotation, as well as one degree of freedom for camber, are specified from the structural properties outlined in Table 2.

6.3 CFD Grid Independence

The blade grid used in the forward flight cases is the same as that used in the hover simulation in Section 4.1. Grid independence has been verified for hover cases, but grid requirements may be more constrictive in forward flight, due to the influence of transonic flow and boundary layer separation. Therefore, the coarse, medium, and fine grids of Table 3 were again analyzed in a baseline forward flight case with rigid airfoil sections and in an active-rotor case in which harmonic parabolic camber was forced.

The simulations were performed with a radially elastic blade and rigid airfoil. Each case was trimmed to 3100 N with zero pitch and roll moments by trimming the collective and cyclic pitch angles. The trimmed collective pitch setting is 0.3 degrees smaller with the medium and fine grid than with the coarse grid (Table 8). The primary cause is that the nose-down pitching moment is significantly lower over the entire rotor disk in the medium and fine cases (Fig. 31), resulting in a larger angle of attack for a given control setting, thus requiring a smaller collective pitch. The average nose-down pitching moment is 25% smaller in magnitude for the medium grid and 23% smaller for the fine grid. The trim differences (Table 8) may also be attributed in part to the $1-2\%$ differences in lift predictions between the blade grids for a given pitch. The drag coefficient, averaged over the rotor disk, is 22% smaller for both the medium and fine grid compared to the coarse grid (Fig. 32). Contour plots of the normal force and drag (Figs. 33–32) indicate that the influence of the tip vortex is captured with more resolution in the medium and fine cases. This is evident in the increased gradient in lift at $r/R = 0.65$ between $\psi = 160^\circ$ and $\psi = 180^\circ$ and the reduced

drag at $r/R = 0.65$ between $\psi = 106°$ and $\psi = 270°$, which corresponds to the location of the tip vortex observed in the Q criterion (second invariant of the velocity gradient tensor) isosurface (Fig. 34). The effects of the tip vortex are diminished due to dissipation when coarse grid spacing is used.

Table 8: Trim settings for various grids (3100 N thrust, 0 N-m pitch and roll moments).

	Coarse	Medium	Fine
θ_0	10.8	10.5	10.5
θ_{1c}	-2.5	-2.6	-2.6
θ_{1s}	0.7	0.6	0.7

A blade section at $75\%R$ is next examined. The instantaneous normal force (Fig. 35) values differs by at most 8% between the coarse and fine grid, and 4% between the medium and fine grid. There is also a phase shift of up to 10° between the coarse and fine unsteady normal force, while the medium and fine normal force phases agree.

The predicted mean pitching moment is 25% and 26% lower with the medium and fine grids, respectively, than with the coarse grid (Fig. 36(a)). The unsteady pitching moment of the coarse grid differs in magnitude near 90° and 360° (Fig. 36(b)) while both the medium and fine grid cases phases agree and magnitude.

There are large offsets (22% to 26%) in the average drag and moment coefficient of the coarse grid compared to the medium and fine grids. In addition, the trimmed collective pitch of the coarse grid is 3% higher than that of the medium and fine grids. In contrast, the medium and fine grids agree within 4% in instantaneous normal forces, and within 1% in collective trim, average pitching moment, and average drag coefficient. It was concluded that the medium grid was sufficiently grid independent, and it was used for subsequent simulations.

6.4 Rotor with Rigid Airfoil

The next evaluation of the methodology's validity was a comparison of the periodically-converged, trimmed responses of the NLABS and FUN3D/NLABS analyses, which at non-transonic, non-stall conditions delineated earlier should provide similar trends for the lift.

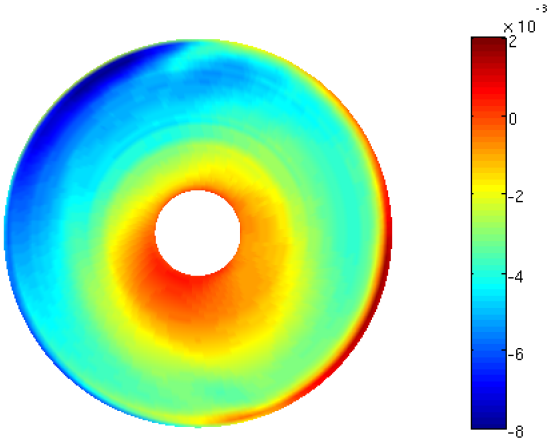

(a) Coarse

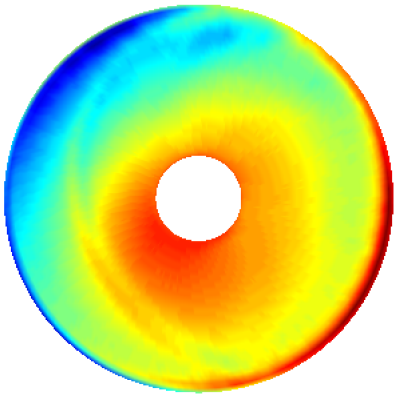

(b) Medium

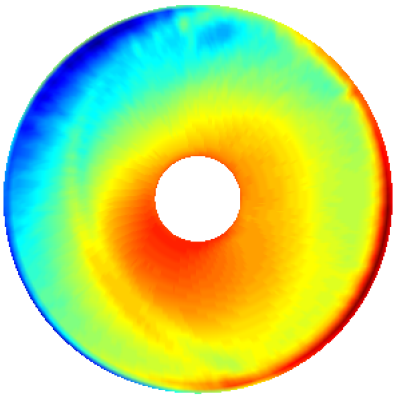

(c) Fine

Figure 31: Pitching moment, $M^2 c_m$, HART II baseline case, $\mu = 0.15, \alpha_s = -5.0$ (freestream left to right).

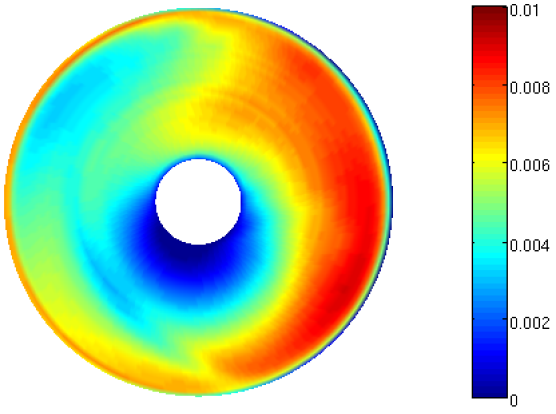

(a) Coarse

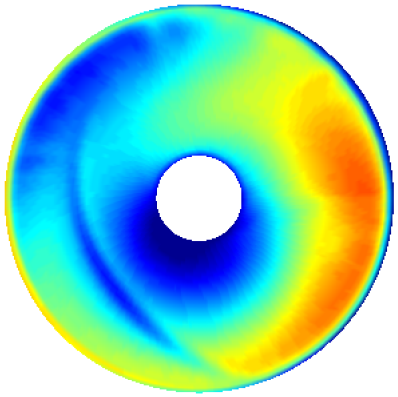

(b) Medium

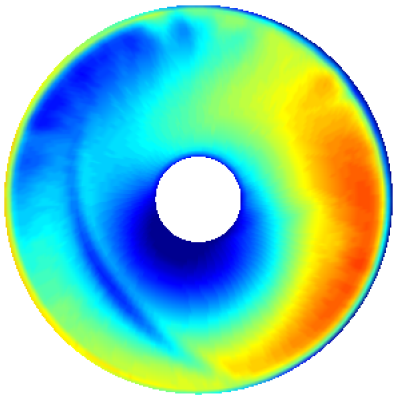

(c) Fine

Figure 32: Drag, $M^2 c_d$, HART II baseline cas, $\mu = 0.15, \alpha_s = -5.0$e (freestream left to right).

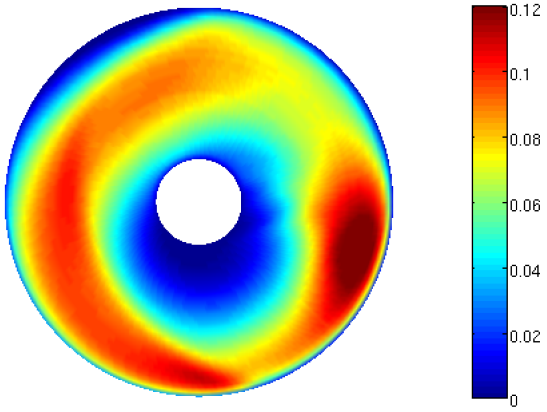

(a) Coarse

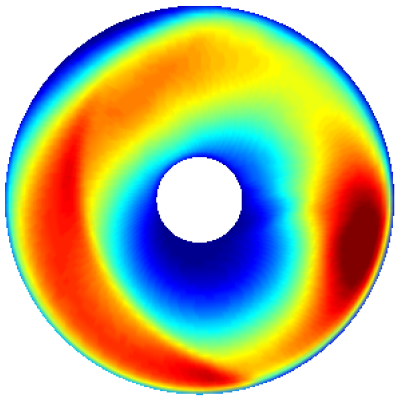

(b) Medium

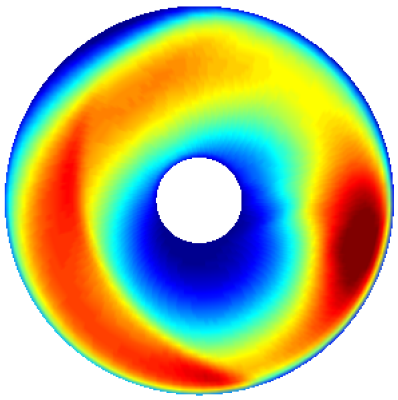

(c) Fine

Figure 33: Normal force, $M^2 c_n$, HART II baseline case, $\mu = 0.15, \alpha_s = -5.0$ (freestream left to right).

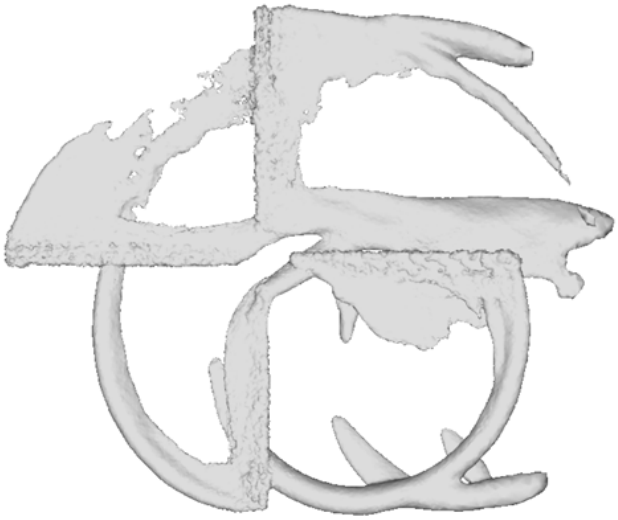

Figure 34: Q criterion isosurface, HART II baseline case, $\mu = 0.15, \alpha_s = -5.0$ (freestream left to right).

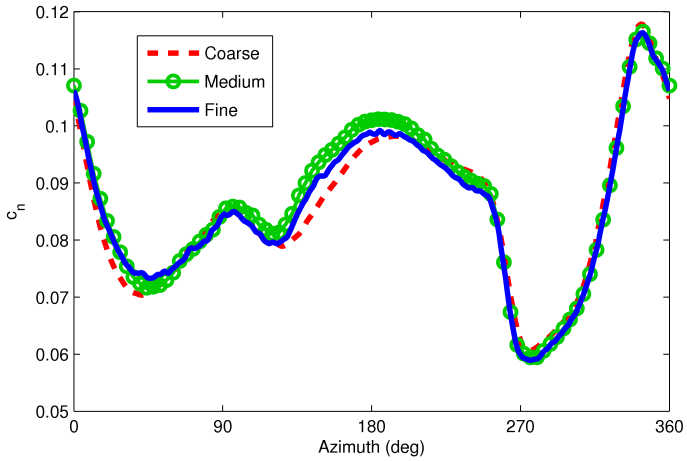

Figure 35: Normal force at $75\%R$, HART II baseline case, $\mu = 0.15, \alpha_s = -5.0$ (freestream left to right).

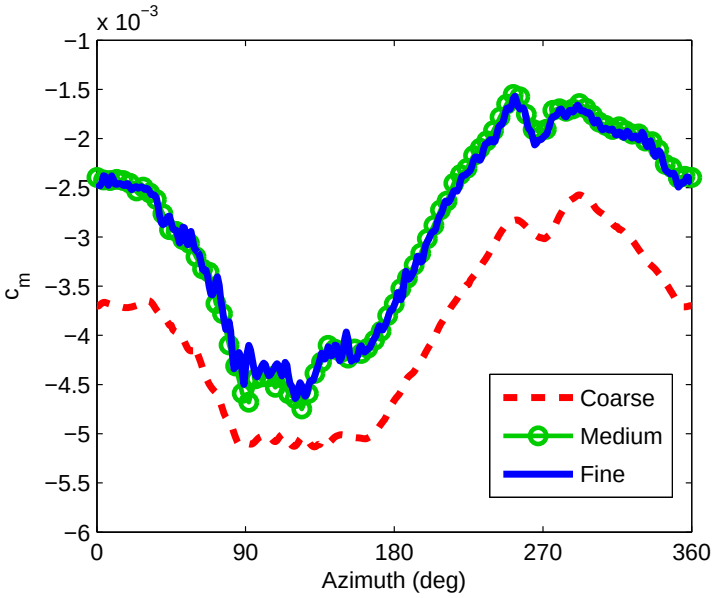

(a) Total moment

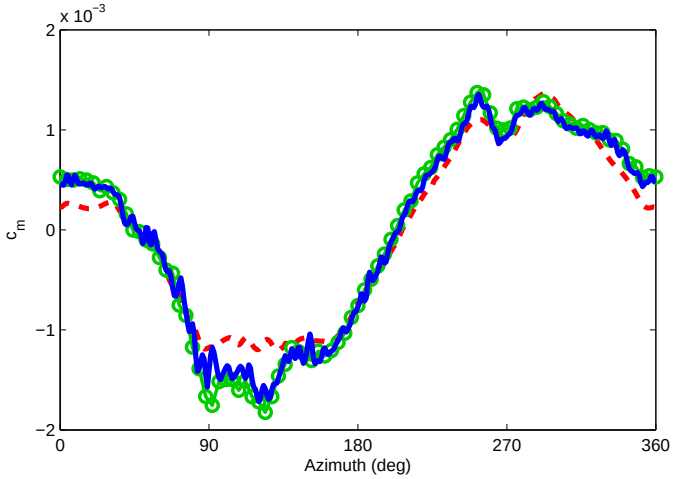

(b) Mean removed

Figure 36: Pitching moment at $75\%R$, HART II baseline case, $\mu = 0.15, \alpha_s = -5.0$ (freestream left to right).

The analysis was first performed for two baseline cases without camber actuation. The elastic axis of the blade was allowed to bend and twist, while the blade cross sections remained rigid. To reduce computational time for the CFD/CSD simulation, a converged solution from F-S/NLABS was used as a starting solution. After a converged solution was achieved, the coupled FUN3D/NLABS code was applied.

6.4.1 Baseline Comparison of Finite-State and CFD Aerodynamics

The baseline case was simulated at an advance ratio of 0.25, trimming the thrust to 3100 N and the longitudinal and lateral hub moments to 0 N-m. The computational results of the NLABS simulation were compared in detail to those of the FUN3D/NLABS simulation.

The trim and structural solution of the NLABS simulation were used as a starting point for the FUN3D/NLABS simulation. To transition from Peters' finite-state aerodynamics to CFD aerodynamics, a weighting function (Eq. 65) was applied. Three different schedules for transitioning from F-S to CFD airloads were compared. In each schedule the transition was initiated after one complete revolution. The transition was completed over three different azimuthal periods: 0° (step transition), 180°, and 360°.

Although the step transition results in higher excursions in magnitude of trim and airloads from the converged value, the convergence time is smaller than when a ramp transition is used. This indicates that the aerodynamic damping is large enough to prevent oscillations in the control settings. The control pitch and cyclic pitch were trimmed in NLABS to achieve the trim targets. The trimmed control pitch using aerodynamic loads from FUN3D was slightly larger than when low-order aerodynamics were used, while the cyclic controls were slightly smaller in magnitude, as listed in Table 9.

Table 9: Converged control settings for forward flight case.

Controls	CFD	Finite-state
θ_0, deg	10.51	10.19
θ_{1c}, deg	0.63	0.86
θ_{1s}, deg	-2.55	-2.82

Qualitatively, the NLABS and FUN3D/NLABS simulations provide a similar normal

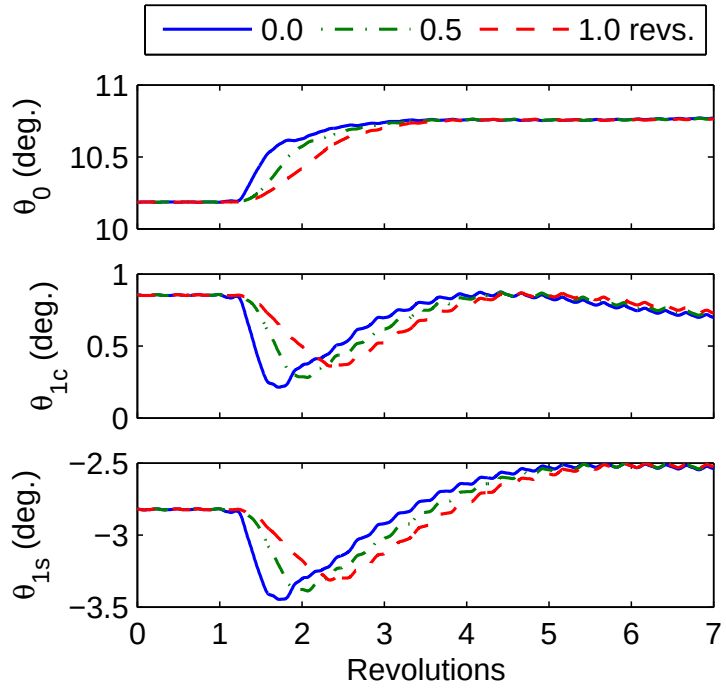

(a) Control history

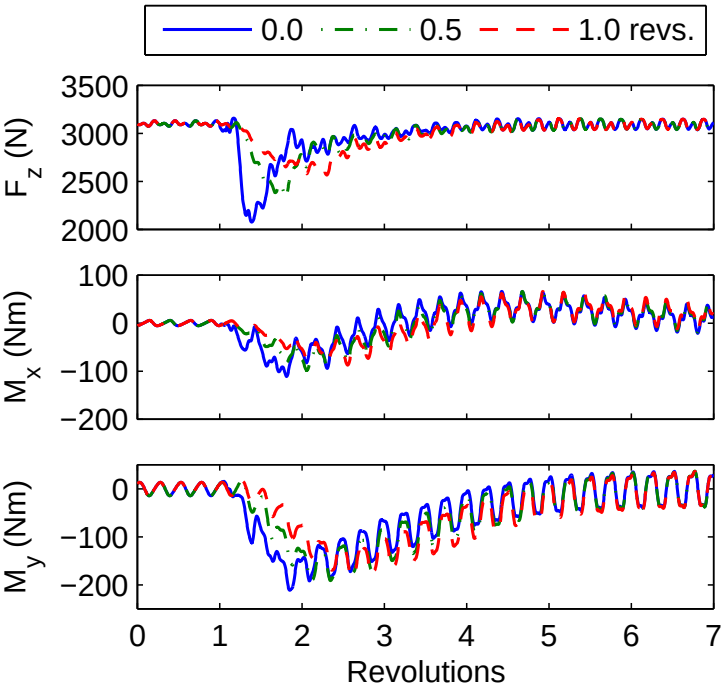

(b) Hub load history

Figure 37: Convergence of loads and controls using stepped/ramped CSD-to-CFD loading transition (legend indicates number of revolutions completed while transitioning from low-order loads to CFD loads).

force distribution over blade span and azimuth (Fig. 38). Between 0° and 20° the normal force distribution shifts slightly inboard when CFD loads are applied, and between 135° and 280° the influence of the tip vortex is dissipated in the F-S results. This second discrepancy is investigated in Section 6.6 to determine if more fidelity can be provided by the low-order finite-state aerodynamic model in NLABS.

F-S/NLABS predictions of the pitching moment are much smaller than FUN3D/NLABS predictions for almost all spanwise and azimuthal positions (Fig. 39). In addition, the influence of the tip vortex observed in the FUN3D/NLABS moment predictions (Fig. 39(b)) is completely absent in the F-S moment predictions (Fig. 39(a)). The pitching moments are sampled at $50\%R$, $75\%R$, and $90\%R$ for further analysis.

A large offset in the pitching moment is observed between the NLABS and FUN3D/NLABS results (Fig. 40). While the one-per-revolution pitching moment responses predicted by NLABS and FUN3D/NLABS are in phase, the magnitude of the nose-down pitching moment predicted by NLABS is $40 - 75\%$ lower than the pitching moment predicted by FUN3D/NLABS at all three radial stations.

The impact of pitching moment on elastic twist is observed in Fig. 41. Due to the large nose-down pitching moment on the advancing side of the rotor, the blade pitches down. These results indicate that elastic twist has a large contribution to the differences in the trim solution observed in Table 9. The collective pitch must be increased to compensate for the nose-down twist, so that the specified thrust can be achieved. Since largest deflections are in the second quadrant the lateral control must decrease and the longitudinal control must increase to maintain the balance of loads over the rotor disk.

Since there is no pre-cone angle in HART II cases, the blade tip is deflected upward (Fig. 42), with largest tip deflections occurring on the retreating side of the blade near 270° azimuth. Larger tip deflections occur on the retreating side of the blade due to the outboard shifting of blade loads as the dynamic pressure near the hub becomes very low.

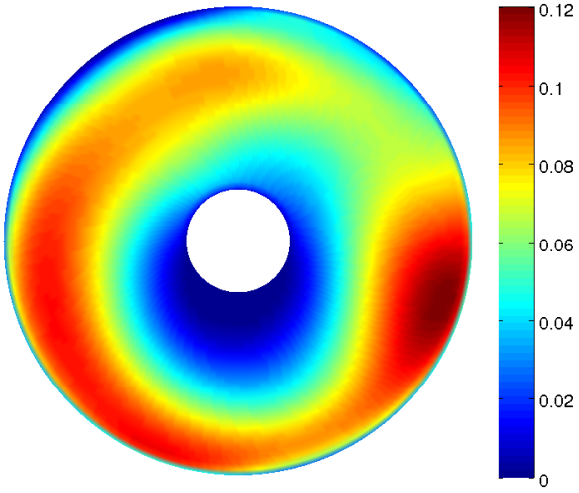

(a) F-S/NLABS

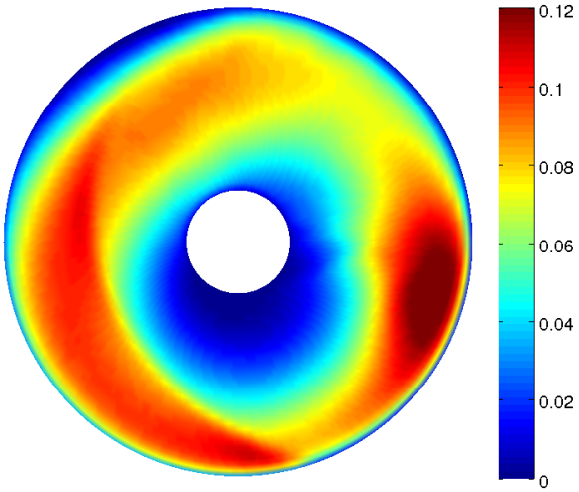

(b) FUN3D/NLABS

Figure 38: Normal force, $M^2 c_n$, for F-S/NLABS and FUN3D/NLABS HART II baseline cases at $\mu = 0.25$ with $\alpha_s = -5.0$.

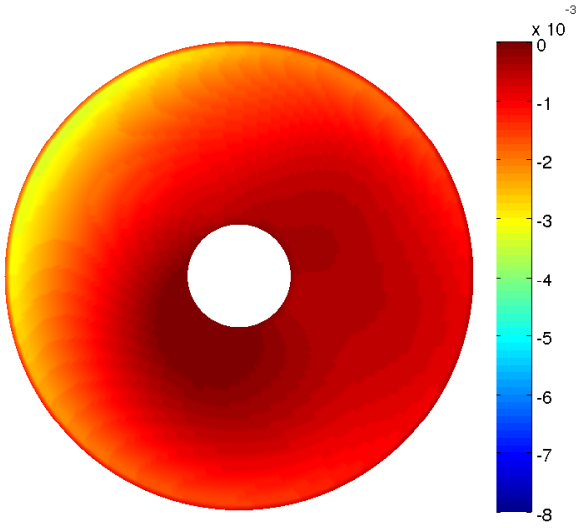

(a) F-S/NLABS

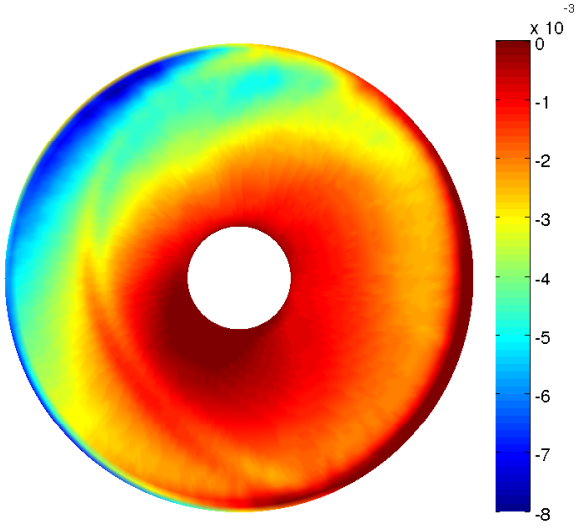

(b) FUN3D/NLABS

Figure 39: Pitching moment, $M^2 c_m$, for F-S/NLABS and FUN3D/NLABS HART II baseline cases at $\mu = 0.25$ with $\alpha_s = -5.0$.

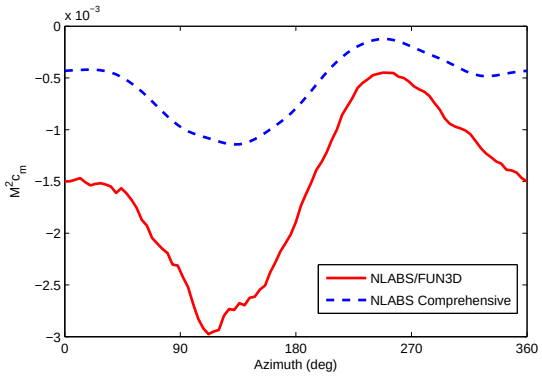

(a) 50%R

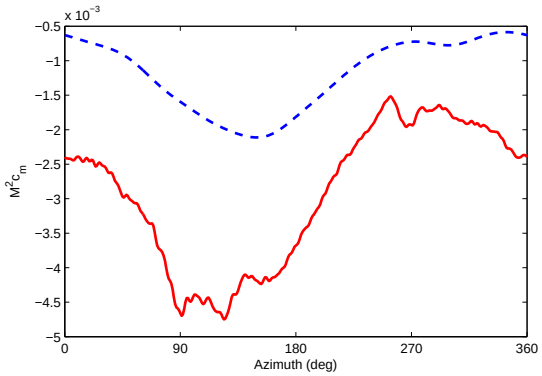

(b) 75%R

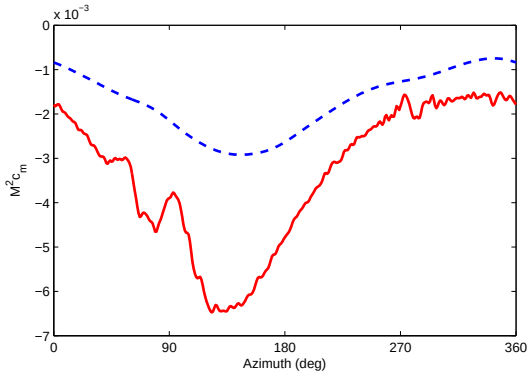

(c) 90%R

Figure 40: Pitching moment, M^2c_m, for F-S/NLABS and FUN3D/NLABS HART II baseline cases at $\mu = 0.25$ with $\alpha_s = -5.0$.

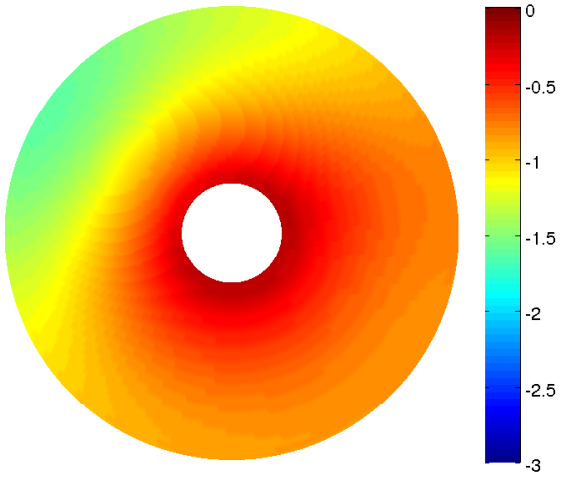

(a) F-S/NLABS

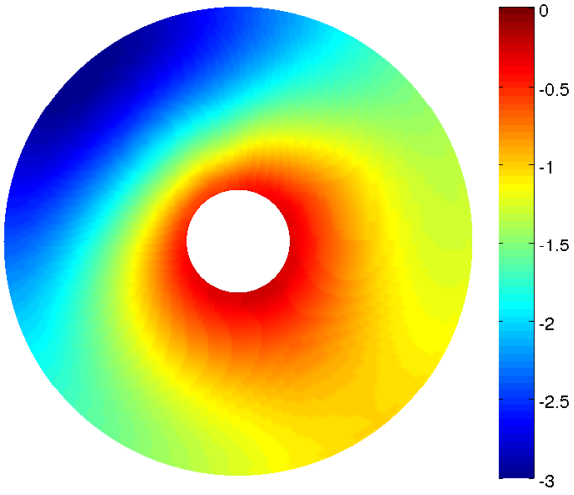

(b) FUN3D/NLABS

Figure 41: Elastic twist, deg, for F-S/NLABS and FUN3D/NLABS HART II baseline cases at $\mu = 0.25$ with $\alpha_s = -5.0$.

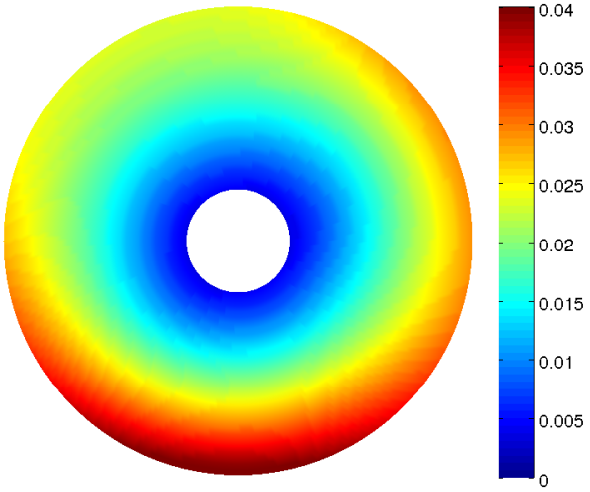

(a) F-S/NLABS

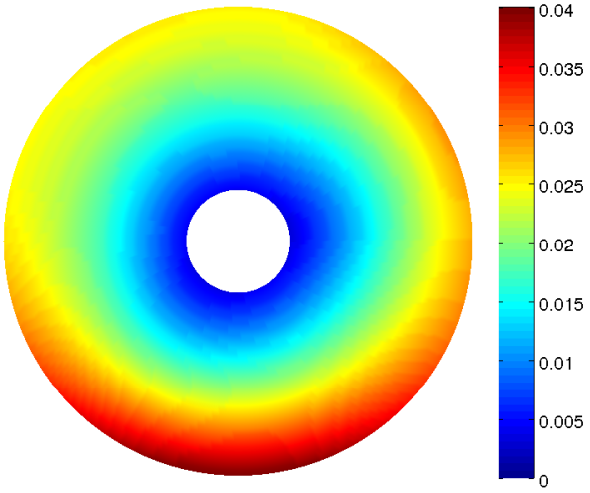

(b) FUN3D/NLABS

Figure 42: Vertical displacement, z/c, for F-S/NLABS and FUN3D/NLABS HART II baseline cases at $\mu = 0.25$ with $\alpha_s = -5.0$.

6.5 Rotor with Prescribed Parabolic Camber

A significant advantage of the FUN3D/NLABS aeroelastic methodology is that it allows arbitrary blade surface deformation to be modeled directly. Control input loads can also be prescribed, so that this capability can be applied for evaluation of camber actuation. To demonstrate this capability, the classic aeroelastic test case of an airfoil with parabolic camber centered at midchord (Fig. 43) is chosen. The nondimensionalized parabolic camber deflection can be expressed as $z/c = -a(x/c)^2$, where a is the amount of camber, x/c is the distance from the midchord, and z/c is the vertical distance from the chord to the camber line.

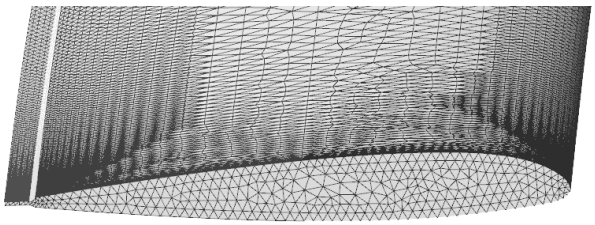

(a) Deformed blade without camber actuation

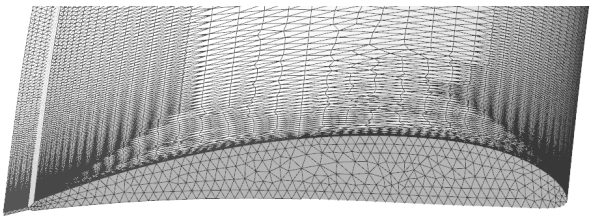

(b) Deformed blade with camber actuation

Figure 43: CFD surface mesh at blade tip demonstrating grid deformation with prescribed camber.

One of the primary objectives of camber actuation is to reduce hub loads. To confirm the potential benefits of camber actuation, camber actuation must produce a sufficient response to minimize vibratory loads. A set of CFD rotor simulations were computed, using the same conditions as the baseline HART II simulation, but with the inclusion of prescribed camber deformations. Camber deformation was achieved by assigning an arbitrarily high

camber stiffness and applying finite-section forces in NLABS. In this case, maximum camber deflections of 0.5%c ("full-camber") and 0.25%c ("half-camber") were imposed uniformly across the radius of the rotor, except near the root. Camber force was applied over time as a sinusoidal function with a frequency three times the rotational velocity of the rotor at various phase offsets of 0°, 90°, 180°, and 270° to examine the rotor response.

The trim solution changed very little for the prescribed-camber cases compared to the rigid-airfoil case in both finite-state and CFD aerodynamics (Table 10). For camber actuation of amplitude $0.005c$ the collective varied by $\pm 0.05°$, the lateral cyclic varied by $\pm 0.33°$, and the longitudinal cyclic varied by $\pm 0.39°$. The lack of change in collective trim indicates that the 3 per revolution camber deflections have very little impact on the mean thrust. Trends are similar for the comprehensive and CFD/CSD trim solutions as the phase of camber actuation is altered. In all cases, the CFD-based analysis resulted in a $0.32 - 0.37°$ increase in collective control, $0.19 - 0.326\circ$ decrease in lateral cyclic control, and $0.05 - 0.33°$ increase in longitudinal control compared to the finite-state-based analysis.

Table 10: Converged control settings for forward flight case.

	Controls	Rigid airfoil	0° phase	90° phase	180° phase	270° phase
Finite-state						
	θ_0, deg	10.19	10.22	10.14	10.15	10.22
	θ_{1c}, deg	0.86	0.96	0.53	0.73	1.18
	θ_{1s}, deg	-2.82	-2.93	-3.20	-2.68	-2.43
CFD						
	θ_0, deg	10.51	10.55	10.51	10.50	10.56
	θ_{1c}, deg	0.63	0.76	0.34	0.43	0.86
	θ_{1s}, deg	-2.55	-2.66	-2.87	-2.63	-2.38

The F-S/NLABS and FUN3D/NLABS sectional normal force responses to camber actuation are similar in phase and magnitude (here, the 0° phase lag is chosen as a representative case in Fig. 44). However, the influence of the tip vortex is not captured in the F-S/NLABS results, and as a result there is up to 25% difference in normal force at 75%R (Fig. 45) predicted by FUN3D/NLABS and F-S/NLABS near $\psi = 120°$, with 13° phase offset in the peak forces. On the retreating side of the rotor, there is much better agreement with a maximum of 7% difference in the instantaneous force and less than 7° phase difference in

the azimuth of force oscillations.

Pitching moments for the camber actuation case with 0° offset are next examined. When camber actuation is applied, the camber deflections generate large 3 per revolution oscillations in the pitching moment (Fig. 46). The average value of the pitching moment predictions by F-S are smaller than those of FUN3D by $\Delta(M^2 c_m) = 0.0018$ at $75\%R$ (Fig. 47). On the advancing side of the blade the NLABS pitching moment predictions (with mean removed) are within 9% of the FUN3D predictions. Near 120° the pitching moments deviate by as much as 55% due to the influence of the tip vortex on CFD loads. The azimuthal location of peak pitching moments are within 4° at all peaks.

Very little difference is observed in the FUN3D/NLABS and F-S/NLABS responses of elastic twist to camber actuation (Fig. 48). Local pitch values of a blade section at $75\%R$ differ by less than 7% at all azimuthal locations.

The aeroelastic response at $\frac{r}{R} = 75\%$, where $\frac{r}{R}$ is the non-dimensional local radius, is examined for the baseline case, half-camber actuation, and full-camber actuation with 0 degrees phase offset (Fig. 50). Although the direct response of normal force to camber actuation is small, the parabolic camber has a large influence on pitching moment (Fig. 50(a)). This causes an elastic twist deflection (Fig. 50(b)), which generates a large response in normal force (Fig. 50(c)). These results are consistent with results from Section 5.2 which indicate that small camber deflections have a large influence on pitching moment and blade deflection. Due to the significant coupling of camber and pitch modes, elastic twist amplifies the effects of camber actuation.

Figure 50 indicates that the response to camber actuation has a nearly linear relationship with the magnitude of the camber deflection, as the normal force coefficient of the half camber case can be approximated as

$$c_{n,half} \approx \frac{1}{2}(c_{n,full} + c_{n,baseline}) \tag{88}$$

within 10% accuracy at all azimuth locations.

The vibratory response to camber deformations is next evaluated to determine whether the magnitude of camber deflections is sufficient for minimizing vibratory loads. The results

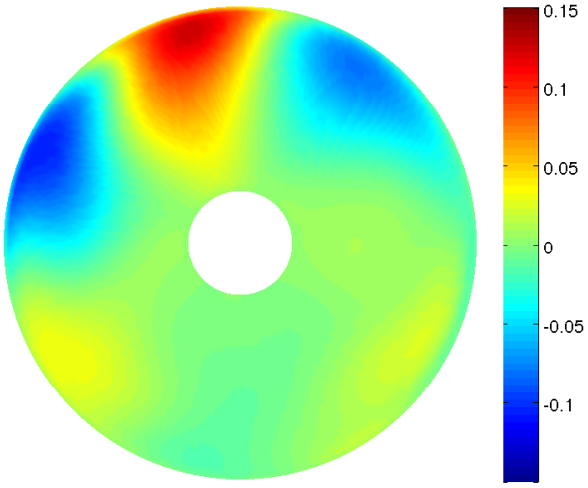

(a) F-S/NLABS

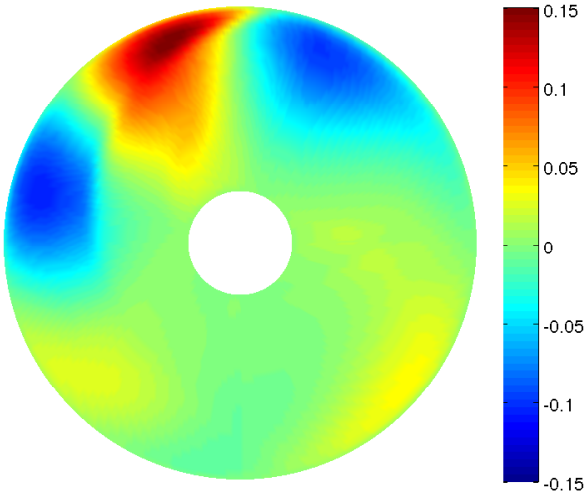

(b) FUN3D/NLABS

Figure 44: Delta in normal forces, $(M^2c_n)_{C0} - (M^2c_n)_{Base}$, for F-S/NLABS and FUN3D/NLABS HART II cases at $\mu = 0.25$ with $\alpha_s = -5.0$, where $C0$ indicates $0.5\%c$ prescribed camber deflection with 0° phase, and $Base$ indicates the baseline case (freestream is left to right).

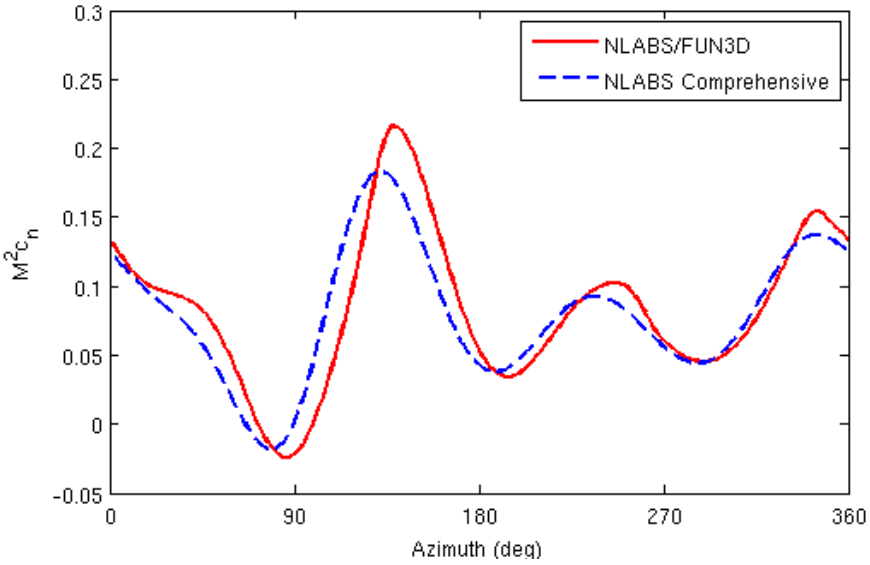

Figure 45: Sectional normal force with 3/rev camber actuation at 75%R, for F-S/NLABS and FUN3D/NLABS HART II cases at $\mu = 0.25$ with $\alpha_s = -5.0$; prescribed 0.5% camber deflection with 0° phase.

displayed in Fig. 51 indicate that a magnitude 0.25%c camber actuation at a frequency of 3 per revolution is sufficient for minimizing any of the forces or moments, as the origin falls within the outlined region of vibratory response. There is a significant offset in magnitude and phase of the CFD/CSD case compared to the finite-state case, and almost all force and moment responses predicted by FUN3D/NLABS are larger than the NLABS predictions. The comprehensive solution predicts a lower-magnitude response to camber actuation. Therefore, when determining the magnitude of camber forces and deflections that will be required to minimize hub loads, the F-S/NLABS solution provides a more conservative estimate.

6.6 Finite-State Rotor Inflow Analysis

In the forward flight simulations it was observed that the tip vortex only had an apparent influence on the FUN3D/NLABS normal force and pitching moment. In addition, there were significant differences in the magnitude and phase of vibratory hubloads. A study was conducted to determine the influence of the number of finite-state inflow modes on the distribution of normal force and pitching moment, particularly in the region of blade

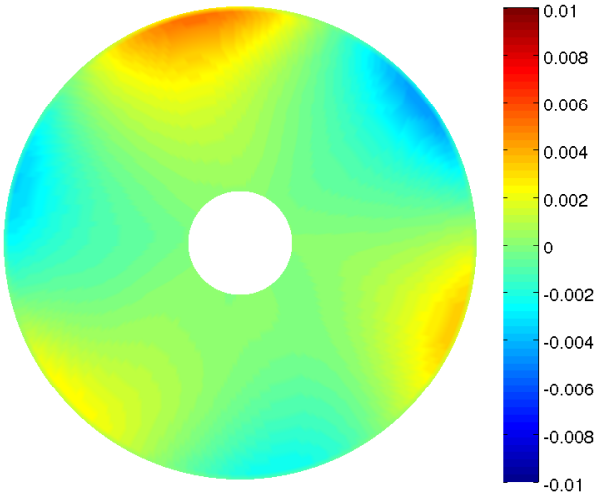

(a) F-S/NLABS

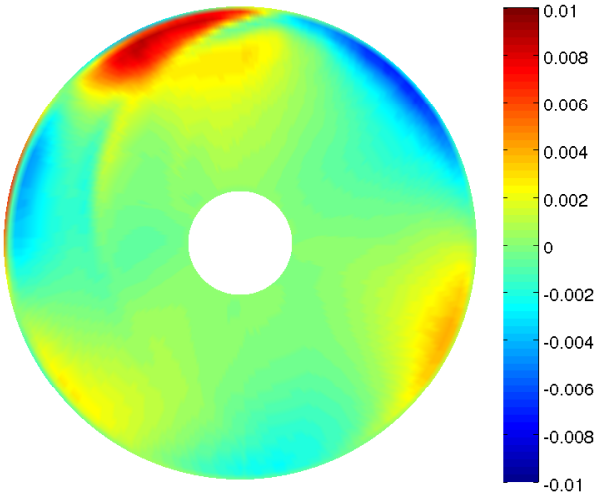

(b) FUN3D/NLABS

Figure 46: Delta in pitching moments, $(M^2 c_m)_{C0} - (M^2 c_m)_{Base}$, for F-S/NLABS and FUN3D/NLABS HART II cases at $\mu = 0.25$ with $\alpha_s = -5.0$, where $C0$ indicates $0.5\%c$ prescribed camber deflection with 0° phase, and $Base$ indicates the baseline case (freestream is left to right)).

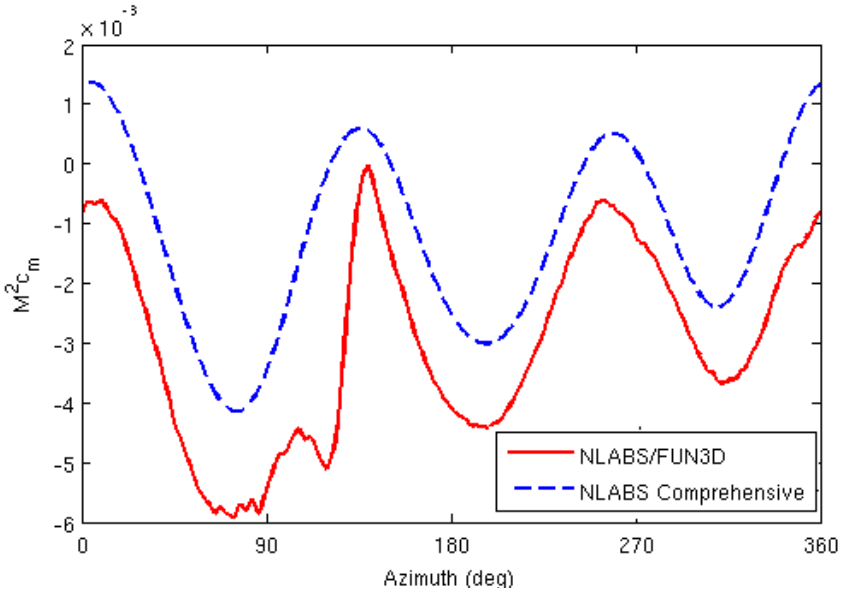

Figure 47: Sectional pitching moment with 3/rev camber actuation at $75\%R$, for F-S/NLABS and FUN3D/NLABS HART II cases at $\mu = 0.25$ with $\alpha_s = -5.0$; prescribed 0.5% camber deflection with 0° phase.

passage over the first tip vortex.

As previously discussed, the NLABS inflow model is the Peters and He finite-state model [124] (Eqs. 44, 45), in which several radial and azimuthal modes are used for approximating the induced inflow solution. In this case the number of radial and azimuthal shape functions were kept equal; otherwise radial oscillations in the normal loads appeared. In the azimuthal direction harmonic functions are used, while in the radial direction polynomials are applied. To determine the required number of finite-state modes, a study was conducted in which 8–24 modes were used in the baseline case, and 8–20 modes were used in cases with prescribed camber actuation of amplitude $0.5\%c$ and frequency 3 per revolution. Increasing the number of modes beyond these values resulted in numerical instability in the NLABS computations.

A qualitative comparison is first made in the normal force distribution and pitching moment distribution on the rotor disk. In Fig. 52 the difference in normal forces, $M^2(c_n^{CFD} - c_n^{CSD})$, demonstrates that the finite-state solution approaches the CFD solution as the number of states is increased. In particular, on the upwind side of the rotor the discontinuity in normal forces is better captured as the number of states increases. In addition, the difference in normal force outboard of $0.9R$ diminishes, and the finite-state

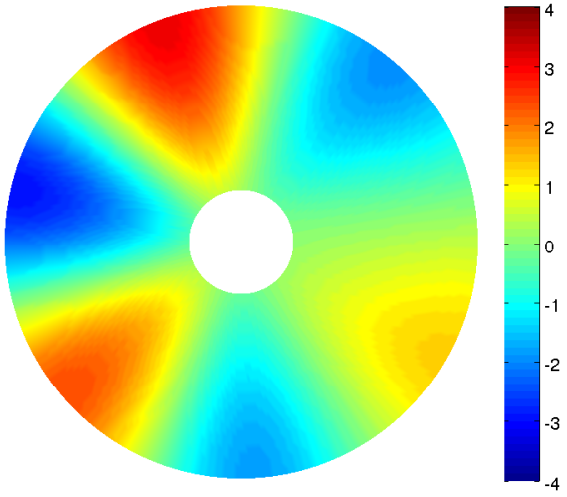

(a) F-S/NLABS

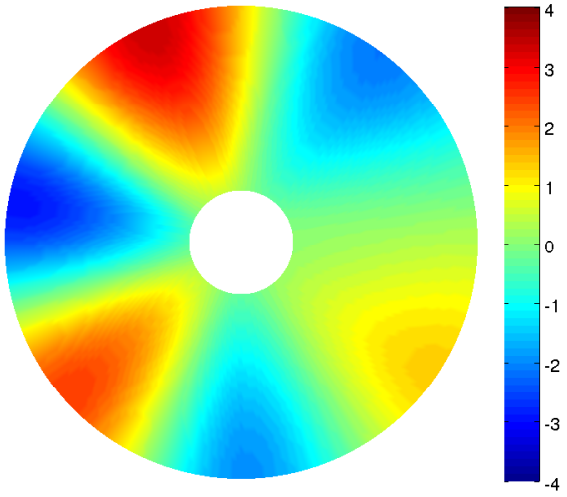

(b) FUN3D/NLABS

Figure 48: Delta in elastic twist, deg, $\theta_{C0} - \theta_{Base}$, for F-S/NLABS and FUN3D/NLABS HART II cases at $\mu = 0.25$ with $\alpha_s = -5.0$, where $C0$ indicates $0.5\%c$ prescribed camber deflection with 0° phase, and $Base$ indicates the baseline case (freestream is left to right).

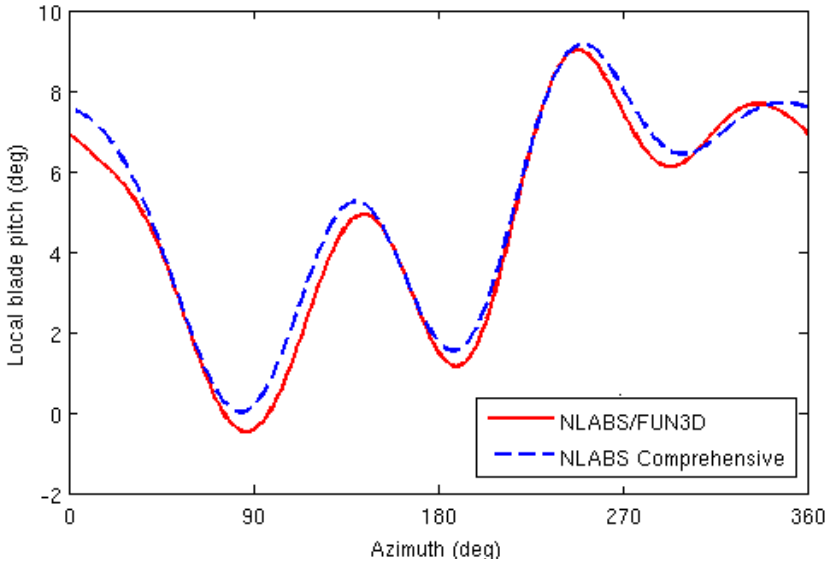

Figure 49: Local blade pitch with 3/rev camber actuation at 75%R, for F-S/NLABS and FUN3D/NLABS HART II cases at $\mu = 0.25$ with $\alpha_s = -5.0$; prescribed 0.5% camber deflections with 0° phase.

solution also approaches the CFD solution between 0° and 90° between $0.6R$ and $0.9R$. It is also observed, however, that when a large number of states is used (at least 20), radial oscillations in the normal force appear, and eventually the solution becomes unstable.

In examining the pitching moment, $M^2(c_{m,qc}^{CFD} - c_{m,qc}^{CSD})$, in Fig. 53, it is evident that the number of states in the inflow model does not improve the moment coefficient. The inflow model is unable to predict any influence of the wake vortices on pitching moment. While the influence of the tip vortex is relatively mild in this case, it indicates that the finite-state model is not suitable for cases in which significant wake interaction or blade-vortex interaction is expected. This observation is confirmed by the results of Smith et al. [147] in comparisons of the aeroelastic behavior of the HART II rotor in forward predicted by various computational methodologies, which included CFD and lifting line methodologies. At $\mu = 0.15$ with $\alpha_s = 5.3$, experimental measurements indicated large fluctuations in pitching moment were caused by blade-vortex interactions (BVI). CFD/CSD simulations were able to predict the unsteady pitching moments to varying levels of accuracy; however, when lifting-line aerodynamics had been applied, the fluctuations in pitching moment were absent during BVI events except in cases where the data was obtained from lookup tables.

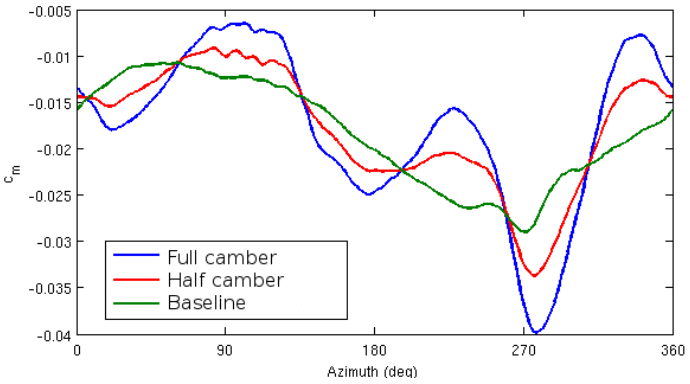

(a) Pitching moment coefficient

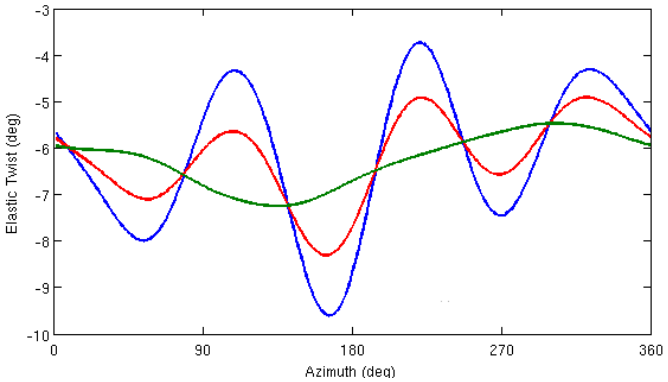

(b) Elastic twist

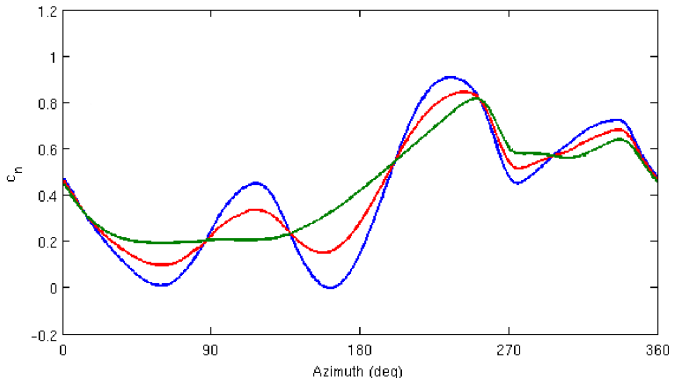

(c) Normal force coefficient

Figure 50: CFD/CSD blade pitch and aerodynamic response to camber actuation at $75\%R$ for HART II rotor at $\mu = 0.25$ with $\alpha_s = -5.0$; full camber indicates $0.5\%c$ deflections, and half camber indicates $0.25\%c$ deflections.

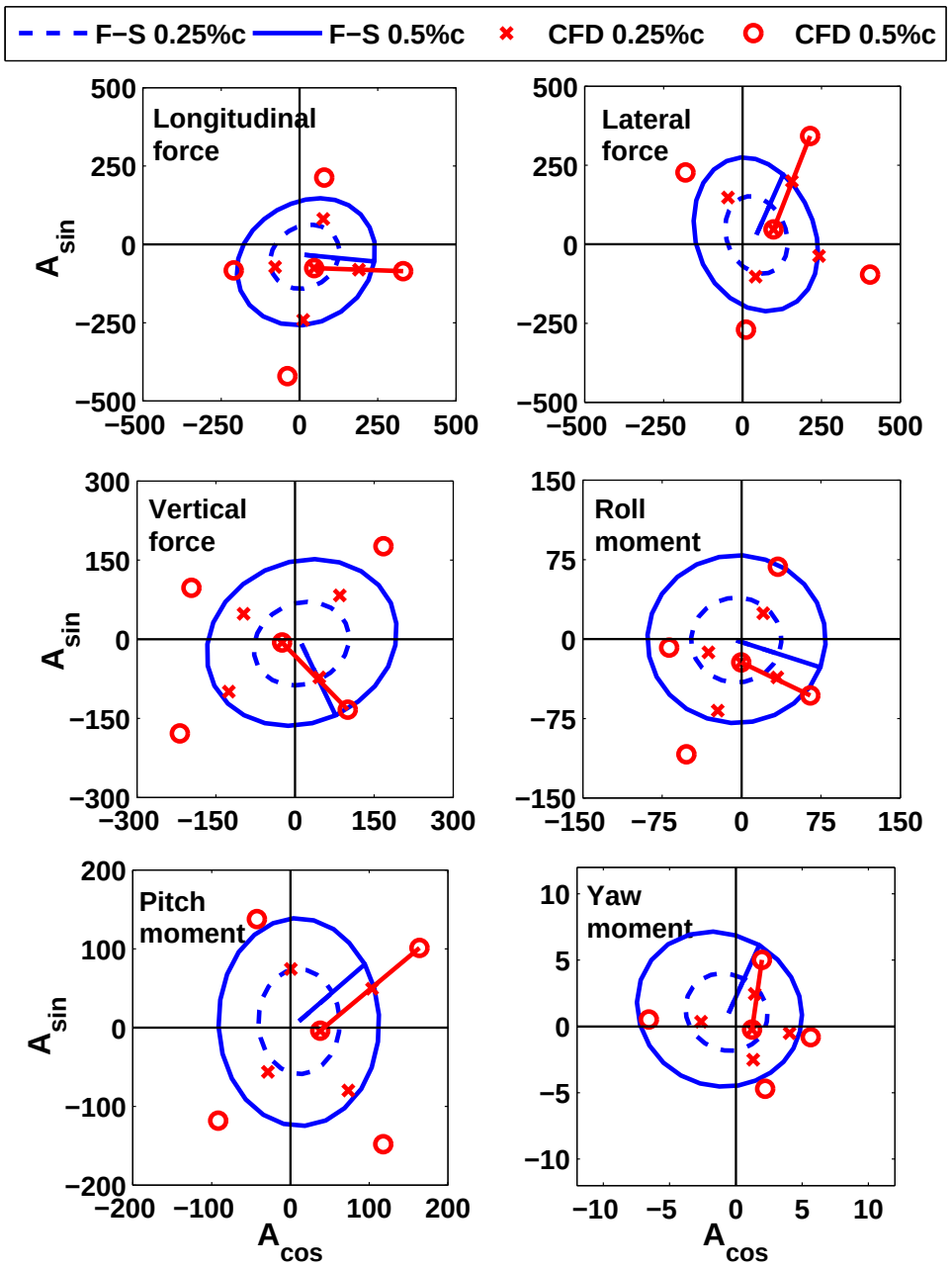

Figure 51: 4 per revolution vibratory load response to camber actuation for F-S/NLABS and FUN3D/NLABS HART II cases at $\mu = 0.25$ with $\alpha_s = -5.0$ with various phase and magnitude. $A_{\sin}$ and $A_{\cos}$ refer to the Fourier coefficients such that the 4 per revolution loads can be written as $F_4 = A_{\sin} \sin 4\Psi + A_{\cos} \cos 4\Psi$. Lines from the center to the outer curve/point indicate 0° phase of camber actuation.

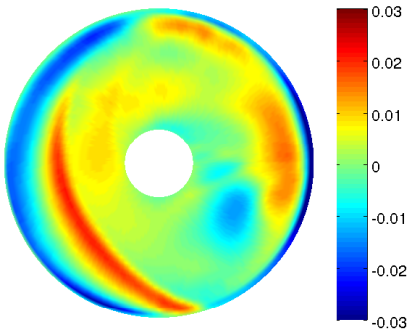

(a) 8 harmonics

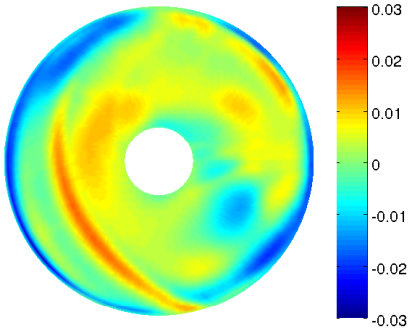

(b) 12 harmonics

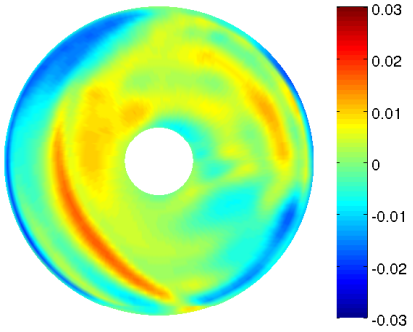

(c) 16 harmonics

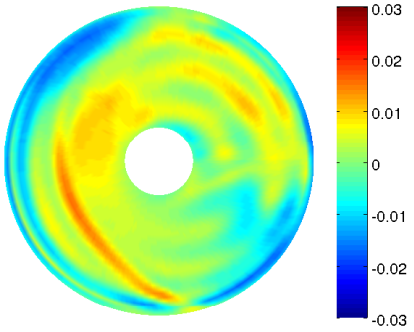

(d) 20 harmonics

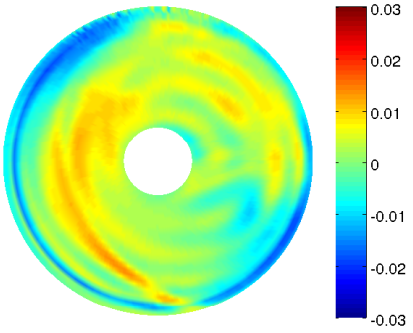

(e) 24 harmonics

Figure 52: Delta in normal forces, $M^2(c_n^{CFD} - c_n^{CFD})$, for F-S/NLABS and FUN3D/NLABS HART II baseline cases at $\mu = 0.25$ with $\alpha_s = -5.0$ with various number of rotor inflow modes.

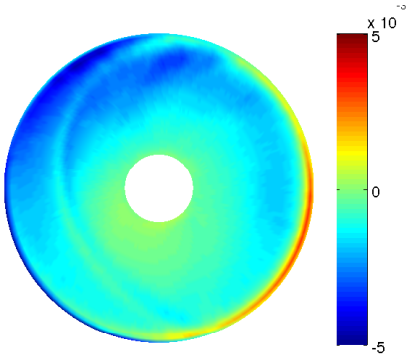

(a) 8 harmonics

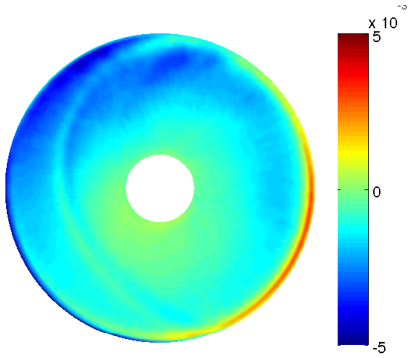

(b) 12 harmonics

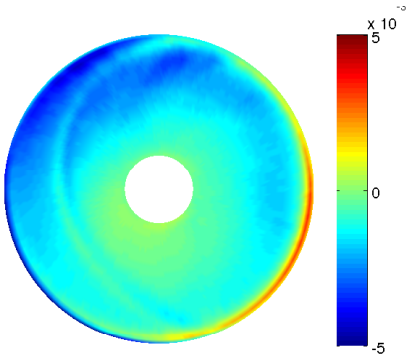

(c) 16 harmonics

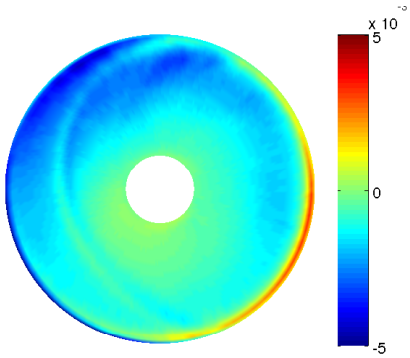

(d) 20 harmonics

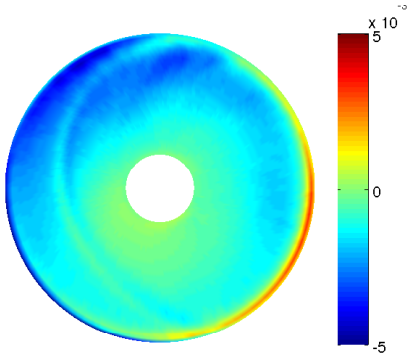

(e) 24 harmonics

Figure 53: Delta in pitching moments, $M^2(c_{m,qc}^{CFD} - c_{m,qc}^{CSD})$, for F-S/NLABS and FUN3D/NLABS HART II baseline cases at $\mu = 0.25$ with $\alpha_s = -5.0$ with various number of rotor inflow modes.

As the distribution of normal loads predicted by the finite-state model approaches that of the CFD model, the hubloads of the comprehensive analysis also approach that of the CFD/CSD simulations (Fig. 54). With only 8 harmonics the comprehensive loads under predict the peak forces and moments for F_x, F_y, F_z, M_x, and M_y (where z is aligned in the shaft axis). The vertical force F_z and roll moment M_x are not only predicted to have lower amplitudes, but also large phase offsets in comparison to the CFD/CSD loads. There is a large offset between the CFD/CSD and comprehensive yaw moment M_z which is because only pressure loads are communicated from the CFD solver. As the number of harmonics is increased, the phase improves for F_z, M_x, and M_z, and the peak values of F_x, F_y, and M_y approach those of the CFD/CSD analysis.

A case with prescribed camber actuation of amplitude $0.005c$, frequency 3 per revolution, and phase offset of 0° is next analyzed. Figure 55 illustrates that as the number of harmonics is increased, the peak values of F_x, F_y, and M_y approach those of the FUN3D/NLABS simulation.

Finally, the change in vibratory loads is quantified in terms of magnitude and phase of the 4 and 8 per revolution hubloads; these are the frequencies at which the largest magnitude vibratory loads occur. In this analysis the change in loads for the rigid-airfoil case is defined as

$$\Delta F_{i,rigid} = (F^{CSD}_{i,rigid} - F^{CFD}_{i,rigid})/F^{CFD}_{i,rigid}. \tag{89}$$

For the cases with prescribed camber only the response to camber deflections is compared:

$$\Delta F_{i,camber} = \left[(F^{CSD}_{i,camber} - F^{CSD}_{i,rigid}) - (F^{CFD}_{i,camber} - F^{CFD}_{i,rigid})\right] / (F^{CFD}_{i,camber} - F^{CFD}_{i,rigid}). \tag{90}$$

In this manner the change in loads due to camber response is isolated from the other loads. In Fig. 56 significant improvements are observed in the magnitude of 4 per revolution vibratory loads F_x, F_y, M_x, and M_y for the rigid airfoil case. However, the magnitude of vertical force F_z and yaw moment M_z deviate further from the CFD/CSD solution as the number of finite-state harmonics is increased. Little or no improvement is observed in the magnitude of vibratory load response to camber deflections. In comparing the phase offset of 4 per revolution vibratory loads, increasing the number of states significantly improves

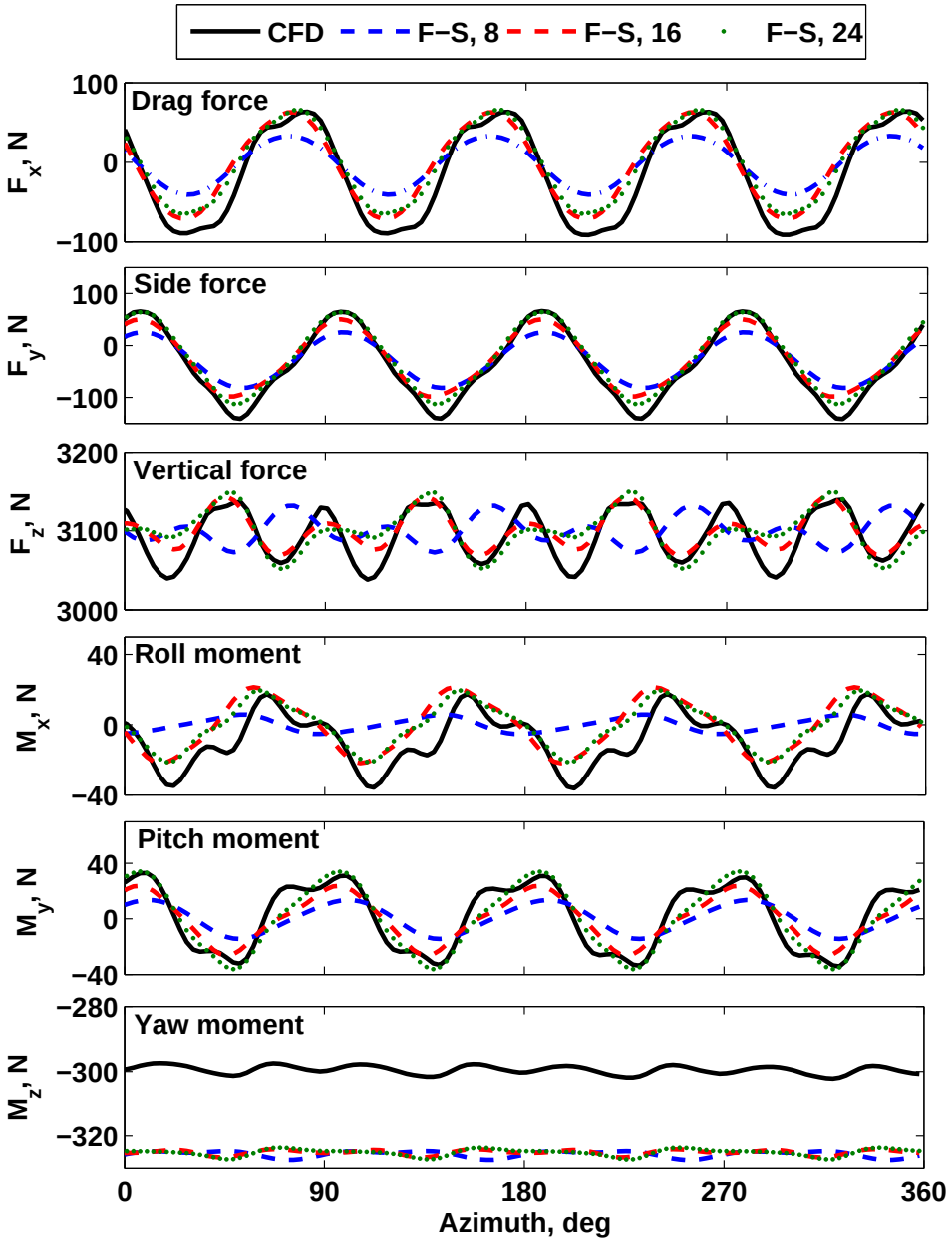

Figure 54: Forces and moments for F-S/NLABS and FUN3D/NLABS HART II baseline cases at $\mu = 0.25$ with $\alpha_s = -5.0$; legend indicates number of finite-state modes.

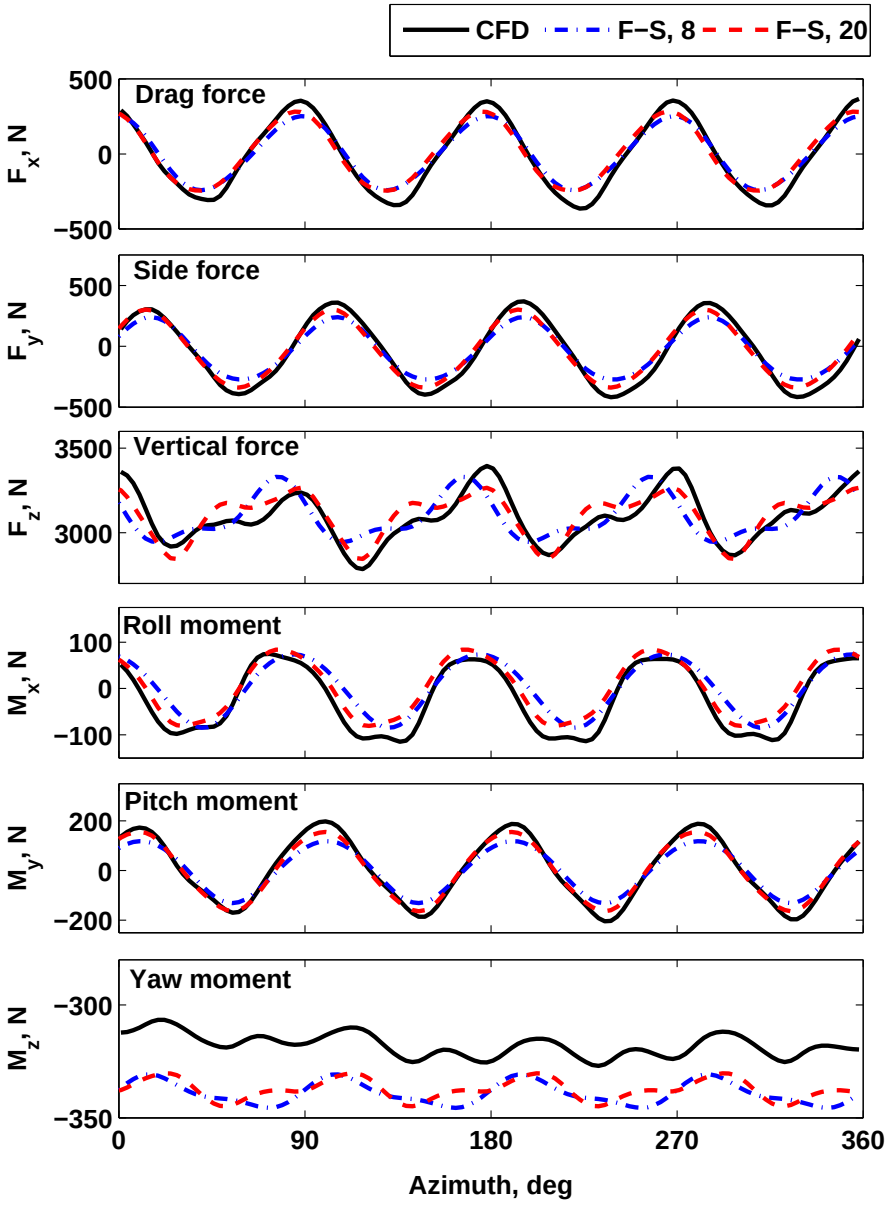

Figure 55: F-S/NLABS and FUN3D/NLABS forces and moments for HART II rotor case with 0° phase, $0.005c$ magnitude prescribed camber oscillations at frequency 3 per revolution; legend indicates number of finite-state modes.

agreement with CFD/CSD results in the baseline case except for the drag force F_x. For all other forces and moments the phase improves until reaching 16 harmonics, after which there is little change in phase. In the prescribed camber cases there is little or no improvement in phase as the number of states is increased.

In examining the magnitude of 8 per revolution vibratory loads (Fig. 58) there is no consistent improvement in finite-state loads as the number of states is increased. However, the phase of almost all forces and moments improve with increased number of states for both the baseline case and the prescribed camber responses. In particular, the normal forces consistently approach those of CFD/CSD loads for all cases. Initially there are $-81°$ to $-151°$ phase offsets in 8 per revolution normal loads, which are reduced to $16°$ to $-87°$ phase offsets as the number of finite-state harmonics is increased.

It has been observed that 8 finite-state harmonics are not sufficient to capture the wake features or accurately predict vibratory loads. Although there are still discrepancies in magnitude and phase as the number of harmonics is increased, the solution begins to approach those of the CFD/CSD results from a qualitative and quantitative perspective. However, increasing the number of harmonics beyond 20–24 may result in numerical instability. Based on these results it is recommended that 16–20 finite-state harmonics be used to more accurately resolve the wake and hub loads while remaining in a numerically stable range.

6.7 Computational Cost

By increasing the number of finite-state harmonics in the comprehensive analysis more accurate agreement with CFD/CSD predictions is reached. If the comprehensive analysis can be applied predominantly in the design of actuation systems, then computational cost can be greatly reduced. One time step of the CFD analysis for a 13.2 million node grid on128 Cray XT5 2.3GHz Opteron processors requires 1 minute and 32 seconds of wall clock time. In a CFD/CSD simulation hole-cutting and computation of domain connectivity information must be computed at every time step, as well as the application of a grid deformation process. The total time required for one time step of a CFD/CSD rotor simulation is 3

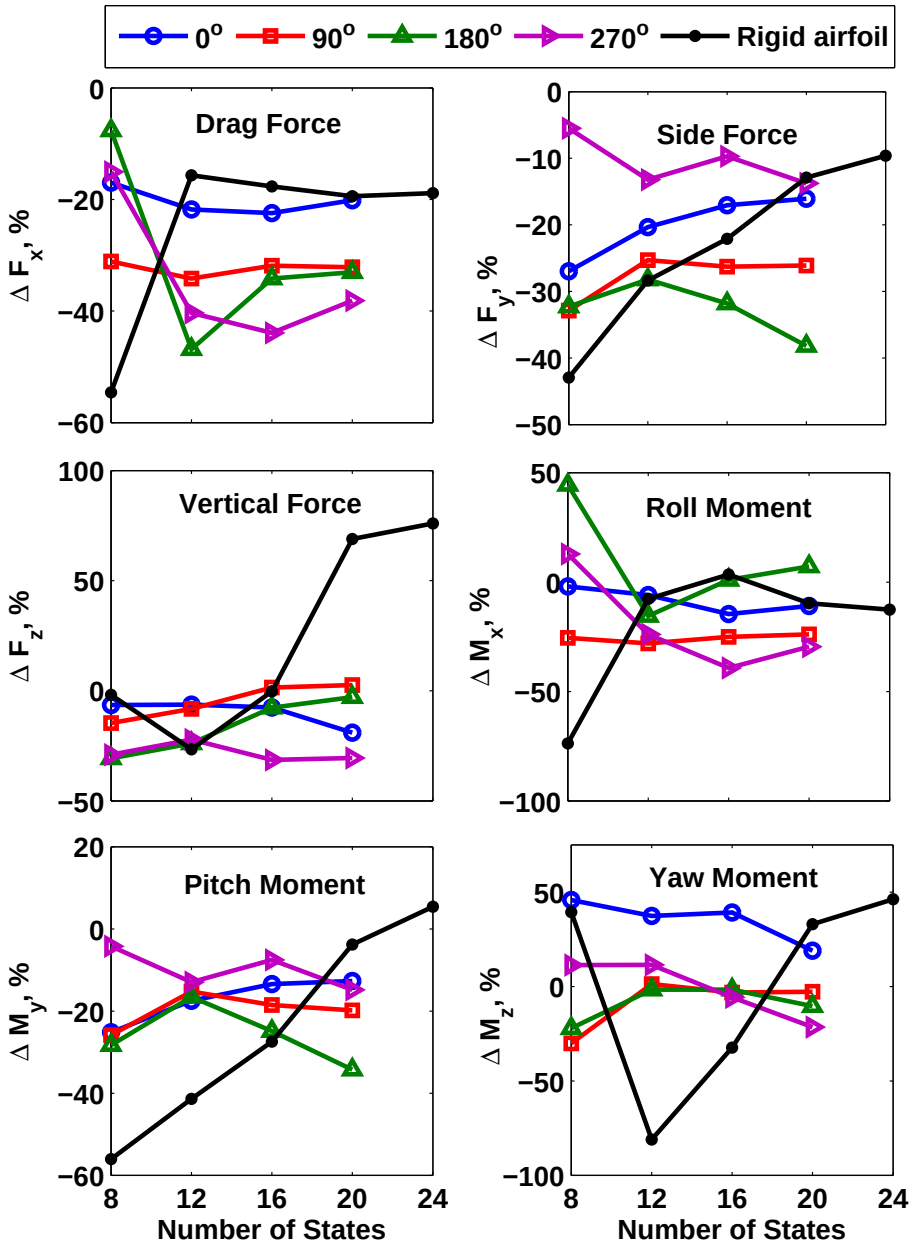

Figure 56: Magnitude response of F-S/NLABS 4 per revolution vibratory loads for HART II rotor with various number of finite-state harmonics with respect to FUN3D/NLABS results; phase of prescribed camber indicated in legend.

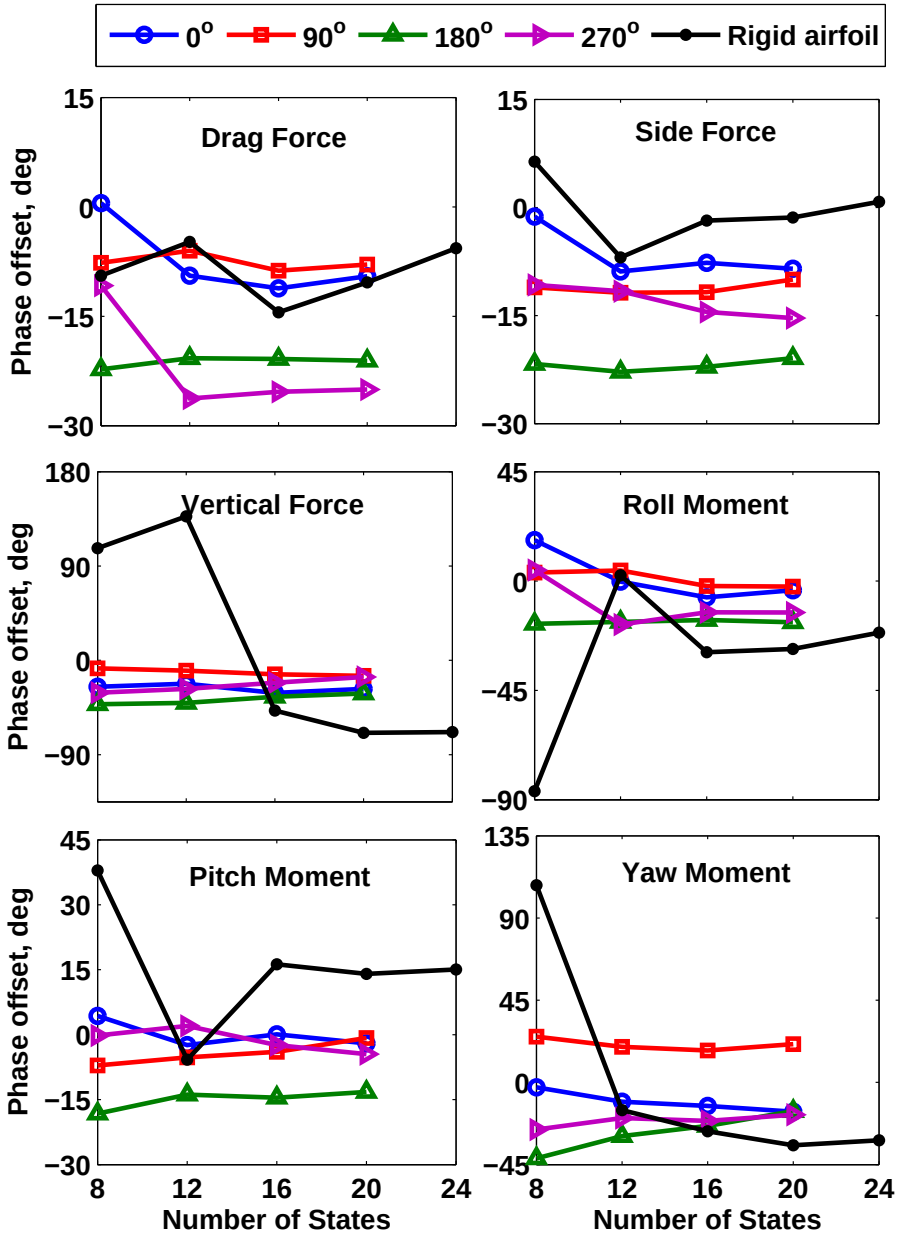

Figure 57: Phase response of F-S/NLABS 4 per revolution vibratory loads for HART II rotor with various number of finite-state harmonics with respect to FUN3D/NLABS results; phase of prescribed camber indicated in legend.

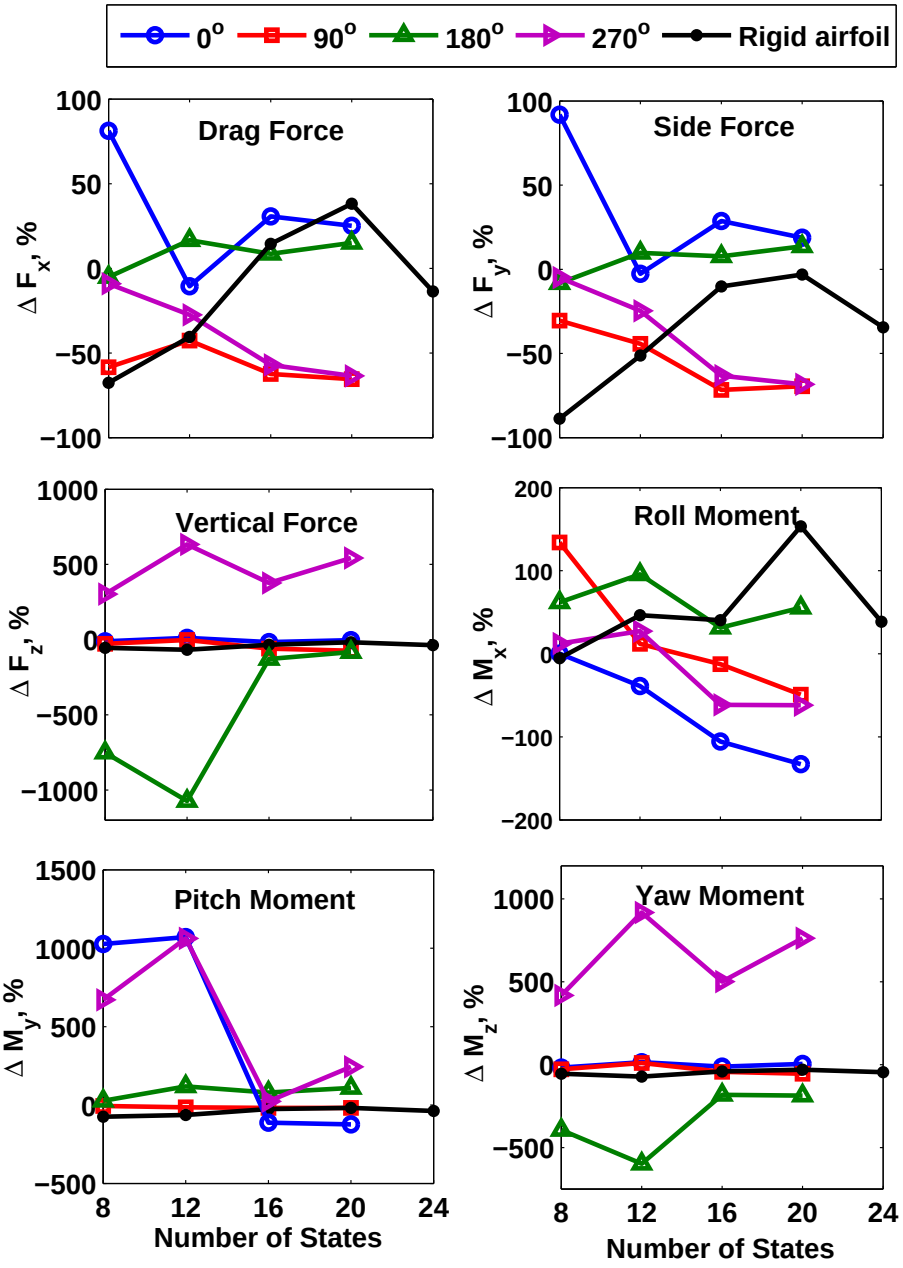

Figure 58: Magnitude response of F-S/NLABS 8 per revolution vibratory loads for HART II rotor with various number of finite-state harmonics with respect to FUN3D/NLABS results; phase of prescribed camber indicated in legend.

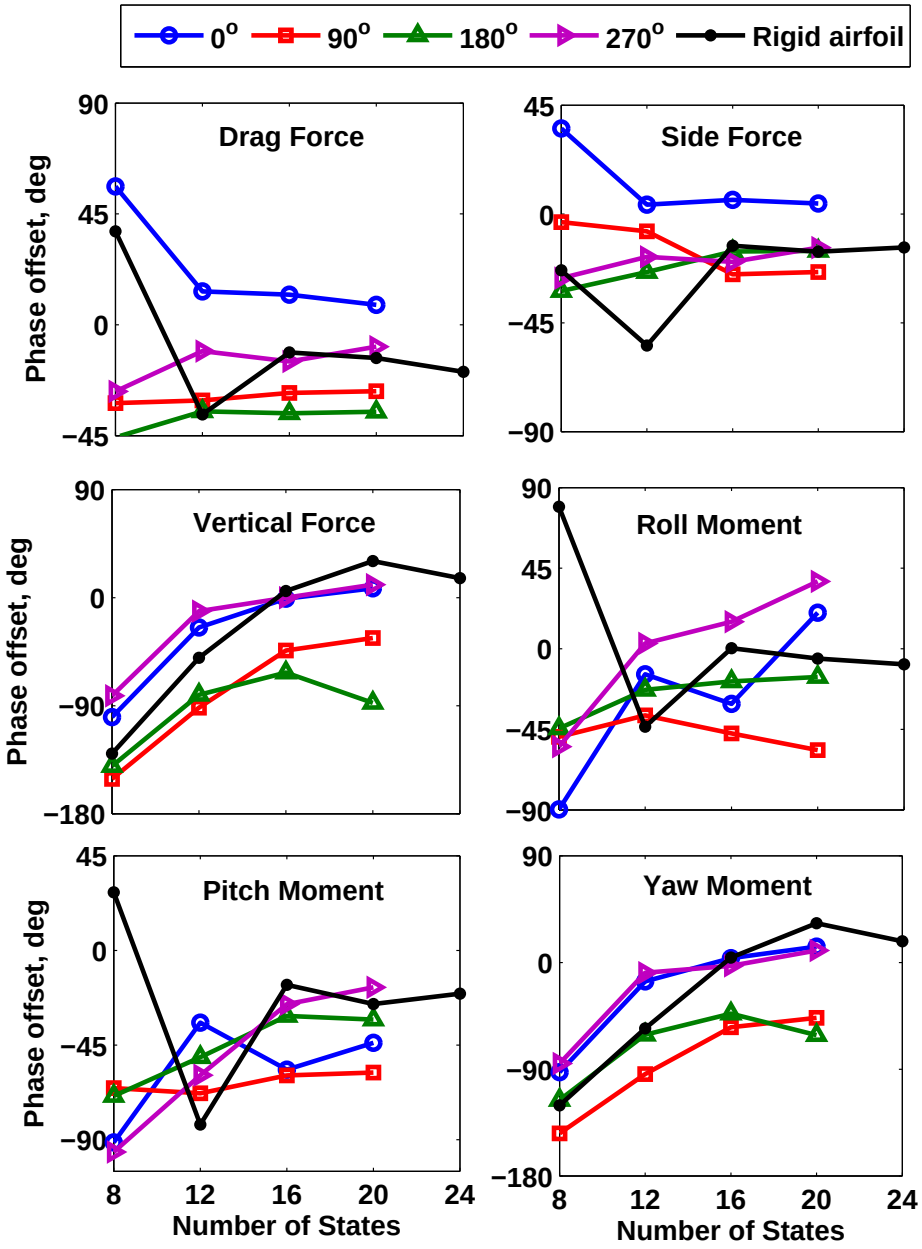

Figure 59: Phase response of F-S/NLABS 8 per revolution vibratory loads for HART II rotor with various number of finite-state harmonics with respect to FUN3D/NLABS results; phase of prescribed camber indicated in legend.

minutes and 20 seconds, which is equivalent to 7.1 central processing unit (CPU) hours when 128 processors are used.

The comprehensive analysis requires only 2.1 seconds per time step, which is two orders of magnitude less wall time and four order of magnitude less total CPU hours if approximately 1×10^2 processors are used. Therefore, efforts to improve the finite-state model and apply it when appropriate can greatly improve the computational efficiency of an aeroelastic analysis.

CHAPTER VII

COMPUTATIONAL EVALUATION OF THE INFLUENCE OF A TEST FACILITY

Simulations are next performed for the HOTIS configuration [120, 143], in which a scaled BO-105 rotor operates inside an enclosed facility to determine if performance characteristics and vibratory loads can be accurately evaluated for a rotor inside a test facility. The effects of various turbulence models, including Menter SST, HRLES, and HRLES with LDKM, are compared in this study. The influence of geometry fidelity throughout the test facility is also analyzed.

7.1 Configuration and Flight Conditions

The HOTIS test [120, 143] is an experiment performed in 2006 for a rotor in hover inside an enclosed facility. In this experiment the rotor was nearly centered in a $6R \times 6R \times 4R$ (width $\times$ length $\times$ height) room, and the rotor plane was $1.43R$ above the ground (Fig. 60). The rotor was a 40% scaled BO-105 rotor with four blades, which is the same rotor (Table 2) that was used in the HART II tests, with a pre-cone angle of 2.5°. The HOTIS test was performed at the rotational velocity $\Omega = 109$ rad/s to obtain a tip Mach number of 0.633. Data were obtained at various levels of thrust, ranging from $C_T = 0.0$ to $C_T = 5.5 \times 10^{-3}$, at collective pitch angles up to 8° with reference to the $70\%R$, using force transducers and a torque meter in the test rig to measure the forces and moments at the hub. In the computational analysis simulations are run with a collective pitch of 8° for comparison to experimental data.

The same blade grids (Table 4) that were applied previously in the forward flight rotor cases were used in the HOTIS simulations. A grid spacing of $1\%c$ was applied near the rotor in the background farfield and test facility grids, and adaptive mesh refinement was applied to better resolve tip vortices and root vortices. A study of the effects of temporal resolution revealed that there was less than 2% difference between the C_T and C_P computed using

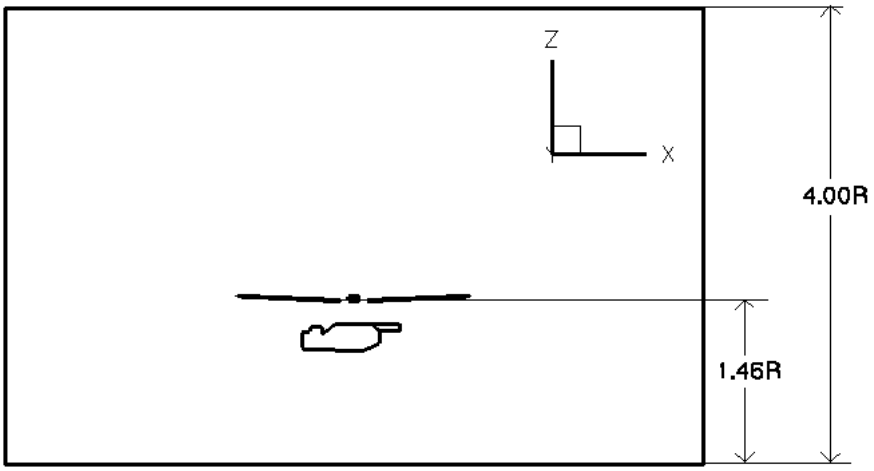

(a) Side view

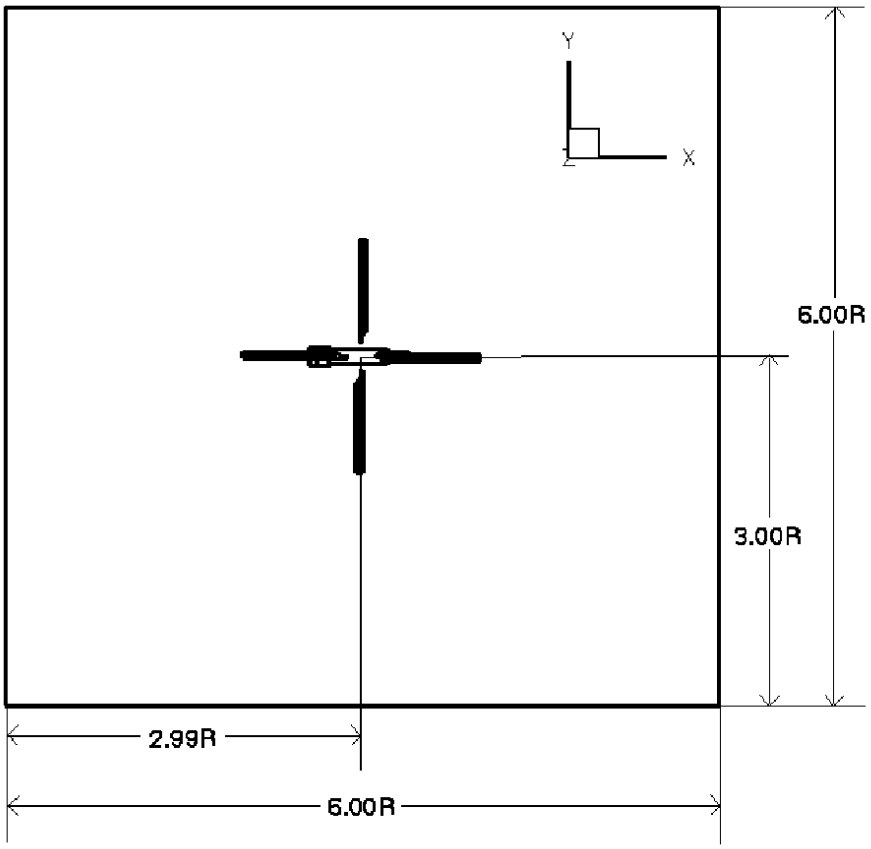

(b) Top view

Figure 60: Dimensions of the HOTIS test facility.

0.5° time steps compared to 1° steps. Time steps of 3° result in an over prediction of torque by 30% and therefore are not appropriate for performance predictions. However, there was little difference in thrust (2%) when using 3° steps, indicating that the momentum added by the rotor is nearly equivalent when 1° steps are used. Therefore, 3° steps were first applied until approaching convergence to reduce computational expense induced by the long-term wake effects. Subsequently 1° steps were used for performance metric predictions.

7.2 Results

The test facility walls were initially modeled with inviscid boundary conditions, and the Menter SST turbulence model with vorticity-based turbulence production was applied. A region of "false convergence" was reached within about 6-8 rotor revolutions, where the thrust and power coefficients reached plateaus (Fig. 61). After 15 revolutions the first two tip vortices were still similar in magnitude and displacement, comparing the free air and test facility cases (Fig. 63). However, in the test facility case at 27 revolutions the tip vortices moved downward and radially outward, and by the 39th revolution the tip vortices traveled nearly straight down and quickly dissipated. The movement of the tip vortices was caused by an increasing induced velocity through the rotor disk, while the dissipation was due to an over-predicted eddy viscosity as the wake circulated throughout the facility (Fig. 64). Thrust began to decrease due to a smaller effective angle of attack and the shifted location of the tip vortex. As the inflow velocity decreases between 39 and 72 revolutions (Fig. 64) the thrust increases again. Between 72 and 150 revolutions the wake vortices shift downward (Fig. 65), altering the inflow velocity (Fig. 64) and again increasing thrust (Fig. 61). However, figure of merit was still under predicted by 27% (Table 11, Fig. 66). The HOTIS facility simulation required more than 100 rotor revolutions to achieve convergence, compared to approximately 12 required by the free-air hover simulation. Further analysis was performed to determine in more detail the effects of the test facility.

As the wake began to recirculate, the loading near the blade tip was first affected as the tip vortices dissipated (Fig. 67). An increase in induced flow through the rotor plane moved the tip vortices downward at a higher rate and further outboard. As a result, the

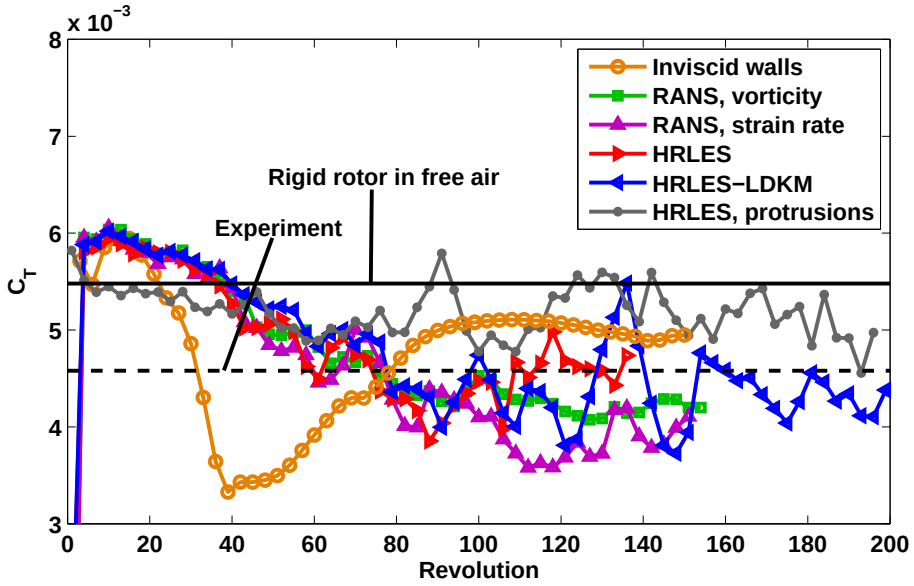

Figure 61: Thrust history for the HOTIS rotor computations at $\Omega R = 0.64$ and at collection pitch 8.0°$collectivepitch$.

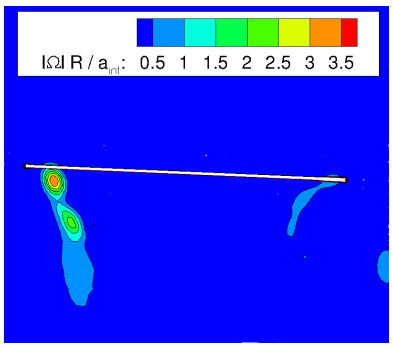

Figure 62: Vorticity contours for the HOTIS rotor in free air.

Table 11: Time-Averaged Converged Performance Results.

	C_T ×1000	C_T Error	FM	FM Error
8.0° Collective Pitch				
Experiment	4.58	–	0.604	–
Free air	5.48	19.7%	0.576	-4.6%
Menter SST, inviscid walls	5.02	9.6%	0.443	-26.7%
Menter SST, vorticity-based	4.21	-8.0%	0.404	-33.1%
Menter SST, strain-rate-based	3.85	-16.0%	0.356	-41.1%
HRLES	4.44	-3.0%	0.424	-29.7%
HRLES with LDKM	4.35	-5.0%	0.436	-27.8%
HRLES with protrusions	5.15	12.4%	0.531	-12.1%
8.3° Collective Pitch				
Experiment	4.77	–	0.597	–
Free air, elastic	4.54	-4.8%	0.567	-5.0%

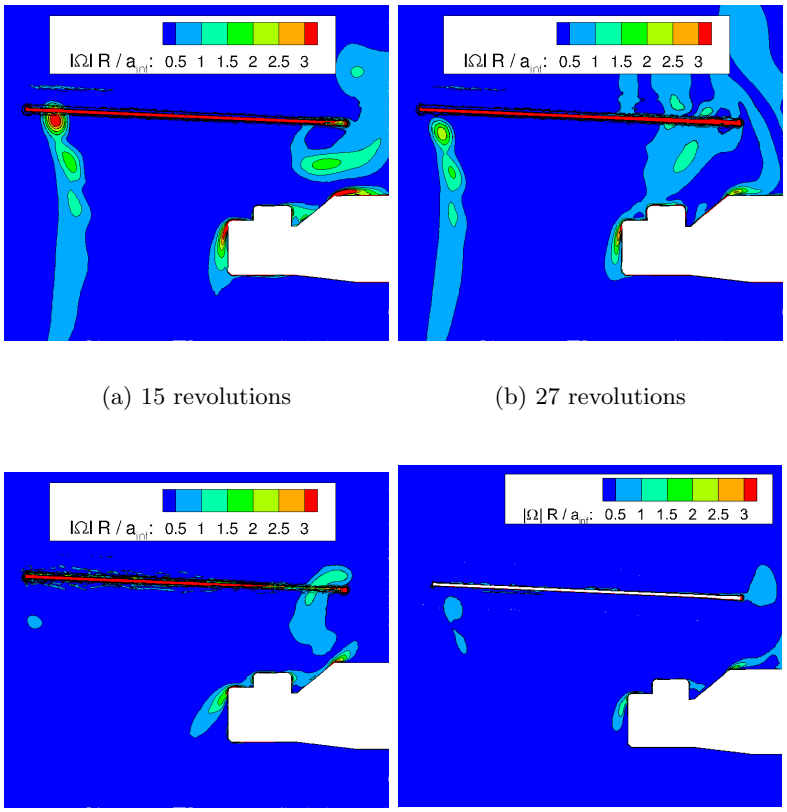

(a) 15 revolutions (b) 27 revolutions

(c) 39 revolutions (d) 150 revolutions

Figure 63: Vorticity contours for the HOTIS rotor in a facility with inviscid walls.

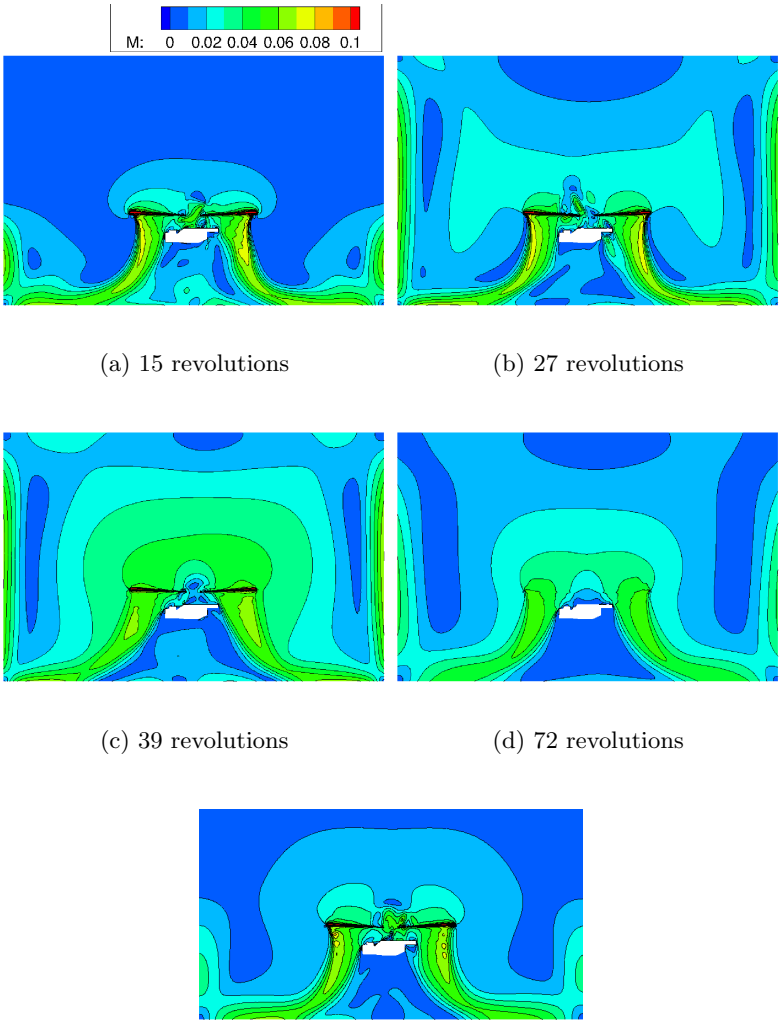

(a) 15 revolutions

(b) 27 revolutions

(c) 39 revolutions

(d) 72 revolutions

(e) 150 revolutions

Figure 64: Mach contours for the HOTIS rotor in a facility with inviscid walls.

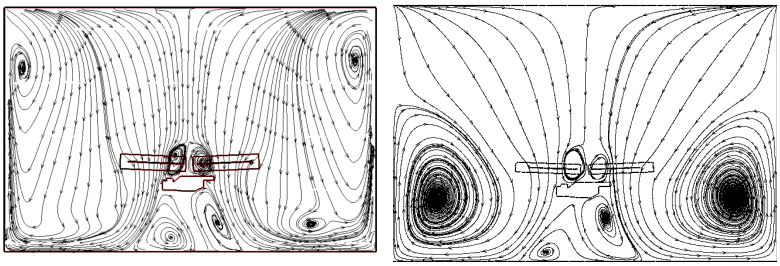

(a) 72 revolutions (b) 150 revolutions

Figure 65: Vorticity contours for rotor in facility with inviscid walls.

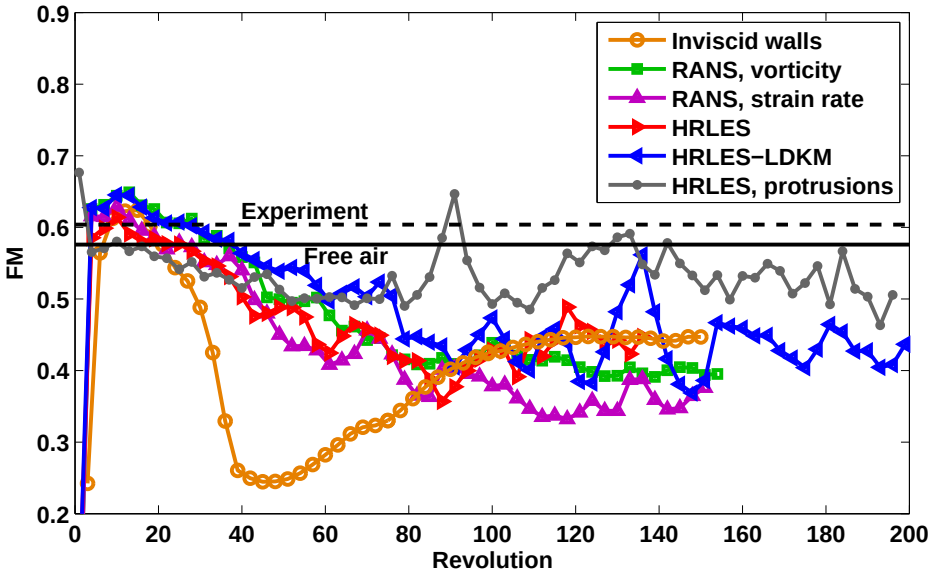

Figure 66: Figure of merit history for HOTIS cases with viscous facility walls at $\Omega R = 0.64$ and at collection pitch $8.0°collectivepitch$.

loading was decreased near the blade tip. As the fountain flow increased the inflow velocity through the rotor plane, the loads over the entire blade were reduced due to a decrease in effective angle of attack. As inflow velocity began to decrease again the effective angle of attack increased, and blade loads began to increase again.

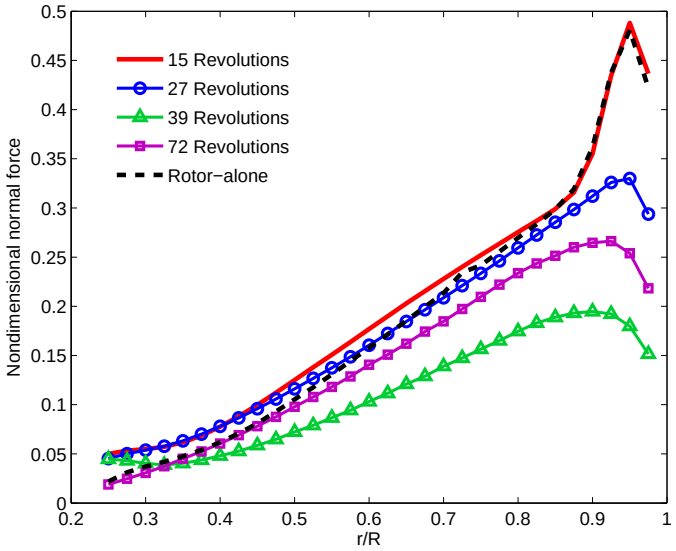

Figure 67: Radial normal force distribution (non-dimensionalized by blade-tip dynamic pressure) of the HOTIS rotor inside a facility at $\Omega R = 0.64$ and at collection pitch $7.6°collective pitch$.

To determine the influence of turbulence model on the flow characteristics, eddy viscosity was examined on a vertical plane through the center of the rotor (Fig. 68). As the wake moved along the walls the eddy viscosity began to reach non-physical values as large as μ_t/μ =270,000. The extremely large values of eddy viscosity caused the wake vortices to generate large regions of rotational flow which caused the increased values of induced velocity. After the recirculation vortices shifted toward the floor, eddy viscosity decreased to some extent, but maximum values of $\mu_t/\mu =$ remained near 100,000 (Fig. 68), and as a result tip vortices were still greatly dissipated (Fig. 63(d)).

These results indicate that nonphysical turbulence properties are generated when the inviscid boundary condition is applied to the test facility walls and the Menter SST turbulence model is applied. Because turbulence properties in the Menter SST model are dependent on

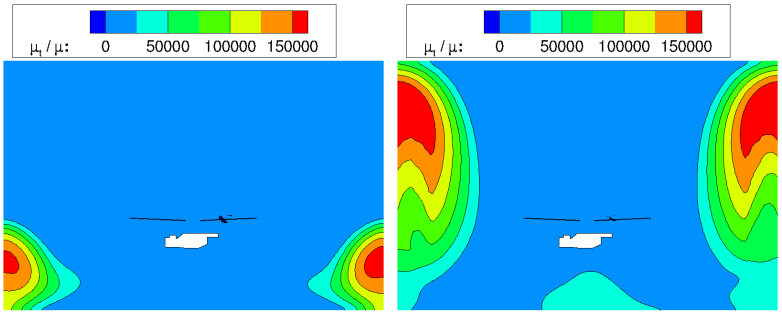

(a) 15 revolutions (b) 27 revolutions

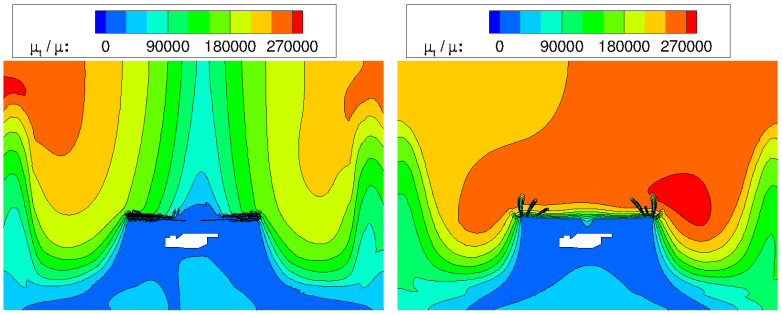

(c) 39 revolutions (d) 72 revolutions

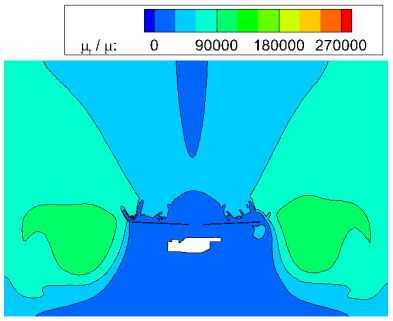

(e) 150 revolutions

Figure 68: Eddy viscosity contours for the HOTIS rotor in a facility with inviscid walls. The scale varies to show levels at different times.

distance from the nearest viscous surface, the boundary condition on test facility walls has a significant effect on the flowfield solution. Hunt [156] and Spalart [80] both indicate that in general URANS models are appropriate only in thin shear layers, and do not accurately model turbulence outside the boundary layer. In a closed volume the turbulent wake of the rotor recirculates through the rotor plane, and thus inaccurate turbulence modeling can greatly impact rotor performance. Since URANS models typically rely on a dependence to wall distance, it is more appropriate to select a turbulence model such as the HRLES model, in which the URANS equations are applied near viscous surfaces, while LES equations are applied elsewhere.

7.2.1 Influence of Turbulence Model

To more accurately model the turbulence in the wake region the baseline HRLES and HRLES-LDKM models were applied. In URANS turbulence models it may be more accurate to calculate turbulence production based on the strain rate, rather than vorticity, which is the convention in many models [80]. Therefore, four test cases with viscous test facility walls were evaluated; each case was identical except for the turbulence model. The turbulence models applied in theses cases were the vorticity-based Menter SST, strain-rate Menter SST, HRLES, and HRLES with LDKM.

The trends of thrust and figure of merit are very similar for all cases (Figs. 61, 66). In comparison with experimental data of van der Wall and Richard [120], thrust is initially over predicted by up to 27%, and figure of merit is over predicted by 0-11%. The difference in thrust is expected, since it was determined that the elastic effects, which are not included in these simulations, decrease thrust. Due to ground effects thrust and figure of merit are also larger than the predicted free-air values. At twenty to thirty revolutions both thrust and figure of merit gradually decline due to the influence of wake recirculation. At 50 revolutions the thrust and figure of merit temporarily plateau. However, at 60 revolutions the thrust and figure of merit again begin to decrease, and becomes more unsteady in nature. By 100 revolutions the figure of merit is greatly under predicted in all four viscous-wall simulations (Fig. 66, Table 11). In some cases the thrust is well predicted, but this is spurious; an

increase in thrust due to a lack of modeled blade twist is canceled by a decrease in thrust due to recirculation.

To determine why thrust predictions decrease as the simulation time increases, the flowfield is sampled at four times during the simulations. Samples are taken at 5 and 10 revolutions to determine the reason for the increase in thrust during that period. Another sample is taken at 50 revolutions to determine why the thrust has decreased in comparison to the solution at 10 revolutions and why the thrust is momentarily constant. Finally, samples are taken after convergence at 100-150 revolutions to determine the reason for the second drop in thrust and the increased unsteadiness. At each sampling time the vorticity, Mach number, and eddy viscosity contours are examined.

The tip vortices and sectional blade loading are first analyzed. The history of normal forces is examined at radial stations from r/R =0.25 to 0.95 at increments of 0.10 (Fig. 69). During the first ten revolutions the influence of the tip vortex increases slightly, increasing the overall thrust. As the downward velocity through the rotor plane increases, the tip vortices are washed downward, and the normal loads diminish near the blade tip (Figs. 70, 71). In all cases the influence of the tip vortex is completely diminished beyond 100 revolutions due to the high downward convection rate of the tip vortices. In the HRLES-LDKM and vorticity-based Menter SST simulations the tip vortex is dissipated less than in the other cases; however, little influence on blade loading is observed, since the tip vortex is far from the rotor.

The downward convection of tip vortices observed in the computational simulations was not observed in the experiment of van der Wall and Richard [120]. The location of tip vortices is compared at a vortex age of 5° (Table 12). In the experiment the tip vortex travels upward and toward the root before being washed down through the rotor disk. In the converged solutions of the simulations the tip vortices travel immediately downward.

The Mach number is next evaluated to determine the reason for the variation in tip vortex location (Fig. 72, 73). Between 20 and 50 revolutions the wake moves up along the wall, and begins to induce a larger inflow through the rotor plane. At approximately 50 revolutions the wake has reach the ceiling, and after 60 revolutions the wake begins

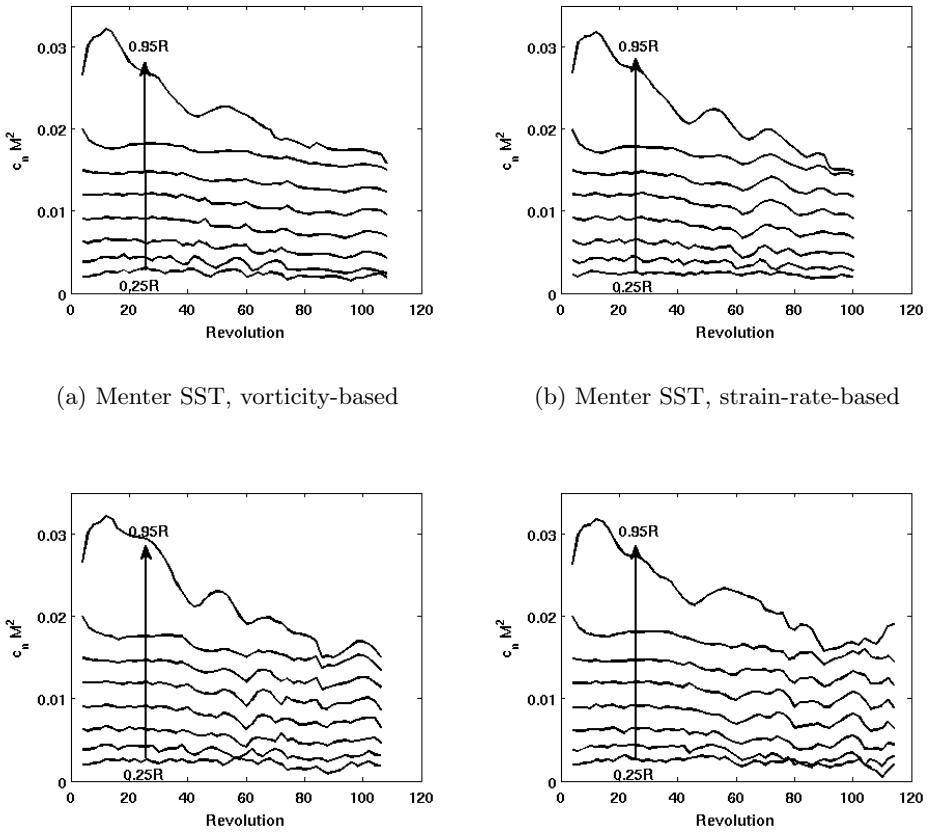

(a) Menter SST, vorticity-based

(b) Menter SST, strain-rate-based

(c) Baseline HRLES

(d) HRLES with LDKM

Figure 69: Normal force on blade sections from r/R =0.25 to 0.95, increments of $0.10R$ for rotor in facility.

Table 12: Tip vortex locations at wake age of 5°.

	$\Delta z/R$	r/R
Experiment [120]	5.03e-3	0.9922
Menter SST, vorticity-based	-3.95e-3	0.9951
Menter SST, strain-rate-based	-4.89e-3	0.9953
Baseline HRLES	-5.95e-3	0.9965
HRLES with LDKM	-3.32e-3	0.9956

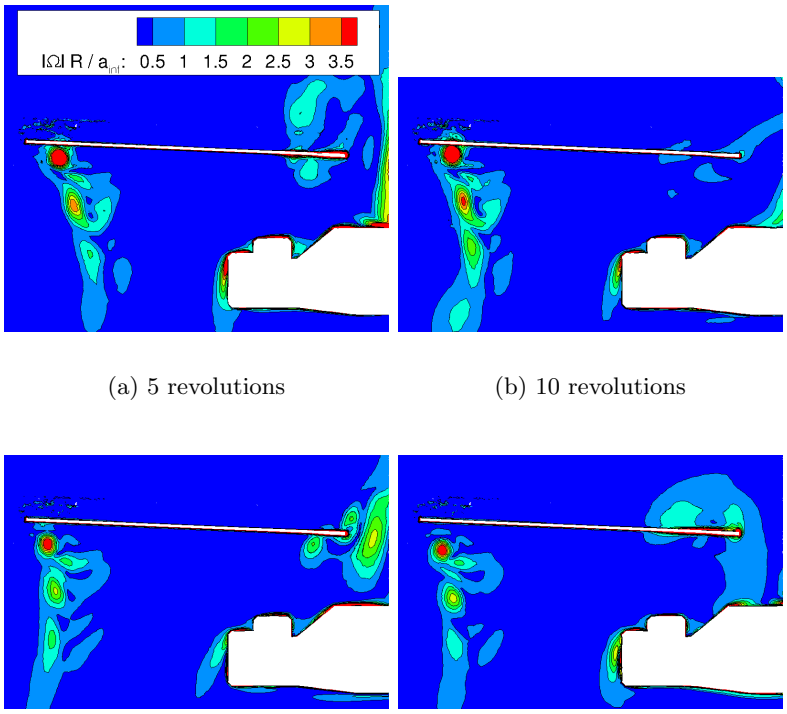

(a) 5 revolutions

(b) 10 revolutions

(c) 50 revolutions

(d) 106 revolutions

Figure 70: Vorticity contours for rotor in facility, viscous walls, HRLES model with LDKM.

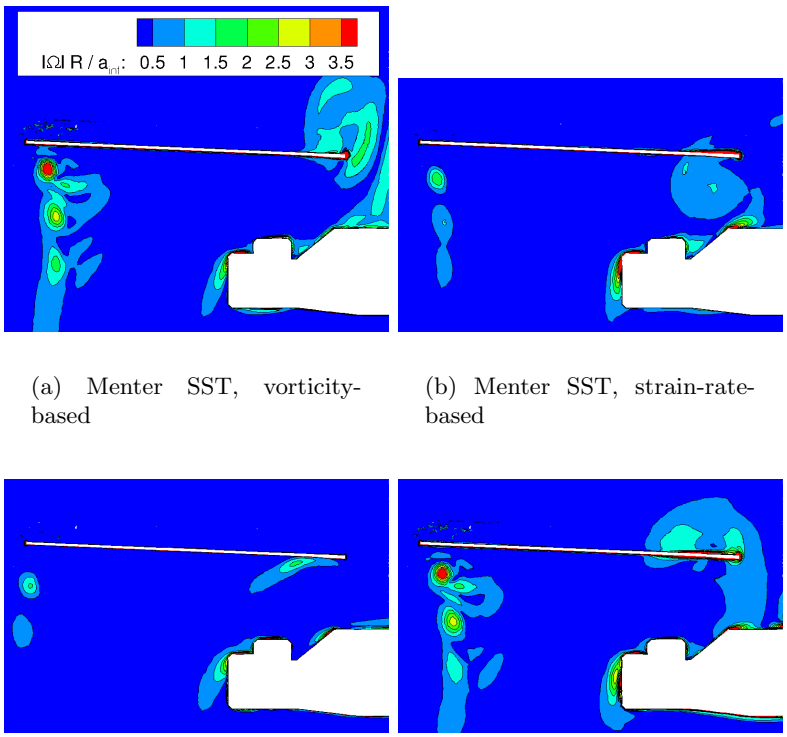

(a) Menter SST, vorticity-based

(b) Menter SST, strain-rate-based

(c) Baseline HRLES

(d) HRLES with LDKM

Figure 71: Final vorticity contours for rotor in facility with viscous walls, after convergence.

to approach the rotor. The high-momentum fluid in the wake begins to wash the tip vortices downward as it recirculates through the rotor disk. In addition, fluctuations in wake properties alter the inflow through the rotor plane, causing variations in thrust.

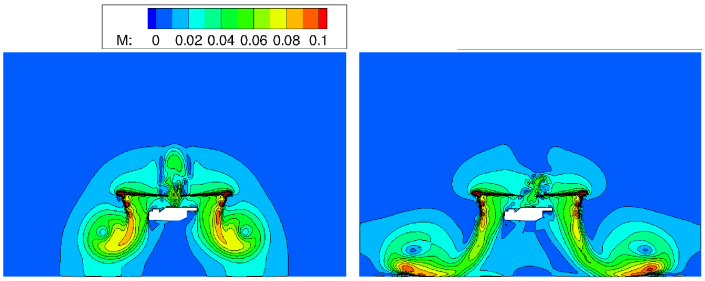

(a) 5 revolutions (b) 10 revolutions

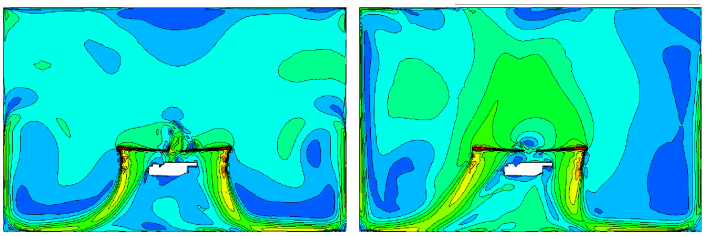

(c) 50 revolutions (d) 100 revolutions

Figure 72: Mach number contours for rotor in facility, viscous walls, HRLES model with LDKM.

In comparison to the inviscid-wall case, there is much more fluctuation in thrust coefficient for the viscous-wall cases. This is a result of velocity fluctuations in the wake which were smoothed by the large eddy viscosity in the inviscid wall case.

Eddy viscosity is next examined in the cases with viscous walls to determine the influence of turbulence model and the boundary condition of test facility walls on the solution (Figs. 74–77). In both URANS cases the maximum eddy viscosity is reduced by an order of magnitude in comparison to the inviscid-wall case. However, even after very long time periods eddy viscosity continues to increase throughout the chamber (Figs. 74–75). In the HRLES cases maximum eddy viscosity is much smaller than in the URANS cases, with maximum values near μ_t/μ =1000. The maximum eddy viscosity changes little throughout the simulation. The baseline HRLES case models a more continuous eddy viscosity, while

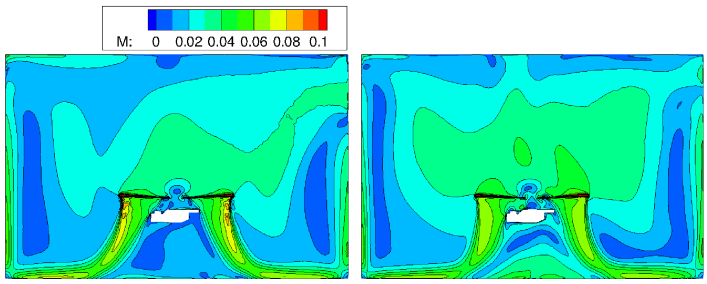

(a) Menter SST, vorticity-based, 100 revolutions

(b) Menter SST, strain-rate-based, 100 revolutions

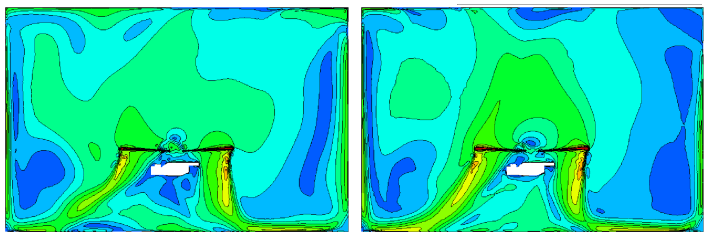

(c) Baseline HRLES, 100 revolutions

(d) HRLES with LDKM, 100 revolutions

Figure 73: Mach number contours for rotor in facility with viscous walls.

values are localized to flow features in the HRLES-LDKM case.

In URANS models it is assumed that all turbulence length scales are modeled, and that the influence of turbulence can be approximated with time-averaged flow properties. In URANS simulations the buildup of eddy viscosity is due to dependence of the turbulence model on a characteristic length based on the distance of each grid node from the nearest viscous wall. The formulation is based on flow physics of the boundary layer, and does not have physical relevance outside the boundary layer, where turbulence is dependent on wake features rather than distances from the nearest viscous surface. In the HRLES simulations eddy viscosity is based on grid resolution, and in LES regions only the subgrid-scale turbulence is modeled. The characteristic length is therefore based on the volume of a cell rather than its distance from a viscous wall. This provides a more physically accurate prediction of turbulence properties outside of boundary layers, and reduces eddy viscosity by an order of magnitude compared to URANS simulations.

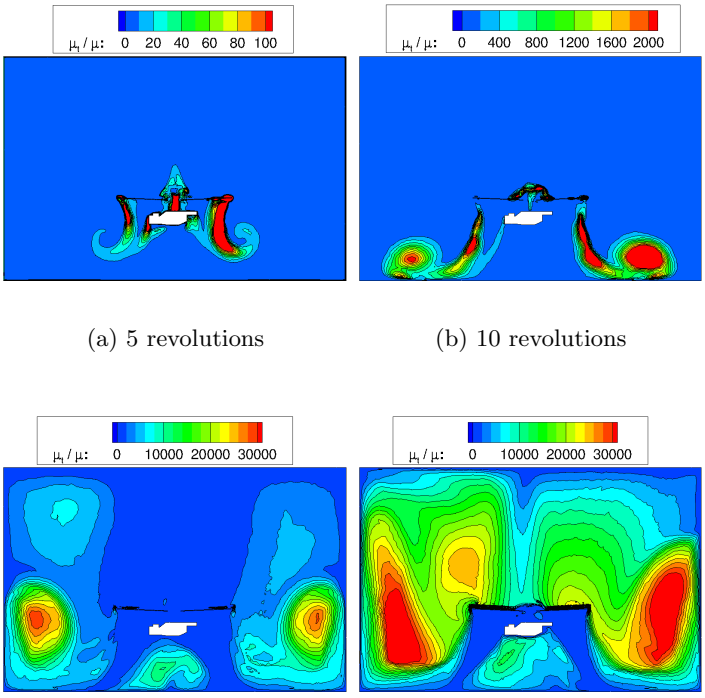

(a) 5 revolutions (b) 10 revolutions

(c) 50 revolutions (d) 100 revolutions

Figure 74: Eddy viscosity contours for rotor in facility, viscous walls, Menter SST vorticity-based model. Scale varies to show levels at different times.

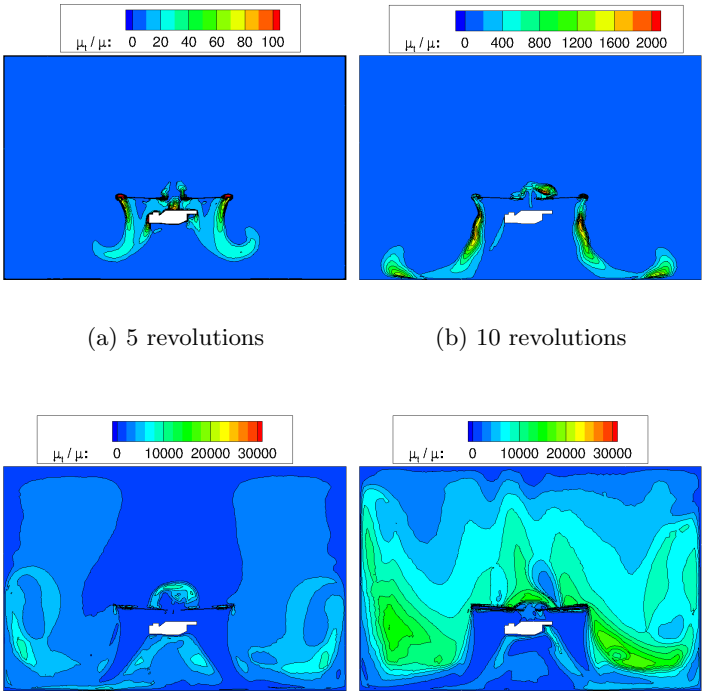

(a) 5 revolutions (b) 10 revolutions

(c) 50 revolutions (d) 100 revolutions

Figure 75: Eddy viscosity contours for rotor in facility, viscous walls, Menter SST strain-rate-based model. Scale varies to show levels at different times.

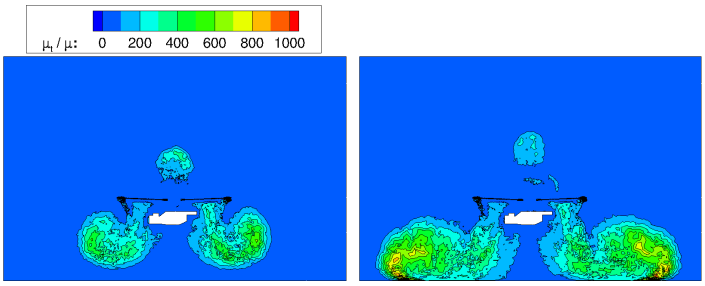

(a) 5 revolutions (b) 10 revolutions

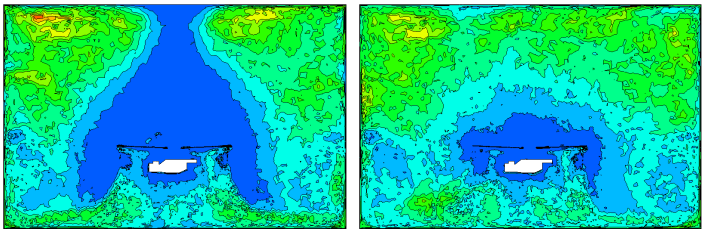

(c) 50 revolutions (d) 100 revolutions

Figure 76: Eddy viscosity contours for rotor in facility with viscous walls and standard HRLES turbulence model.

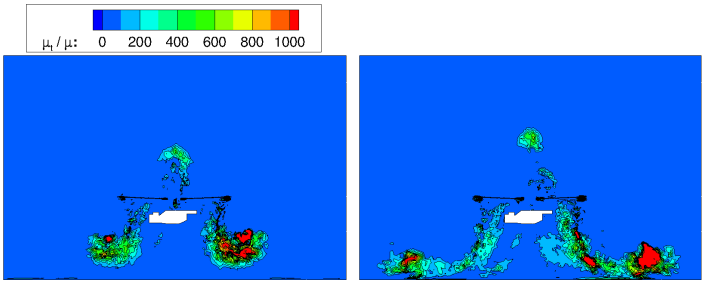

(a) 5 revolutions (b) 10 revolutions

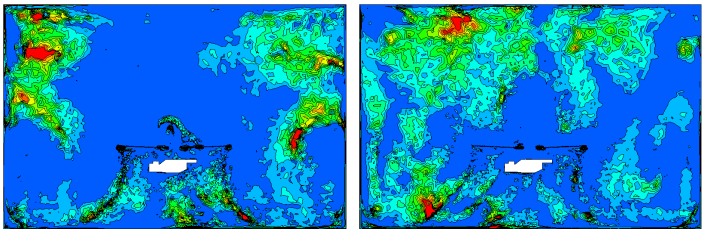

(c) 50 revolutions (d) 100 revolutions

Figure 77: Eddy viscosity contours for rotor in facility with viscous walls and HRLES-LDKM turbulence model.

7.2.2 Influence of Facility Components

In the HOTIS test facility [120] (Fig. 78) several protrusions and cavities along the floor, walls, and ceiling were present during the hover test. While the exact measurements of these components were not available, the dimensions of several components such as the sting, machinery, cabinets, and window cavities were approximated based on digitized data extracted from photographs of the facility. These components were modeled in the background grid as simple prisms and cylinders with viscous surfaces, and the HRLES turbulence model with constant coefficients was applied. Grid spacing was again $0.121c$ near the rotor, and the composite grid consisted of the new background grid with the cavities and protrusions added and the previously-used "medium" blade grid.

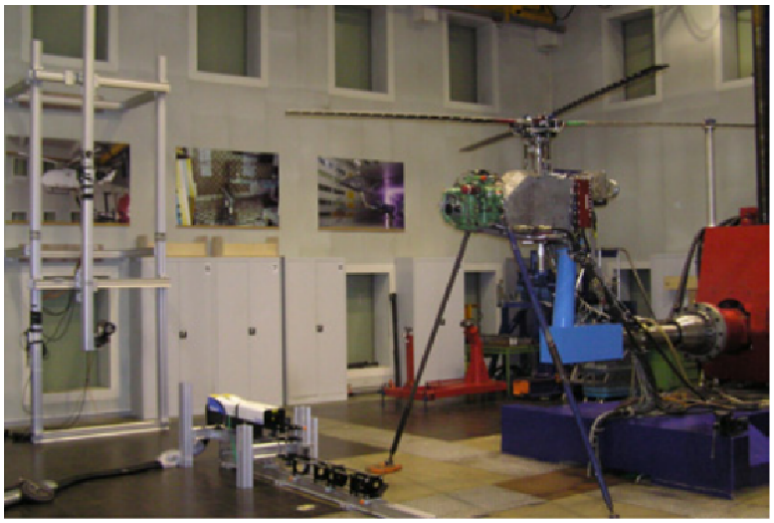

Figure 78: HOTIS test room [120].

With the geometric protrusions modeled in the test facility the figure of merit prediction improved greatly, diminishing the error with respect to experimental measurements, which ranged from -28 to -41% in cases without protrusions, to -12% error. In cases where the protrusions were not modeled the wake initially had little influence on the rotor. After 20 revolutions the thrust began to drop as large recirculation patterns began to form inside the test facility, and the mean thrust continued to decrease until reaching 100 revolutions, where the mean figure of merit was 0.36 to 0.44. When the protrusions were modeled the figure of merit was initially lower, due to recirculation patterns forming more quickly and nearer

to the rotor. However, perturbations in the flow disrupted the larger vortex structures, and over time the effects of recirculation were smaller with protrusions included, as exhibited in the thrust and figure of merit predictions (Fig. 61, 66).

The location of the recirculation vortices influence the direction and magnitude of the tip vortices. In cases without protrusions the inflow velocity is greater, and almost directly downward. When protrusions are modeled the inflow velocity is lower, and as a result the tip vortices remain nearer the rotor (Fig. 79). In all cases except the case with protrusions the influence of the tip vortex is completely diminished beyond 100 revolutions (Fig. 80) due to the dissipation and downwash of the tip vortices, and at 95%R the normal force drops by an average of 26% from 50 to 100 revolutions. In the HRLES-LDKM and vorticity-based Menter SST simulations the tip vortex is dissipated less than in the other cases; however, little influence on blade loading is observed compared to the other cases, since the tip vortex is far from the rotor. In the HRLES case with protrusions the normal force at 95%R is diminished by only 4% during the same time period.

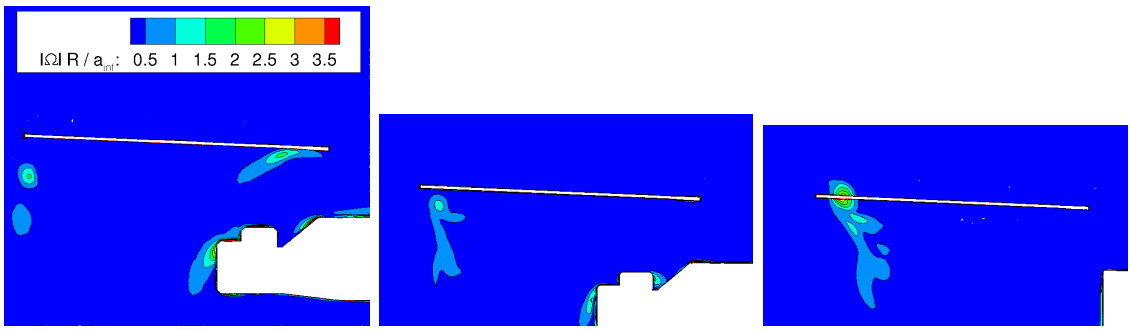

(a) Without protrusions, y-plane (b) With protrusions, y-plane (c) With protrusions, x-plane

Figure 79: Vorticity contours near blade tip at ψ=180° in HOTIS facility with and without protrusions modeled, after convergence.

The figure of merit prediction is also improved compared to cases without the protrusions. The inflow velocity and eddy viscosity, which are influential in figure of merit predictions, are examined. When protrusions are present the inflow velocity is greatly reduced (Fig. 81) due to the size and location of wake vortices. On average, the downward velocity 1R above the rotor disk is 65% greater when the protrusions are not included. The

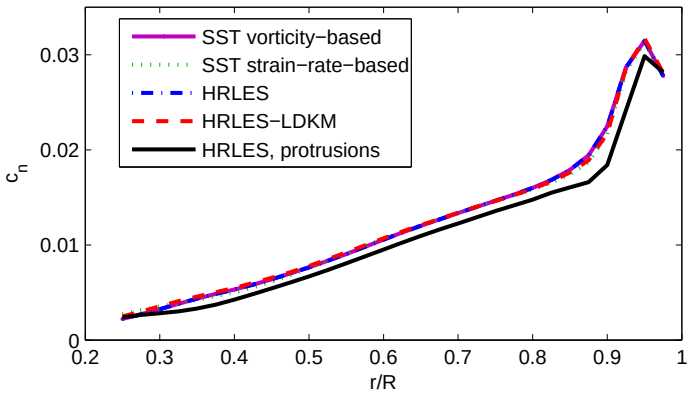

(a) 10 revolutions

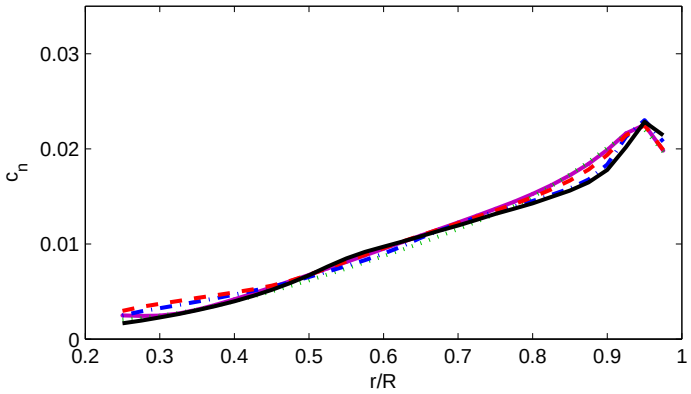

(b) 50 revolutions

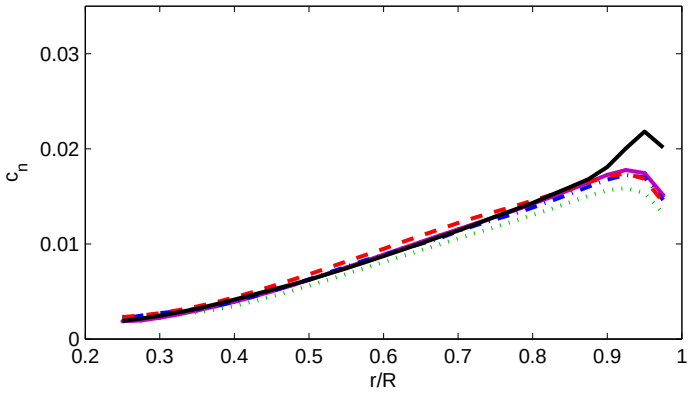

(c) 100 revolutions

Figure 80: Radial normal force distribution (averaged over one revolution) of HOTIS rotor with rigid blades, modeled with and without facility protrusions and cavities.

inflow velocity not only decreases the effective angle of attack, but also has a large influence on movement of the tip vortex, which greatly alters blade loading near the tip.

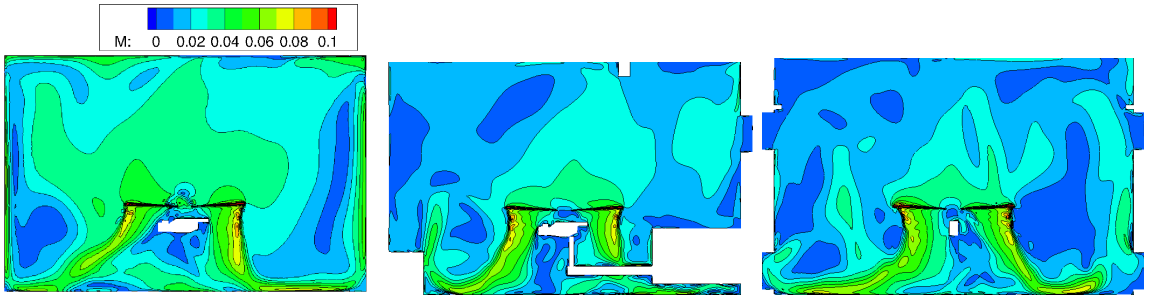

(a) Without protrusions, y-plane (b) With protrusions, y-plane (c) With protrusions, x-plane

Figure 81: Mach number contours in HOTIS facility with and without protrusions, after convergence.

In the case with protrusions, the eddy viscosity reaches 400–500 in isolated regions; however, throughout the facility eddy viscosity is typically 100–300, compared to values of 300–800 more typical of the HRLES case without protrusions. It is observed that in the regions near and below the rotor the eddy viscosity is lower than in the surrounding regions. This can be attributed to the inverse dependency on $V_{cell}^{1/3}$ (Eq. 6), as the grid spacing near and below the rotor is approximately $0.10c$, while it is as high as $0.75c$ away from the rotor. In all HRLES cases the nondimensional eddy viscosity is lower than the "threshold value" of 5.6E3 determined by Réthoré ([98]), indicating that it should not have a severe influence on performance predictions, while in all RANS cases the eddy viscosity exceeds the threshold value. These results are in agreement with his conclusion that RANS turbulence modeling is not suitable for cases in which both small and large scale turbulence is being modeled.

7.3 Summary of Test Facility Analyses

The influence of four turbulence models on rotor performance and flowfield characteristics has been examined. In the two URANS cases, eddy viscosity became very large due to the presence of vortical wake structures away from viscous walls. Figure of merit was significantly under predicted in both cases. Although eddy viscosity predictions were greatly

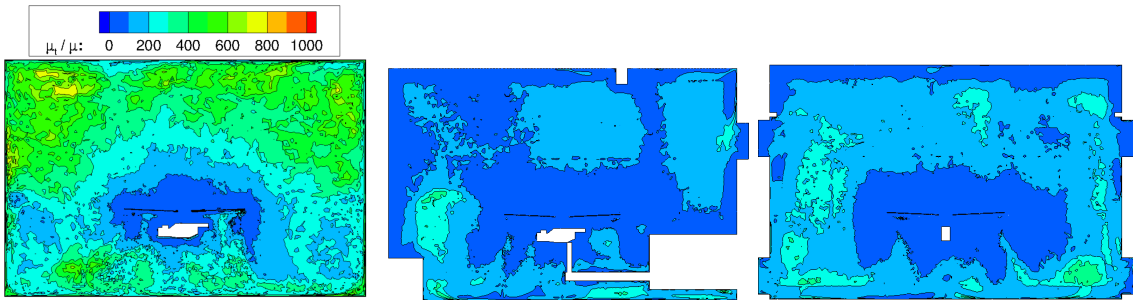

(a) Without protrusions, y-plane

(b) With protrusions, y-plane

(c) With protrusions, x-plane

Figure 82: Eddy viscosity contours in HOTIS facility with HRLES model, after convergence.

reduced when HRLES turbulence models were applied, the figure of merit predictions improved only slightly (Table 11, Fig. 66). No significant improvements in figure of merit resulted from implementation of LDKM in the HRLES turbulence model. While the converged figure of merit predictions of the inviscid wall case are comparable to predictions of the HRLES cases, very large eddy viscosities were generated throughout the simulation, which resulted in a large drop in figure of merit between 35 and 70 revolutions in comparison to all other cases. Inclusion of the cavities and protrusions that were present along the floor, ceiling, and walls of the test facility had a significant influence on wake recirculation characteristics, and the resulting figure of merit predictions were greatly improved (Table 11, Fig. 66). These results indicate that even facility components that are far from the rotor are important in the computational model because of their influence on the wake structure. The thrust (Table 11, Fig. 61) is over predicted when the components are included; however, free air analyses of the HOTIS rotor with rigid and elastic blades indicate that the over-predicted thrust is caused by the rigid blade modeling. When the rotor is modeled with elastic blades, torsion of the blades decreases the average pitch angle and reduces thrust. Thus, for computational modeling of a rotor inside an enclosed chamber it is recommended that an HRLES turbulence model be applied, and that all components in the facility be modeled.

CHAPTER VIII

CONCLUSIONS

A tight CFD/CSD coupling methodology for aeroelastic analysis of rotor with morphing airfoils has been developed. The method has been validated by comparing computational predictions for rotor performance with experimental data. Unsteady camber behavior has been verified through simulation of flexible wing sections performed with the F-S/NLABS and FUN3D/NLABS codes and comparison of flutter speeds with analytical solutions. A stability analysis was also demonstrated for flexible airfoils in compressible flow. Finally, the methodology was demonstrated for three-dimensional rotor cases in forward flight with camber actuation. The influence of test facility components and turbulence modeling were also evaluated. The results obtained from this research yields the following conclusions:

- A methodology for coupling CFD and CSD codes with the capability of modeling radial and chordwise pressure distributions, as well as three-dimensional structural deflections, has been developed and demonstrated.

- In airfoil and rotor analyses it was demonstrated that, although the CFD/CSD interface does not strictly enforce conservation of work, the error in work was small and bounded over time.

- Application of the CFD/CSD methodology to a rotor in hover improved free-air thrust predictions and figure of merit prediction to within 5% of the HART II and HOTIS data. Significant changes in thrust with respect to the rigid case were observed due to the torsional deflection of the rotor blades.

- F-S/NLABS analysis predicted pitch/plunge flutter speeds within 3% of the solutions presented by Zeiler, and parabolic camber flutter within 1% of the approximate solution presented by Murua. The close agreements is expected, since the analyses all applied Peters finite-state aerodynamics.

- FUN3D/NLABS and F-S/NLABS predicted flutter speeds within 5% of each other at low $\omega_\zeta/\omega_\alpha$, while deviating at higher values of $\omega_\zeta/\omega_\alpha$ as the pitch mode began to dominate the instability. This change was traced to a small offset in location of the aerodynamic center from the quarter-chord in CFD results, while in Peters' finite-state aerodynamics, in which inviscid flow and a linear wake are assumed, the aerodynamic center is predicted to be at the quarter-chord.

- The FUN3D/NLABS and F-S/NLABS predictions for parabolic camber flutter speed were 1% at large inverse mass ratios, though differences as large as 25% were observed at small inverse mass ratios. At all inverse mass ratios there is a 2.5% to 4.9% phase difference in the aerodynamic loads. At low inverse mass ratios the flutter speed is more sensitive to phase offsets of the aerodynamic loads, which may be caused by the fidelity of inflow modeling.

- Two-dimensional analyses at compressible speeds indicated that for a NACA 23012 blade section, with pitch and plunge frequencies based on those of the HART II rotor with a rotational speed of 109 rad/s, pitch deflections of the FUN3D/NLABS and F-S/NLABS analyses were within 10-12% of one another in the linear regime, while large differences in behavior were observed once transonic flow became significant. In the F-S/NLABS simulations static divergence was encountered before flutter. In the FUN3D/NLABS simulations limit cycle oscillations were observed once deflections became large, due to the unsteady nonlinear aerodynamics. An analysis of the flowfield and pressure distributions indicated that the motion of the airfoil in FUN3D/NLABS simulation was caused by shed vortices which were produced by shocks and large airfoil deflections.

- In simulations of a NACA 23012 airfoil in compressible flow stiffness requirements for stability were determined. Despite the differences in aeroelastic behavior near the minimum stable camber stiffness, both FUN3D/NLABS and F-S/NLABS predicted similar stiffness requirements for stability.

- A FUN3D/NLABS analysis was performed for the HART II rotor in hover and forward

flight and compared to experimental data. Normal forces were under predicted in dynamic stall and transonic flow regions, but errors were comparable to those of similar CFD/CSD and comprehensive CSD analyses. Peak-to-peak vertical tip deflections were in phase with experimental data, but the magnitude was under predicted. Similar CFD/CSD analyses under predict tip deflections of the HART II rotor by a similar margin.

- In forward flight FUN3D predicts a larger nose-down pitching moment than F-S aerodynamics. This affected the blade torsion, and resulted in a collective trim setting 0.3° larger when CFD loads were applied than when F-S aerodynamics was applied. In addition.

- The influence of wake induced inflow on sectional normal forces was observed in the FUN3D and F-S aerodynamic results. However, while the influence of the tip vortices on pitching moment was observed in FUN3D results, F-S aerodynamics failed to model these influences. These results are consistent with previous analyses in which aerodynamic methods based on lifting-line models fail to predict the influence of tip vortices.

- An analysis of the rotor inflow finite-state modes was performed, and it was determined that it was necessary to include at least 16 modes in order to sufficiently resolve the influence of the wake and reduce deltas with respect to CFD loads.

- Prescribed harmonic camber motion was applied at various phases and magnitudes. FUN3D/NLABS and F-S/NLABS predicted a similar phase response to camber actuation in all cases. In most cases FUN3D/NLABS analyses predicted a larger magnitude response, indicating that the NLABS results provide a more conservative solution for the required camber deflections.

- FUN3D/NLABS and F-S/NLABS solutions indicated that the response to 0.25%c camber actuation is sufficient to minimize individuals hub loads and moments if the actuation phase and magnitude are optimized.

- In complete test facility simulations it was observed that the URANS turbulence model yielded very high eddy viscosity which significantly altered the flowfield and resulted in poor predictions of rotor performance. The HRLES model yielded better results due to improved modeling in eddy viscosity.

- In enclosed facility simulations, inclusion of actual protrusions and cavities along the walls, ceiling, and floor of the facility are important in evaluation of the rotor. Although the components were far from the rotor they altered recirculatory flow structures, which have a significant influence on rotor performance.

- If the effects of elasticity are not included the thrust predictions for the HART II rotor are over predicted. For cases inside a test facility the computational cost for a converged CFD/CSD simulation is estimated to be on the order of 1×10^6 CPU hours, which was not feasible in the current effort. Little influence of aeroelasticity was observed on figure of merit predictions.

8.1 Recommendations for Future Work

The following recommendations are made for future work:

- Simulations performed in this research have been performed for compliant airfoils without actuation and for prescribed airfoil motion in which the stiffness prevented deflections from aerodynamic loads. Stability analyses for a full rotor configuration with and without active camber should be performed to evaluate the interaction between active camber deflections and aerodynamic deflections and to determine the stability limits.

- There is a large difference in the very small time scales required for capturing the near-blade physics and the large time scales required for convergence of the wake solution throughout the test chamber. Due to the number of revolutions required, achieving converged solutions inside an enclosed facility is very computationally expensive. Possible alternatives include hybrid CFD/vortex transport simulations and hybrid CFD/free wake simulations. These methods may have the capability to resolve

wake features more efficiently for long enough durations of time to better evaluate recirculatory effects.

- To reduce unsteady loads in experiments, some researchers have added honeycomb structures and screens to dissipate recirculating wake vortices and reduce large return velocities. Others have placed a duct below the rotor to prevent fountain flow. Employing one of these techniques would allow vibratory loading to be examined without interference from wake vorticity. A methodology for performing computational simulations of this type of configuration should be designed and analyzed.

- Camber actuation was not optimized for vibratory load reduction in the present work. It is not feasible to perform the large sampling of FUN3D/NLABS analyses required by many optimization methods. It may be possible, however, to use F-S/NLABS simulations in performing a search for optimal solutions, and then to use the solution as a beginning point in a gradient-based approach for optimization in a FUN3D/NLABS analysis.

REFERENCES

[1] Ormiston, Robert A., "Applications of the Induced Power Model and Performance of Conventional and Advanced Rotorcraft," in *American Helicopter Society Specialists' Conference on Aeromechanics* , (San Francisco, CA), pp. 588–615, January 20-22, 2010.

[2] Bousman,W. G., "A Qualitative Examination of Dynamic Stall from Flight Test Data," *Journal of the American Helicopter Society*, vol. 43, no. 4, pp. 279–295, 1998.

[3] Datta, Anubhav and Chopra, Inderjit, "Validation of Structural and Aerodynamic Modeling Using UH-60A Airloads Program Data," *Journal of the American Helicopter Society*, vol. 51, no. 1, pp. 43–58, 2006.

[4] Loewy, R., "Helicopter Vibrations: A Technical Perspective," *Journal of the American Helicopter Society*, vol. 29, no. 4, pp. 4–30, 1984.

[5] Friedmann, P. P. and Millott, T. A., "Vibration Reduction in Rotorcraft Using Active Control: A Comparison of Various Approaches," *Journal of Guidance, Control, and Dynamics*, vol. 18, no. 4, pp. 664–673, 1995.

[6] Quinn, Jr., J.H., "Drag Tests of NACA 65(215)-114, a=1.0 Practical Construction Airfoil Section Equipped With 0.295-Airfoil Chord Slotted Flap," Tech. Rep. TN-1236, NACA.

[7] Jose, A. I., Mishra, A., and Baeder, J. D., "An Investigation Into the Aerodynamics of Trailing Edge Flaps With Overhang and Gap," in *American Helicopter Society Specialists' Conference on Aeromechanics*, (San Francisco, CA), January 23-25, 2008.

[8] Chandrasekhara, M. S., Wilder, M. C., and Carr, L. W., "Compressible Dynamic Stall Control: Comparison of Two Approaches," *Journal of Aircraft*, vol. 38, no. 3, pp. 448–453, 2001.

[9] Szodruch, J., "The Influence of Camber Variation on the Aerodynamics of Civil Transport Aircraft," in *American Institute of Aeronautics and Astronautics, Aerospace Sciences Meeting*, (Reno, NV), January 14-17, 1985.

[10] Kerho, M., "Adaptive Airfoil Dynamic Stall Control," *Journal of Aircraft*, vol. 44, no. 4, pp. 1350–1360, July 2007.

[11] Yeo, H., "Assessment of Active Controls for Rotor Performance Enhancement," *Journal of the American Helicopter Society*, vol. 53, no. 2, pp. 152–163, 2008.

[12] Bilgen, O., De Marqui Jr., C., Kochersberger, K. B., and Inman, D. J., "Piezoceramic Composite Actuators for Flow Control in Low Reynolds Number Airflow," *Journal of Intelligent Material Systems and Structures*, vol. 21, no. 12, pp. 1201–1212, 2010.

[13] Palacios, R. and Cesnik, C. E. S., "Geometrically Nonlinear Theory of Composite Beams with Deformable Cross Sections," *AIAA Journal*, vol. 46, no. 2, pp. 439–450, 2008.

[14] Jain, R., Yeo, H., and Chopra, I., "An Examination of Rotor Loads due to On-Blade Active Controls for Performance Enhancement using CFD/CSD Analysis," in *American Helicopter Society Specialists' Conference on Aeromechanics*, (San Francisco, CA), January 20-22, 2010.

[15] Glukhikh, S., Barkanov, E., Kovalev, A., Masarati, P., Morandini, M., Riemenschneider, J., and Wierach, P., "Design of Helicopter Rotor Blades with Actuators Made of a Piezomacrofiber Composite," *Mechanics of Composite Materials*, vol. 44, no. 1, pp. 57–64, 2008.

[16] Shivananda, T. P., *Pressure Measurements Near the Tip of a Hovering Model Rotor Blade and a Preliminary Investigation of the Flow in the Rotor Wake*. PhD thesis, Georgia Institute of Technology, 1977.

[17] Piziali, R. A. and Felker, F. F., "Reduction of Unsteady Recirculation in Hovering Model Helicopter Rotor Testing," *Journal of the American Helicopter Society*, vol. 32, no. 1, pp. 54–59, 1987.

[18] Jackson, C., Wagner, H., and Wasilewski, R., "55-Nitinol - The Alloy with A Memory: Its Physical Metallurgy, Properties, and Applications," Tech. Rep. NASA-SP 5110, National Aeronautics and Space Administration, 1972.

[19] Roglin, R. and Hanagud, S., "Helicopter with Adaptive Rotor Blades for Collective Control," *Smart Materials and Structures*, vol. 5, no. 1, pp. 76–88, 1996.

[20] Tong, D. and Williams II, R. L., "Optimal Shape Control of Composite Thin Plates with Piezoelectric Actuators," *Journal of Intelligent Material Systems and Structures*, vol. 9, no. 6, pp. 458–467, 1998.

[21] Lee, T. and Chopra, I., "Design Issues of a High-Stroke, On-Blade Piezostack Actuator for a Helicopter Rotor with Trailing-Edge Flaps," *Journal of Intelligent Material Systems and Structures*, vol. 11, no. 5, pp. 328–342, 2000.

[22] Chattopadhyay, A., Seeley, C., and Mitchell, L., "Design of a Smart Flap Using Polymeric C-Block Actuators and a Hybrid Optimization Technique," *Smart Materials and Structures*, vol. 6, no. 2, pp. 134 –144, 1997.

[23] Hall, S. and Tzianetopoulou, T., "Design and Testing of a Double X-Frame Piezoelectric Actuator," in *Proceedings of the International Society for Optical Engineering*, (Newport Beach, CA), March 3-6, 2000.

[24] Fulton, M. and Ormiston, R. A., "Hover Testing of a Small-Scale Rotor with On-Blade Elevons," *Journal of the American Helicopter Society*, vol. 46, no. 2, pp. 96–106, 2001.

[25] Boyd, J. A., "Trailing Edge Device for an Airfoil," in *U.S. Patent 4542868*, 1985.

[26] Maughmer, M. D. and Bramesfeld, G., "Experimental Investigation of Gurney Flaps," *Journal of Aircraft*, vol. 45, no. 6, pp. 2062–2067, 2008.

[27] Lee, J. and Shin, S., "Structural Integrity Design for an Active Helicopter Rotor Blade with Piezoelectric Flap Actuators," in *Proceedings of SPIE - The International Society for Optical Engineering*, (San Diego, CA), March 7-10, 2011.

[28] Straub, F. K., Kennedy, D. K., Domzalski, D. B., Hassan, A. A., Ngo, H., Anand, V., and Birchette, T., "Smart Material-Actuated Rotor Technolnnogy - SMART," *Journal of Intelligent Material Systems and Structures*, vol. 15, no. 4, pp. 249–260, 2004.

[29] Straub, F. K., Anand, V. R., Birchette, T. S., and Lau, B. H., "Smart Rotor Development and Wind Tunnel Test," in *Proceedings of the 35th European Rotorcraft Forum*, (Hamburg, Germany), September 22-25, 2009.

[30] Kim, J., Smith, E. C., and Wang, K. W., "Helicopter Blade Loads Control via Multiple Trailing-Edge Flaps," in *Proceedings of the American Helicoper Society 62nd Annual Forum*, (Phoenix, AZ), May 9-11, 2006.

[31] Shin, S. J. and Cesnik, C. E. S., "Forward Flight Response of the Active Twist Rotor for Helicopter Vibration Reduction," in *Proceedings of the 42nd AIAA/ASME/ASCE/AHS/ASC Structures, Structural Dynamics and Materials Conference*, (Seattle, WA), April 16-19, 2001.

[32] Shin, S., Cesnik, C. E. S., and Hall, S. R., "Closed-Loop Control Test of the NASA/Army/MIT Active Twist Rotor for Vibration Reduction," *Journal of the American Helicopter Society*, vol. 50, no. 2, pp. 178–194, 2005.

[33] Bernhard, A. P. F. and Wong, J., "Wind-Tunnel Evaluation of a Sikorsky Active Rotor Conroller Implemented on the NASA/ARMY/MIT Active Twist Rotor," *Journal of the American Helicopter Society*, vol. 50, no. 1, pp. 65–81, 2005.

[34] Haynes, R. A., *Hygrothermally Stable Laminated Composites*. PhD thesis, Georgia Institute of Technology, 2010.

[35] Bilgen, O., De Marqui Jr., C., Kochersberger, K. B., and Inman, D. J., "Macro-Fiber Composite Actuators for Flow Control of a Variable Camber Airfoil," *Journal of Intelligent Material Systems and Structures*, vol. 22, no. 1, pp. 81–91, 2011.

[36] Gandhi, F., Frecker, M., and Nissly, A., "Design Optimization of a Controllable Camber Rotor Airfoil," *AIAA Journal*, vol. 46, no. 1, pp. 142–153, 2008.

[37] Grohmann, B. A., Müller, F., Ahci, E., Pfaller, R., Bauer, M., Maucher, C., Dieterich, O., Storm, S., and Jänker, P., "Design, Evaluation and Test of Active Trailing Edge," in *Proceedings of the 67th Annual Forum of the American Helicopter Society*, (Virginia Beach, VA), May 3-5, 2011.

[38] Young, A. D., "The Aerodynamic Characteristics of Flaps," Tech. Rep. R M 2662, Aeronautical Research Council, 1947.

[39] Stability and Control Group, "Approximate Relationships for Determining Airplane Maximum Lift Coefficients," Tech. Rep. SM-13874, Douglas Aircraft Company, Inc., 1950.

[40] Semezis, Y. and Gombert, J., "The High-Lift Wing, Remarks on the Prediction of Characteristics," Tech. Rep. TT-F-14073, NASA, December 1971.

[41] Smith, A., "High-Lift Aerodynamics," *Journal of Aircraft*, vol. 12, no. 6, pp. 501–530, 1975.

[42] Brune, G. W. and McMasters, J. H., *Computational Aerodynamics Applied to High-Lift Systems*, vol. 125. New York: AIAA, 1989.

[43] Newman, J., Barnwell, R. W., and Taylor, A. C., "Aerodynamic Shape Sensitivity Analysis and Design Optimization of Complex Configurations Using Unstructured Grids," in *Applied Aerodynamics Conference*, (Atlanta, GA), AIAA 1997-2275, June 23-25, 1997.

[44] Guruswamy, G. P., "Unsteady Aerodynamic and Aeroelastic Calculations for Wings Using Euler Equations," *AIAA Journal*, vol. 28, no. 3, pp. 461–469, 1990.

[45] Bauchau, O. A. and Ahmad, J. U., "Advanced CFD and CSD Methods for Multidisciplinary Applications in Rotorcraft Problems," in *AIAA, NASA, and ISSMO, Symposium on Multidisciplinary Analysis and Optimization*, (Bellevue, WA), AIAA 1996-4151, September 4-6, 1996.

[46] Potsdam, M., Yeo, H., and Johnson, W., "Rotor Airloads Prediction Using Loose Aerodynamic/Structural Coupling," *Journal of Aircraft*, vol. 43, no. 3, pp. 732–742, 2006.

[47] Datta, A. and Chopra, I., "Prediction of the UH-60A Main Rotor Structural Loads Using Computational Fluid Dynamics/Comprehensive Analysis Coupling," *Journal of the American Helicopter Society*, vol. 53, no. 4, pp. 351–365, 2008.

[48] Biedron, R. and Lee-Rausch, E., "Rotor Airloads Prediction Using Unstructured Meshes and Loose CFD/CSD Coupling," in *26th AIAA Applied Aerodynamics Conference, AIAA Paper 2008-7341*, (Honolulu, HI), AIAA 2008-7341, August 18-21, 2008.

[49] Abras, J. N. and Smith, M. J., "Rotorcraft Methodology for Unstructured CFD-CSD Coupling," in *American Helicopter Society Specialists' Conference on Aerodynamics*, (San Francisco, CA), January 23-25, 2008.

[50] Farhat, C., Lesoinne, M., Stern, P., and Lantèri, S., "High Performance Solution of Three-Dimensional Nonlinear Aeroelastic Problems via Parallel Partitioned Algorithms: Methodology and Preliminary Results," *Advances in Engineering Software*, vol. 28, no. 1, pp. 43–61, 1997.

[51] Pawar, P. M., Jung, S. N., and Yu, Y. H., "Helicopter Vibration Reduction Using Active Twist Control of Composite Rotor Blades," in *Proceedings of the 64th Annual Forum of the American Helicopter Society*, (Montreal, Canada), April 29-May 1, 2008.

[52] Bagai, A. and Leishman, J. G., "Rotor Free-Wake Modeling using a Pseudo-Implicit Technique Including Comparisons with Experiment," *Journal of the American Helicopter Society*, vol. 40, no. 3, pp. 29–41, 1995.

[53] Tung, C., Cardonna, F. X., and Johnson, W. R., "The Prediction of Transonic Flows on an Advancing Rotor," *Journal of the American Helicopter Society*, vol. 31, no. 3, pp. 4–9, 1986.

[54] Nygaard, T. A., Saberi, H. A., Ormiston, R. A., Strawn, R. C., and Potsdam, M., "CFD and CSD Coupling Algorithms and Fluid Structure Interface for Rotorcraft Aeromechanics in Steady and Transient Flight Conditions," in *Proceedings of the 62nd Annual Forum of the American Helicopter Society*, (Phoenix, AZ), May 9-11, 2006.

[55] Padthe, A. K., Liu, L., and Friedmann, P. P., "A Comprehensive Study of Active Microflaps for Vibration Reduction in Rotorcraft," in *Proceedings of the 66th Annual Forum of the American Helicopter Society*, (Phoenix, AZ), May 11-13, 2010.

[56] Ravichandran, K., Chopra, I., Wake, B. E., and Hein, B., "Active Flaps and Slats for Rotor Performance Enhancement," in *Proceedings of the 67th Annual Forum of the American Helicopter Society*, (Virginia Beach, VA), May 3-5, 2011.

[57] Datta, A. and Johnson, W., "A Multibody Formulation for Three Dimensional Brick Finite Element Based Parallel and Scalable Rotor Dynamic Analysis," in *Proceedings of the 66th Annual Forum of the American Helicopter Society*, (Phoenix, AZ), May 11-13, 2010.

[58] Han, T. and Li, R., "Transonic Aeroelastic Software and its Engineering Application," in *Proceedings of the 2nd WRI World Congress on Software Engineering*, (Wuhan, Hubei, China), December 19-20, 2010.

[59] Chen, G., Li, Y., and Yan, G., "Active Control Law Design for Flutter/LCO Suppression Based on Reduced Order Model Method," *Chinese Journal of Aeronautics*, vol. 23, no. 6, pp. 639–646, 2010.

[60] Taylor, N. V., Allen, C. B., Jones, D. P., Gaitonde, A., and Hill, G. F. J., "Investigation of Structural Modelling Methods for Aeroelastic Calculations," in *Proceedings of the 22nd AIAA Applied Aerodynamics Conference*, (Providence, RI), AIAA 2004-5370, August 16-19, 2004.

[61] Palacios, R. and Cesnik, C. E. S., "Low-Speed Aeroelastic Modeling of Very Flexible Slender Wings With Deformable Airfoils," in *Proceedings of the 49th AIAA/ASME/ASCE/AHS/ASC Structures, Structural Dynamics and Materials Conference*, (Schaumburg, IL), AIAA 2008-1995, 2008.

[62] Kumar, D. and Cesnik, C. E. S., "Performance Enhancement and Vibration Reduction in Dynamic Stall Condition Using Active Camber Deformation," in *Proceedings of the 69th Annual Forum*, (Phoenix, AZ), May 21-23 2013.

[63] Murua, J., Palacios, R., and Peiró, J., "Camber Effects in the Dynamic Aeroelasticity of Compliant Airfoils," *Journal of Fluids and Structures*, vol. 26, no. 4, pp. 527–543, 2010.

[64] Peters, D. A., Hsieh, M.-C. A., and Torrero, A., "A State-Space Airloads Theory for Flexible Airfoils," *Journal of the American Helicopter Society*, vol. 52, no. 4, pp. 329–342, 2007.

[65] Dunn, P. and Dugundji, J., "Nonlinear Stall Flutter and Divergence Analysis of Cantilivered Graphite/Epoxy Wings," *AIAA Journal*, vol. 30, no. 1, pp. 153–162, 1992.

[66] Kim, A. and Dugundji, J., "Nonlinear Large Amplitude Vibration of Composite Helicopter Blade at Large Static Deflection," *AIAA Journal*, vol. 31, no. 5, pp. 938–946, 1993.

[67] Caradonna, F. X. and Tung, C., "Experimental and Analytical Studies of a Model Helicopter Rotor in Hover," Tech. Rep. TM-81232, NASA, September 1981.

[68] Devenport, W., Rife, M., Liapis, S., and Follin, G., "The Structure and Development of a Wing-tip Vortex," *Journal of Fluid Mechanics*, vol. 312, pp. 67–106, April 1996.

[69] Chow, J. S., Zilliac, G. G., and Bradshaw, P., "Mean and Turbulence Measurements in the Near Field of a Wingtip Vortex," *AIAA Journal*, vol. 35, no. 10, pp. 1561–1567, 1997.

[70] Ramasamy, M., Johnson, B., and Leishman, J. G., "Turbulent Tip Vortex Measurements Using Dual-Plane Stereoscopic Particle Image Velocimetry," *AIAA Journal*, vol. 47, no. 8, pp. 1826–1840, 2009.

[71] Felker, F. F. and Light, J. S., "Aerodynamic Interactions Between a Rotor and Wing in Hover," *Journal of the American Helicopter Society*, vol. 33, no. 2, pp. 53–61, 1988.

[72] Polak, D. R., Rehm, W., and George, A. R., "Effects of an Image Plane on the Tiltrotor Fountain Flow," *Journal of the American Helicopter Society*, vol. 45, no. 2, pp. 90–96, 2000.

[73] Potsdam, M. A. and Strawn, R. C., "CFD Simulations of Tiltrotor Configurations in Hover," *Journal of the American Helicopter Society*, vol. 50, no. 1, pp. 82–94, 2005.

[74] Ganesh, B. and Komerath, N., "Study of Ground Vortex Structure of Rotorcraft in Ground Effect at Low Advance Ratios," in *Proceedings of the 24th AIAA Applied Aerodynamics Conference*, (San Francisco, CA), AIAA 2006-3475, June 5-8, 2006.

[75] Ganesh, B., *Unsteady Aerodynamics of Rotorcraft at Low Advance Ratios in Ground Effect*. PhD thesis, Georgia Institute of Technology, 2010.

[76] Timm, G. K., "Obstacle-Induced Flow Recirculation," *Journal of Sound and Vibration*, vol. 4, no. 3, pp. 490–506, November 1966.

[77] Kini, S. and Conlisk, A. T., "Nature of Locally Steady Rotor Wakes," *Journal of Aircraft*, vol. 39, no. 5, pp. 750–758, September-October 2002.

[78] Singh, R. and Brown, R., "CFD Modeling and Simulation for Ducted Rotor Test Stand Design," in *Proceedings of the 67th Annual Forum of the American Helicopter Society*, (Virginia Beach, VA), May 3-5, 2011.

[79] Romander, E., Norman, T. R., and Chang, I., "Correlating CFD Simulation With Wind Tunnel Test for the Full-Scale UH-60A Airloads Rotor," in *Proceedings of the 67th Annual Forum of the American Helicopter Society*, (Virginia Beach, VA), May 3-5, 2011.

[80] Spalart, P. R., "Strategies for Turbulence Modelling and Simulations," *International Journal of Heat and Fluid Flow*, vol. 21, no. 3, pp. 252–263, 2000.

[81] Duraisamy, K. and Baeder, J. K., "High Resolution Wake Capturing Methodology for Hovering Rotors," *Journal of the American Helicopter Society*, vol. 52, no. 2, pp. 110–122, 2007.

[82] Bhagwat, M. and Leishman, J. G., "Correlation of Helicopter Rotor Tip Vortex Measurements," *AIAA Journal*, vol. 38, no. 2, pp. 301–308, February 2000.

[83] K., M. and Heineck, J., "Measurements of the Early Development of Trailing Vorticity from a Rotor," no. NASA/TP-2002-211848, AFDD/TR-02-A001, May.

[84] Holst, T. L. and Pulliam, T. H., "Overset Solution Adaptive Grid Approach Applied to Hovering Rotorcraft Flows," in *Proceedings of the 27th AIAA Applied Aerodynamics Conference*, (San Antonio, TX), AIAA 2009-3519, June 22-25, 2009.

[85] Benek, J., Buning, P., and Steger, J., "A 3-D CHIMERA Grid Embedding Technique," in *Proceedings of the 7th Computational Physics Conference*, (Cincinnati, OH), AIAA 1985-1523, July 15-17, 1985.

[86] Buning, P., Chiu, I., Obayashi, S., Rizk, Y., and Steger, J., "Numerical Simulation of the Integrated Space Shuttle Vehicle in Ascent," in *Proceedings of the 15th Atmospheric Flight Mechanics Conference*, (Minneapolis, MN), AIAA 1988-4359, August 15-17, 1988.

[87] Nichols, R., Tramel, R., and Buning, P., "Solver and Turbulence model Upgrades to OVERFLOW2 for Unsteady and High-Speed Applications," in *Proceedings of the 24th Applied Aerodynamics Conference*, (San Francisco, CA), AIAA 2006-2824, June 5-8, 2006.

[88] Post, D. E., "A New DoD Initiative: The Computational Research and Engineering Acquisition Tools and Environments, (CREATE) Program," *Journal of Physics: Conference Series*, vol. 125, no. 1, 2008.

[89] Sankaran, V., Sitaraman, J., Wissink, A., Datta, A., Jayaraman, B., Potsdam, M., Mavriplis, D., Yang, Z., O'Brien, D., Saberi, H., Cheng, R., Hariharan, N., and Strawn, R., "Application of the Helios Computational Platform to Rotorcraft Flowfields," in *48th AIAA Aerospace Sciences Meeting Including the New Horizons Forum and Aerospace Exposition*, (Orlando, FL), AIAA 2010-1230, January 4-7 2010.

[90] Mavriplis, D. J. and Venkatakrishnan, V., "A Unified Multigrid Solver for the Navier-Stokes Equations on Mixed Element Meshes," *International Journal of Computational Fluid Dynamics*, vol. 8, no. 4, pp. 247–263, 1997.

[91] Mavriplis, D. J., "Viscous Flow Analysis Using a Parallel Unstructured Multigrid Solver," *AIAA Journal*, vol. 38, no. 11, pp. 2067–2076, November 2000.

[92] Wissink, A. M., Hornung, R. D., Kohn, S., Smith, S., and Elliott, N., "Large-Scale Parallel Structured AMR Calculations Using the SAMRAI Framework," in *Proceedings of Supercomputing 2001 (SC01)*, (Denver CO), November 2001.

[93] Hornung, R. D., Wissink, A. M., and Kohn, S. R., "Managing Complex Data and Geometry in Parallel Structured AMR Applications," *Engineering with Computers*, vol. 22, no. 3-4, pp. 181–195, December 2006.

[94] Pulliam, T. H., "Euler and Thin-Layer Navier-Stokes Codes: ARC2D, and ARC3D," in *Computational Fluid Dynamics Users Workshop*, (Tullahoma, TN), March 12-16, 1984.

[95] Saberi, H., Khoshlahjeh, M., and Ormiston, R. andRutkowski, M. J., "Overview of RCAS and Application to Advanced Rotorcraft Problems," in *American Helicopter Society Specialists' Conference on Aeromechanics*, (San Francisco, CA), January 21-23, 2004.

[96] Kamkar, S. J. and Wissink, A. M., "An Automated Adaptive Mesh Refinement Scheme for Unsteady Aerodynamic Wakes," in *50th AIAA Aerospace Sciences Meeting Including the New Horizons Forum and Aerospace Exposition*, (Nashville, TN), AIAA 2012-0160, January 9-12, 2012.

[97] Wissink, A., Jayaraman, B., Datta, A., Sitaraman, J., Potsdam, M., Kamkar, S., Mavriplis, D., Yang, Z., Jain, R., Lim, J., and Strawn, R., "Capability Enhancments in Version 3 of the Helios High-Fidelity Rotorcraft Simulation Code," in *50th AIAA Aerospace Sciences Meeting Including the New Horizons Forum and Aerospace Exposition*, (Nashville, TN), AIAA 2012-0713, January 9-12, 2012.

[98] Réthoré, P. E., *Wind Turbine Wake in Atmospheric Turbulence*. PhD thesis, Aalborg University, 2009.

[99] Gundling, C., Roget, B., Sitaraman, J., and Rai, R., "Comparison of Wind Turbine Wakes in Steady and Turbulent Inflow," in *50th AIAA Aerospace Sciences Meeting Including the New Horizons Forum and Aerospace Exposition*, (Nashville, TN), AIAA 2012-0899, January 9-12, 2012.

[100] Wilcox, D. C., *Turbulence Modeling for CFD*. DCW Industries, 2nd ed., 1998.

[101] Menter, F. R., "Two-Equation Eddy-Viscosity Turbulence Models for Engineering Applications," *AIAA Journal*, vol. 32, no. 8, pp. 1598–1605, 1994.

[102] Menter, F. R., "Review of the Shear-Stress Transport Turbulence Model Experience from an Industrial Perspective," *International Journal of Computational Fluid Dynamics*, vol. 23, no. 4, pp. 305–316, April-May 2009.

[103] Moore, J. G. and Moore, J., "Realizability in Two-Equation Turbulence Models," in *Proceedings of the 30th AIAA Fluid Dynamics Conference*, (Norfolk, VA), AIAA 1999-3779, June 28-July 1, 1999.

[104] Smirnov, P. E. and Menter, F. R., "Sensitization of the SST Turbulence Model to Rotation and Curvature by Applying the Spalart-Shur Correction Term," *Journal of Turbomachinery*, vol. 131, no. 4, pp. 1–8, 2009.

[105] Dacles-Mariani, J., Zilliac, G. G., Chow, J. S., and Bradshaw, P., "Numerical/Experimental Study of a Wingtip Vortex in the Near Field," *AIAA Journal*, vol. 33, no. 9, pp. 1561–1568, 1995.

[106] Dacles-Mariani, J. and Kwak, D. and Zilliac, G., "On Numerical Error and Turbulence Modeling in Tip Vortex Flow Prediction," *International Journal for Numerical Methods in Fluids*, vol. 30, no. 1, pp. 65–82, 1999.

[107] Smagorinsky, J., "General Circulation Experiments with the Primitive Equations," *Monthly Weather Review*, vol. 91, no. 3, pp. 99–164, 1963.

[108] Travin, A., Shur, M., Strelets, M., and Spalart, P., "Detached-Eddy Simulations Past a Circular Cylinder," *Flow, Turbulence and Combustion*, vol. 63, no. 1, pp. 293–313, 2000.

[109] Lynch, C. E. and Smith, M. J., "Extension and Exploration of a Hybrid Turbulence Model on Unstructured Grids," vol. 49, pp. 2585–2590, November 2011.

[110] Shelton, A. B., Braman, K., Smith, M. J., and Menon, S., "Improved Hybrid RANS-LES Turbulence Modeling for Rotorcraft," in *Proceedings of the 62nd Annual Forum of the American Helicopter Society*, (Phoenix, AZ), May 9-11, 2006.

[111] Kim, W. and Menon, S., "An Unsteady Incompressible Navier-Stokes Solver for Large Eddy Simulation of Turbulent Flows," *International Journal for Numerical Methods in Fluids*, vol. 31, no. 6, pp. 983–1017, November 1999.

[112] Menon, S. and Patel, N., "Subgrid Modeling for Simlation of Spray Combustion in Large-Scale Combustors," *AIAA Journal*, vol. 44, no. 4, pp. 709–723, April 2006.

[113] Lilly, D. K., "A Proposed Modification of the Germano Subgrid-Scale Closure Method," *Physics of Fluids*, vol. 4, no. 3, pp. 633–635, 1992.

[114] Sánchez-Rocha, M., *Wall-Models for Large Eddy Simulation Based on a Generic Additive-Filter Formulation.* PhD thesis, Georgia Institute of Technology, 2009.

[115] Kawai, S. and Fujii, K., "Analysis and Prediction of Thin-Airfoil Stall Phenomena with Hybrid Turbulence Methodology," *AIAA Journal*, vol. 43, no. 5, pp. 953–961, May 2005.

[116] Lynch, C. E., *Advanced CFD Methods for Wind Turbine Analysis.* PhD thesis, Georgia Institute of Technology, 2011.

[117] Vreman, B., Geurts, B., and Kuerten, H., "Realizability Conditions for the Turbulent Stress Tensor in Large-Eddy Simulation," *Journal of Fluid Mechanics*, vol. 278, pp. 351–362, 1994.

[118] Fang, Y. and Menon, S., "Kinetic-Eddy Simulation of Static and Dynamic Stall," in *Proceedings of the 24th Applied Aerodynamics Conference*, (San Francisco, CA), AIAA 2006-3847, June 5-8, 2006.

[119] van der Wall, B. G., "2nd HHC Aeroacoustic Rotor Test (HART II)– Part I: Test Documentation," Tech. Rep. IB 111-2003/31, German Aerospace Center (DLR), Braunschweig, Germany, November 2003.

[120] van der Wall, B. G. and Richard, H., "Hover Tip Vortex Structure Test (HOTIS) - Test Documentation and Representative Results," Tech. Rep. IB 111-2008/16, German Aerospace Center (DLR), Braunschweig, Germany, May 2008.

[121] Cesnik, C. E. and Hodges, D. H., "VABS: A New Concept for Composite Rotor Blade Cross-Sectional Modeling," *Journal of the American Helicopter Society*, vol. 42, no. 1, pp. 27–38, 1997.

[122] Palacios, R. and Cesnik, C. E. S., "Cross-Sectional Analysis of Nonhomogeneous Anisotropic Active Slender Structures," *AIAA Journal*, vol. 43, no. 12, pp. 2624–2638, 2005.

[123] Thepvongs, S., Cesnik, C. E. S., Cook, J. R., and Smith, M. J., "Computational Aeroelasticity of Rotating Wings with Deformable Airfoils," in *Proceedings of the 65th Annual Forum of the American Helicopter Society*, (Grapevine, TX), April 29-May 1, 2009.

[124] Peters, D. A., Boyd, D. D., and He, C. J., "Finite-State Induced-Flow Model for Rotors in Hover and Forward Flight," *Journal of the American Helicopter Society*, vol. 34, no. 4, pp. 5–17, October 1989.

[125] Petot, D., "Differential Equation Modelling of Dynamic Stall," *La Recherche Aerospatiale*, no. 5, pp. 59–72, 1989.

[126] Stumpf, W. and Peters, D. A., "An Integrated Finite-State Model for Rotor Deformation, Non-linear Airloads, Inflow and Trim," *Mathematical Computer Modeling*, vol. 18, no. 3, pp. 115–129, 1993.

[127] Thepvongs, S., Cesnik, C. E. S., Palacios, R., and Peters, D. A., "Finite-state Aeroelastic Modeling of Rotating Wings with Deformable Airfoils," in *Proceedings of the 64th Annual Forum*, (Montreal, Canada), April 29-May 1, 2008.

[128] Drela, M. and Giles, M. B., "Viscous-Inviscid Analysis of Transonic and Low Reynolds Number Airfoils," *AIAA Journal*, vol. 25, no. 10, pp. 1347–1355, 1987.

[129] Peters, D. A., Bayly, P., and Li, S., "A Hybrid Periodic-Shooting, Auto-Pilot Method for Rotorcraft Trim Analysis," in *Proceedings of the 52nd Annual Forum of the American Helicopter Society*, (Washington, D.C.), June 4-6, 1996.

[130] Anderson, W., Rausch, R., and Bonhaus, D., "Implicit/Multigrid Algorithms for Incompressible Turbulent Flows on Unstructured Grids," *Journal of Computational Physics*, vol. 128, no. 2, pp. 391–408, 1996.

[131] Bonhaus, D., "An Upwind Multigrid Method For Solving Viscous Flows On Unstructured Triangular Meshes," Master's thesis, George Washington University, 1993.

[132] O'Brien, D., *Analysis of Computational Modeling Techniques for Complete Rotorcraft Configurations*. PhD thesis, Georgia Institute of Technology, 2006.

[133] Renaud, T., OBrien, D., Smith, M., and Potsdam, M., "Evaluation of Isolated Fuselage and Rotor-Fuselage Interaction Using Computational Fluid Dynamics," *Journal of the American Helicopter Society*, vol. 53, no. 1, pp. 3–17, January 2008.

[134] Abras, J. A., *Enhancement of Aeroelastic Rotor Airload Prediction Methods*. PhD thesis, Georgia Institute of Technology, 2009.

[135] Noack, R., "DiRTlib: A Library to Add an Overset Capability to Your Flow Solver," in *Proceedings of the 17th AIAA Computational Fluid Dynamics Conference*, (Toronto, Ontario), AIAA 2005-5116, June 6-9, 2005.

[136] Noack, R., "SUGGAR: A General Capability for Moving Body Overset Grid Assembly," in *Proceedings of the 17th AIAA Computational Fluid Dynamics Conference*, (Toronto, Ontario), AIAA 2005-5117, June 6-9, 2005.

[137] Biedron, R. and Lee-Rausch, E., "Computation of UH-60A Airloads Using CFD/CSD Coupling on Unstructured Meshes," in *Proceedings of the 67th Annual Forum of the American Helicopter Society*, (Virginia Beach, VA), May 3-5, 2011.

[138] Biedron, R. and Lee-Rausch, E., "An Examination of Unsteady Airloads on a UH-60A Rotor: Computation Versus Measurement," in *Proceedings of the 68th Annual Forum of the American Helicopter Society*, (Fort Worth, TX), May 1-3, 2012.

[139] Pidaparti, R. M. V., "Structural and Aerodynamic Data Transformation Using Inverse Isoparametric Mapping," *AIAA Journal of Aircraft*, vol. 29, no. 3, pp. 507–509, 1992.

[140] Lee, P. K., "CFD/CSD Grid Interfacing of Three-Dimensional Surfaces by Inverse Isoparametric Mapping," Master's thesis, Massachusetts Institute of Technology, 2001.

[141] Smith, M. J., Cesnik, C. E. S., and Hodges, D. H., "An Evaluation of Computational Algorithms Suitable for Fluid-Structure Interactions," *AIAA Journal of Aircraft*, vol. 37, no. 2, pp. 282–294, 2000.

[142] Smith, M. J., "Conservation Issues for Reynold-Averaged Navier-Stokes-Based Rotor Aeroelastic Simulations," *Journal of Aerospace Engineering*, vol. 25, no. 2, pp. 217–227, April 2012.

[143] Richard, H. and van der Wall, B., "Detailed Investigation of Rotor Tip Vortex in Hover Condition," in *Proceedings of the 32nd European Rotorcraft Forum*, (Maastricht, The Netherlands), September 12-14, 2006.

[144] van der Wall, B. G. and Burley, C. L., "2nd HHC Aeroacoustic Rotor Test (HART II)– Part II: Test Documentation," Tech. Rep. IB 111-2005/03, German Aerospace Center (DLR), Braunschweig, Germany, November 2005.

[145] Jacobs, E. N. and Clay, W. C., "Characteristics of the NACA 23012 Airfoil from Tests in the Full-Scale and Variable-Density Tunnels," Tech. Rep. 530, NACA, 1936.

[146] van der Wall, B. G., Lim, J. W., Smith, M. J., Jung, S. N., Bailly, J., Baeder, J. D., and Boyd, D. D., "The HART II International Workshop: An Assessment of the State-of-the-Art in Comprehensive Code Prediction," *CEAS Aeronautical Journal*, vol. 4, no. 3, pp. 223–252, September 2013.

[147] Smith, M. J., Lim, J. W., Van der Wall, B. G., Baeder, J. D., Biedron, R. T., Boyd, D. D., Jayaraman, B., Jung, S. N., and Min, B. Y., "The HART II International Workshop: An Assessment of the State of the Art in CFD/CSD," *CEAS Aeronautical Journal*, vol. 4, no. 4, pp. 345–372, December 2013.

[148] Theodorsen, T., "General Theory of Aerodynamic Instability and the Mechanism of Flutter," Tech. Rep. 496, NACA, 1935.

[149] Palacios, R. and Cesnik, C. E. S., "Low-Speed Aeroelastic Modeling of Very Flexible Slender Wings with Deformable Airfoils," in *Proceedings of the 49th AIAA/ASME/ASCE/AHS/ASC Structures, Structural Dynamics and Materials Conference*, (Schaumburg, IL), AIAA 2008-1995, April 2008.

[150] Jones, K. D. and Platzer, M. F., "Numerical Computation of Flapping-Wing Propulsion and Power Extraction," in *35th Aerospace Sciences Meeting and Exhibit*, (Reno, NV), AIAA 97-0826, January 6-10, 1997.

[151] Zeiler, T. A., "Results of Theodorsen and Garrick Revisited," *Journal of Aircraft*, vol. 37, no. 5, pp. 918–920, 2000.

[152] Pope, A., *The Forces and Pressures over an NACA 0015 Airfoil through 180 Degrees Angle of Attack*. PhD thesis, Georgia Institute of Technology, 1947.

[153] Critzos, C., Heyson, H., and Boswinkle Jr., R., "Aerodynamic Characersitics of NACA 0012 Airfoil Section at Angles of Attack from 0 to 180," Tech. Rep. TN-3361, NACA, 1955.

[154] Smith, M. J., Koukol, B. C. G., Quackenbush, T., and Wachspress, D., "Reverse- and Cross-Flow Aerodynamics for High-Advance-Ratio Flight," in *Proceedings of the 35th European Rotorcraft Forum*, (Hamburg, Germany), September 22-25, 2009.

[155] Smith, M. J., Liggett, N. D., and Koukol, B. C. G., "Aerodynamics of Airfoils at High and Reverse Angles of Attack," *Journal of Aircraft*, vol. 48, no. 6, pp. 2012–2023, November-December 2011.

[156] Hunt, J. D. R., "Developments in Computational Modelling of Turbulent Flows," in *ERCOFTAC Work*, (Lausanne, Switzerland), Cambridge University Press, March 26-28, 1990.

VITA

James Richard Cook was born in Rockdale, TX in 1980, where he attended high school school and graduated in 1999. He attended Brigham Young University in Provo, UT for one year before leaving to offer voluntary service in Costa Rica for two years. He returned to Brigham Young University to earn a Bachelor of Science degree in Mechanical Engineering in 2006. During his undergraduate studies he took interest in fluid dynamics and aerodynamics, and he decided to pursue a higher education in the field of aerospace engineering at the Georgia Institute of Technology with a focus in aeroelasticity. He began working as a graduate research assistant in the Computational Aeroelasticity Laboratory in 2007 where he began his research in CFD methodology. During his first year at Georgia Tech he met his wife Lisa Kunkel, whom he married July 18, 2009. He graduated with his master's degree December 2009 and went on to finish his Doctorate of Philosophy in Aerospace Engineering while working as an aerospace/software engineer for CymSTAR LLC to develop software upgrades for flight simulators.